

# Offline Parameter Estimation of a 18.5 kW Doubly fed induction generator

by  
Seyed Hamed Eghbali Dogaheh



*Thesis presented in partial fulfilment of the requirements for the degree  
Master of Science in Engineering  
at Stellenbosch University*

UNIVERSITEIT  
iYUNIVESITHI  
STELLENBOSCH  
UNIVERSITY

100  
1918 · 2018

Supervisor: Dr Nkosinathi Gule  
Co-Supervisor: Prof. H.J. Vermeulen  
Faculty of Engineering  
Department of Electrical and Electronic Engineering

December 2018

## DECLARATION

By submitting this thesis electronically, I declare that the entirety of the work contained therein is my own, original work, that I am the sole author thereof (save to the extent explicitly otherwise stated), that reproduction and publication thereof by Stellenbosch University will not infringe any third party rights and that I have not previously in its entirety or in part submitted it for obtaining any qualification.

Date: December 2018

Copyright © 2018 Stellenbosch University

All rights reserved

## ABSTRACT

In the past years, technology advancements have allowed the wind energy to become one of the most economical forms of power generation in the field of renewable energies. Nowadays, wind turbines that produce electricity make use of the advance and mature technologies and generate sustainable sources of energy. In the areas where the wind is plentiful, it is a major rival to the conventional sources of energy. Many countries worldwide have vast resources of it but still, haven't used its capacity to the fullest. The upsides of wind energy are:

- Omitting the emission of greenhouse gases.
- The energy supplies can be increased and diversified using wind energy.
- In comparison to the other power sources, a shorter time is required for planning, design, and construction.
- The flexibility of such projects so that the current wind farms can host more turbines in case of higher demand for energy.
- Finally, a significant saving in terms of materials, labor and investment.

The extracted energy from the wind, is in the form of kinetic energy and is harnessed by the rotor blades and turned into mechanical energy. Then, this mechanical energy is transformed into the electrical energy by a wind turbine generator. The nominal power extracted from the wind varies based on the size of the rotor and the wind speed, regardless of the losses.

The power ratings for wind generators varies from some hundred watts to multi-megawatt generators depending on the utilization and where they are stationed.

Nowadays, a vast percentage of the larger scale wind generators employ the geared topologies, AC outputs connected to the power grid through power electronic converters, while it seems that the dynamic in the market is gradually changing towards employing the permanent magnet, gearless topologies by using the fully-rated power electronic converters. On the other hand, the small-scale turbines usually employ the direct drive generators with DC outputs and aeroelastic blades. However, the use of wind generators in a direct drive topology accompanied by the aeroelastic blades and DC outputs is rarely used and still under development.

It is impossible to have the exact same power generation from the wind each year due to its variable nature. Furthermore, the wind generators can only be used in areas where a minimum speed of 4.5 m/s or higher is available. The suitable sites are chosen based on the measurements on the site and the data from a wind atlas.

There are several methods for analyzing the dynamic behavior of the wind turbines. Employing the parameters of such systems is a suitable way to analysis the machine dynamic behavior and

reduces complexities regarding the use of higher order models. The problem is that these parameters are subject to change in different operating conditions and need to be estimated accurately by some methods. This study concentrates on estimating the parameters of a doubly fed induction generator by employing the previously proposed Matlab c-code and s-function codes and investigates the practical application of that method on a 18.5 kW doubly fed induction generator.

## OPSOMMING

In die afgelope jaar het tegnologie vooruitgang die windenergie toegelaat om een van die mees ekonomiese vorme van kragopwekking op die gebied van hernubare energie te word. Vandag maak windturbines wat elektrisiteit produseer, gebruik van die voor- en volwasse tegnologie en volhoubare energiebronne. In die gebiede waar die wind oorvloed is, is dit 'n groot mededinger in die konvensionele energiebronne. Baie lande wêreldwyd het groot middele, maar het nog steeds nie sy vermoë tot die uiterste gebruik nie. Die opwaartse windenergie is:

- Om die uitstoot van kweekhuysgasse uit te skakel.
- Die energiebronne kan verhoog en gediversifiseer word met behulp van windenergie.
- In vergelyking met die ander kragbronne word 'n korter tyd benodig vir beplanning, ontwerp en konstruksie.
- Die buigsaamheid van sulke projekte, sodat die huidige windplase meer turbines in die geval van hoër vraag na energie kan gasheer.
- Ten slotte, 'n beduidende besparing in terme van materiale, arbeid en belegging.

Die energie wat uit die wind onttrek word, is in die vorm van kinetiese energie en word deur die rotorblades aangewend en omskep in meganiese energie. Dan word hierdie meganiese energie omgeskakel na die elektriese energie deur 'n windturbine generator. Die nominale krag wat uit die wind onttrek word, hang af van die grootte van die rotor en die windspoed, ongeag die verliese.

Die kraggraderings vir windopwekkers wissel van sowat honderd watt na multi-megawatt kragopwekkers, afhangende van die gebruik en waar hulle gestasioneer is.

Deesdae gebruik 'n groot persentasie van die grootskaalse windopwekkers die toegepaste topologieë, AC-uitsette wat via die elektriese elektroniese omsetters aan die rooster verbind word, terwyl dit blyk dat die dinamiek in die mark geleidelik verander na die gebruik van die permanente magneet, ratlose topologieë deur die volwaardige krag elektroniese omsetters. Aan die ander kant gebruik die kleinschalige turbines gewoonlik die direkte dryfgenerators met gelykstroomuitsette en aeroelastiese lemme. Die gebruik van windgenerators in 'n direkte dryf topologie, vergesel van die aeroelastiese lemme en GS-uitsette word egter selde gebruik en steeds onder ontwikkeling.

Dit is onmoontlik om elke jaar dieselfde kragopwekking uit die wind te kry as gevolg van die veranderlike aard daarvan. Verder kan die windgenerators slegs gebruik word in gebiede waar

'n minimum spoed van 4,5 m / s of hoër beskikbaar is. Die geskikte plekke word gekies op grond van die metings op die terrein en die data van 'n windatlas.

Daar is verskeie metodes om die dinamiese gedrag van die windturbines te ontleed. Die gebruik van die parameters van sulke stelsels is 'n geskikte manier om die masjien dinamiese gedrag te ontleed en kompleksiteit te verminder rakende die gebruik van hoër-orde modelle. Die probleem is dat hierdie parameters onderworpe is aan verandering in verskillende bedryfsomstandighede en deur sommige metodes akkuraat beraam moet word. Hierdie studie fokus op die raming van die parameters van 'n dubbel gevoed induksie generator deur gebruik te maak van die voorheen voorgestelde Matlab c-kode en s-funksie kodes en ondersoek die praktiese toepassing van die metode op 'n 18.5 kW dubbel gevoed induksie generator.

## **ACKNOWLEDGEMENTS**

I would like to thank Dr. Nkosinathi Gule and Professor HJ (Johan) Vermeulen, Department of Electrical and Electronics Engineering, University of Stellenbosch, for their invaluable contributions to this project. I would like to thank my family for their precious support.

## CONTENTS

DECLARATION .....	I
ABSTRACT.....	II
OPSOMMING .....	IV
ACKNOWLEDGEMENTS .....	VI
CONTENTS.....	VII
LIST OF FIGURES .....	XIII
LIST OF TABLES .....	XVII
LIST OF ABBREVIATIONS AND SYMBOLS .....	XX
<b>1 INTRODUCTION .....</b>	<b>1</b>
1.1 Background.....	1
1.2 Review of Related Research.....	3
1.3 Thesis Contributions .....	4
1.4 Thesis structure .....	4
<b>2 LITERATURE REVIEW .....</b>	<b>5</b>
2.1 Introduction.....	5
2.2 Overview of the wind turbine systems topologies .....	5
2.2.1 Introduction.....	5
2.2.2 Fixed speed wind turbine systems .....	5
2.2.3 Two-speed induction generator wind turbine systems .....	6
2.2.4 Variable speed wind turbine systems.....	7
2.2.4.1 Variable rotor resistance generator topology .....	8
2.2.4.2 Generator with fully-rated converter topology .....	9
2.2.4.3 Generator with direct drive and fully-rated converter topology .....	10
2.2.4.4 Direct drive grid-connected slip-synchronous permanent magnet generator topology	11
2.2.4.5 Double-fed induction generator topology .....	12
2.2.4.6 Directly coupled synchronous generator with variable gearbox topology.....	13



2.3 System identification and parameter estimation .....	14
2.3.1 Introduction.....	14
2.3.2 System identification and parameter estimation .....	14
2.3.3 Cost functions .....	17
2.3.4 Optimisation algorithms .....	18
2.3.4.1 Newton method.....	22
2.3.4.2 Gauss-Newton method.....	22
2.3.4.3 Trust-region method.....	23
2.3.4.4 Levenberg-Marquardt method .....	24
2.3.4.5 Conclusion .....	25
2.4 Overview of the parameter identification and estimation methods .....	25
2.4.1 Introduction.....	25
2.4.2 Offline parameter identification techniques .....	26
2.4.3 Online rotor time constant estimation techniques.....	30
2.4.3.1 Spectral analysis techniques.....	30
2.4.3.2 Observer-based techniques .....	31
2.4.3.3 Model reference adaptive system-based techniques .....	33
2.4.3.4 Other methods.....	34
2.4.4 Online estimation of stator resistance.....	34
2.4.5 Online compensation of saturation and iron loss.....	35
3 MODELING AND PARAMETER ESTIMATION METHODOLOGY .....	37
3.1 Introduction.....	37
3.2 Mathematical models.....	37
3.2.1 System overview.....	37
3.2.2 Components Modelling .....	37
3.2.2.1 Aerodynamic block.....	38
3.2.2.2 Mechanical block.....	40

3.2.2.3	Electrical block .....	42
3.2.2.3.1	Introduction .....	42
3.2.2.3.2	Doubly fed induction generator ABC model.....	42
3.2.2.3.3	Doubly fed induction generator Direct–Quadrature (DQ) model.....	45
3.3	Overview of MATLAB C-code and S-functions.....	47
3.4	Parameter Estimation Process.....	48
4	PARAMETER DETERMINATION AND TEST ARRANGEMENT.....	50
4.1	Introduction.....	50
4.2	18.5 kW wounded rotor induction machine.....	51
4.2.1	18.5 kW Induction machine parameter determination.....	52
4.2.1.1	DC tests.....	52
4.2.1.2	No-load test.....	53
4.2.1.3	Blocked rotor test.....	54
4.2.1.4	Parameters calculation .....	55
4.3	22 kW induction machine .....	56
4.4	Powerflex 700 variable frequency AC drive .....	57
4.5	Torque measurement.....	57
4.6	Current measurement .....	58
4.7	Voltage measurement .....	59
4.8	Angular position and angular velocity measurement.....	61
4.9	Data acquisition hardware and software .....	62
4.9.1	Data acquisition hardware .....	62
4.9.1.1	NI CompactDAQ 9178 8-Slot USB Chassis.....	62
4.9.1.2	NI 9215 measurement card .....	63
4.9.1.3	NI 9401 measurement card .....	64
4.9.1.4	NI 9237 measurement card .....	64
4.9.2	Data acquisition software .....	65

4.9.2.1 Voltage and current measurement task .....	66
4.9.2.2 Load cell measurement task .....	66
4.9.2.3 Angular position and angular velocity measurement task .....	67
4.9.2.4 Front panel structure .....	67
4.9.2.5 Task synchronization .....	69
<b>5 PARAMETER ESTIMATION RESULTS.....</b>	<b>71</b>
5.1 Introduction.....	71
5.2 Parameter estimation procedure.....	71
5.3 Estimation results based on simulated signals .....	73
5.3.1 Stator voltage perturbation .....	74
5.3.1.1 ABC model .....	76
5.3.1.2 DQ model.....	77
5.3.2 Angular velocity perturbation.....	77
5.3.2.1 ABC model .....	80
5.3.2.2 DQ model.....	81
5.3.3 Conclusion .....	81
5.4 Estimation results based on measured signals .....	81
5.4.1 Stator voltage perturbation .....	82
5.4.1.1 ABC model .....	85
5.4.1.2 DQ model.....	86
5.4.2 Angular velocity perturbation.....	86
5.4.2.1 ABC model .....	89
5.4.2.2 DQ model.....	90
5.4.3 Conclusion .....	90
5.5 Result improvement for the measurement based estimations.....	90
5.5.1 Introduction.....	90
5.5.2 Considering the initial conditions .....	90

5.5.2.1 Stator voltage perturbation.....	91
5.5.2.1.1 ABC model.....	91
5.5.2.1.2 DQ model.....	91
5.5.2.2 Angular velocity perturbation.....	92
5.5.2.2.1 ABC model.....	92
5.5.2.2.2 DQ model.....	93
5.5.3 Windowing the output signals.....	93
5.5.3.1 Stator voltage perturbation.....	94
5.5.3.1.1 ABC model.....	94
5.5.3.1.2 DQ model.....	94
5.5.3.2 Angular velocity perturbation.....	95
5.5.3.2.1 ABC model.....	95
5.5.3.2.2 DQ model.....	96
5.5.4 Cost function modification.....	96
5.5.4.1 Stator voltage perturbation.....	96
5.5.4.1.1 ABC model.....	96
5.5.4.1.2 DQ model.....	97
5.5.4.2 Angular velocity perturbation.....	98
5.5.4.2.1 ABC model.....	98
5.5.4.2.2 DQ model.....	98
5.5.5 Symmetrical components method.....	99
5.5.5.1 Stator voltage perturbation.....	100
5.5.5.1.1 ABC model.....	100
5.5.5.1.2 DQ model.....	100
5.5.5.2 Angular velocity perturbation.....	101
5.5.5.2.1 ABC model.....	101
5.5.5.2.2 DQ model.....	102

5.5.6 Conclusion .....	102
6 CONCLUSIONS AND RECOMMENDATIONS .....	103
7 REFERENCES .....	107
APPENDIX A : LABVIEW IMPLEMENTATION OF MEASUREMENT SYSTEM.....	113
A.1.1 Introduction.....	113
A.1.2 Current and voltage tasks.....	A-1
A.1.3 Torque reading task .....	A-2
A.1.4 Angular velocity and position measurement task .....	A-3
A.1.5 Measurements synchronization task .....	A-4
A.1.6 Complete System including all tasks .....	A-5
APPENDIX B : DATA SHEETS.....	B-1
B.1.1 Introduction.....	B-1
B.1.2 CCELL PA6110 200 kg load cell datasheet.....	B-1
B.1.3 LEM Hass 50-S current sensor electrical data .....	B-2
B.1.4 LEM LV 25-P voltage transducer technical data .....	B-3
B.1.5 Baumer GI342 incremental encoder technical data .....	B-3
B.1.6 NI CompactDAQ 9178 8-Slot USB Chassis.....	B-4
B.1.7 NI 9215 measurement card .....	B-5
B.1.8 NI 9401 measurement card .....	B-6
B.1.9 NI 9237 measurement card .....	B-7

## LIST OF FIGURES

Figure 2-1: Fixed-speed generator topology.....	5
Figure 2-2: Power versus the angular velocity [rpm] for two-speed induction generator [10].	6
Figure 2-3: Two-speed generator topology.....	7
Figure 2-4: Variable rotor resistance generator topology. ....	9
Figure 2-5: Generator with fully-rated converter topology. ....	9
Figure 2-6: Generator with direct drive and fully-rated topology. ....	10
Figure 2-7: Cross-sectional diagram of the SS-PMG [11].....	11
Figure 2-8: SS-PMG topology [11]. ....	12
Figure 2-9: Double-fed induction generator topology. ....	13
Figure 2-10: Directly coupled synchronous generator with variable gearbox topology. ....	13
Figure 2-11: Block diagram of the system identification process [12], [13].....	15
Figure 2-12: Block diagram of the parameter estimation process [14]. ....	16
Figure 2-13: Optimisation tree diagram [13]. ....	19
Figure 3-1: Wind turbine system functional block diagram .....	37
Figure 3-2: Operating points for a wind turbine with a two-speed induction generator topology [7].....	39
Figure 3-3: Two-mass gearbox model [5]. ....	41
Figure 3-4: Three-phase machine diagram [78].....	42
Figure 3-5: Two-phase machine diagram [80].....	45
Figure 3-6: Flow diagram of the main functional components of C-code S-function [6]. ....	48
Figure 3-7: Parameter estimation process diagram [6].....	49
Figure 4-1: Simplified schematic picture of the test bench. ....	50
Figure 4-2: SPER 200 L4, 18.5 kW wounded rotor induction machine nameplate. ....	52
Figure 4-3: 22 kW induction machine nameplate.....	56
Figure 4-4: Powerflex 700 Variable frequency AC drive.....	57

Figure 4-5: CCELL PA6110 200 kg load cell. ....	58
Figure 4-6: LEM Hass 50-S current sensor. ....	59
Figure 4-7: LEM Hass 50-S current sensor connection circuit and operation diagram.....	59
Figure 4-8: LEM LV 25-P voltage transducer. ....	60
Figure 4-9: LEM LV 25-P voltage transducer connection diagram. ....	60
Figure 4-10: Baumer GI342 incremental encoder. ....	61
Figure 4-11: Baumer GI342 incremental encoder output signals. ....	61
Figure 4-12: Baumer GI342 incremental encoder terminal assignment. ....	62
Figure 4-13: NI CompactDAQ 9178 USB Chassis. ....	62
Figure 4-14: NI 9215 measurement card. ....	63
Figure 4-15: NI 9401 measurement card. ....	64
Figure 4-16: NI 9237 measurement card. ....	65
Figure 4-17: Current and voltage measurement task structured by NI-DAQmx functions. ....	66
Figure 4-18: load cell measurement task structured by NI-DAQmx functions. ....	67
Figure 4-19: Angular position and angular velocity task structured by NI-DAQmx functions. .....	67
Figure 4-20: Front panel of the codes written for the measurements including the settings in Labview.....	68
Figure 4-21: Front panel of the codes written for the measurements including some of the virtual screens. ....	68
Figure 4-22: Generic block diagram of the Align and resample VI for synchronizing different signals. ....	69
Figure 4-23: Complete Labview generic block diagram with all the tasks used in this study.	70
Figure 5-1: Three-phase stator voltages perturbation. ....	74
Figure 5-2: Three-phase stator currents .....	75
Figure 5-3: Three-phase rotor currents. ....	75

Figure 5-4: Mechanical torque.....	76
Figure 5-5: Angular velocity perturbation. ....	78
Figure 5-6: Three-phase stator voltages.....	78
Figure 5-7: Three-phase stator currents. ....	79
Figure 5-8: Three-phase rotor currents. ....	79
Figure 5-9: Mechanical torque.....	80
Figure 5-10: Three-phase stator voltages.....	83
Figure 5-11: Three-phase stator voltages showing the perturbation point. ....	83
Figure 5-12: Three-phase stator currents. ....	84
Figure 5-13: Three-phase rotor currents. ....	84
Figure 5-14: Mechanical torque.....	85
Figure 5-15: Angular velocity perturbation. ....	87
Figure 5-16: Three-phase stator voltage perturbation.....	87
Figure 5-17: Three-phase stator currents. ....	88
Figure 5-18: Three-phase rotor currents. ....	88
Figure 5-19: Mechanical torque.....	89
Figure 7-1 Current and voltage tasks .....	A-1
Figure 7-2 Torque reading task.....	A-2
Figure 7-3 Angular velocity and position measurement task .....	A-3
Figure 7-4 Measurements synchronization task .....	A-4
Figure 7-5 Complete System including all tasks .....	A-5
Figure 7-6 CCELL PA6110 200 kg load cell datasheet.....	B-1
Figure 7-7 LEM Hass 50-S current sensor electrical data .....	B-2
Figure 7-8 LEM LV 25-P voltage transducer technical data .....	B-3
Figure 7-9 Baumer GI342 incremental encoder technical data .....	B-3
Figure 7-10 NI CompactDAQ 9178 8-Slot USB Chassis.....	B-4



Figure 7-11 NI 9215 measurement card .....	B-5
Figure 7-12 NI 9401 measurement card .....	B-6
Figure 7-13 NI 9237 measurement card .....	B-7

## LIST OF TABLES

Table 3-1: Swept area for H-rotor and Darrieus rotor [10].....	40
Table 4-1: SPER 200 L4, 18.5 kW wounded rotor induction machine data provided by VEM. .....	51
Table 4-2: DC tests results of the 18.5 kW induction machine. ....	53
Table 4-3: No load test results of the 18.5 kW induction machine.....	54
Table 4-4: Blocked rotor test results of the 18.5 kW induction machine. ....	54
Table 4-5: Calculated parameters of 18.5 kW induction machine based on the tests data.....	56
Table 5-1: Parameter estimation settings.....	74
Table 5-2: The ABC model Parameter estimation results for the stator voltage perturbation based on the simulated signals.....	76
Table 5-3: The DQ model Parameter estimation results for the stator voltage perturbation based on the simulated signals. ....	77
Table 5-4: The ABC model Parameter estimation results for the angular velocity perturbation based on the simulated signals.....	80
Table 5-5: The DQ model Parameter estimation results for the angular velocity perturbation based on the simulated signals.....	81
Table 5-6: Parameter estimation settings.....	82
Table 5-7: The ABC model Parameter estimation results for the stator voltage perturbation based on the measured signals. ....	85
Table 5-8: The DQ model Parameter estimation results for the stator voltage perturbation based on the measured signals. ....	86
Table 5-9: The ABC model Parameter estimation results for the angular velocity perturbation based on the measured signals. ....	89
Table 5-10: The DQ model Parameter estimation results for the angular velocity perturbation based on the measured signals. ....	90
Table 5-11: The ABC model Parameter estimation results for the stator voltage perturbation based on the measured signals considering the initial conditions.....	91

Table 5-12: The DQ model Parameter estimation results for the stator voltage perturbation based on the measured signals considering the initial conditions.....	92
Table 5-13: The ABC model Parameter estimation results for the angular velocity perturbation based on the measured signals considering the initial conditions.....	92
Table 5-14: The DQ model Parameter estimation results for the angular velocity perturbation based on the measured signals considering the initial conditions.....	93
Table 5-15: The ABC model Parameter estimation results for the stator voltage perturbation based on the measured signals considering the windowed output signals.....	94
Table 5-16: The DQ model Parameter estimation results for the stator voltage perturbation based on the measured signals considering the windowed output signals.....	95
Table 5-17: The ABC model Parameter estimation results for the angular velocity perturbation based on the measured signals considering the windowed output signals.....	95
Table 5-18: The DQ model Parameter estimation results for the angular velocity perturbation based on the measured signals considering the windowed output signals.....	96
Table 5-19: The ABC model Parameter estimation results for the stator voltage perturbation based on the measured signals considering the modified cost function. ....	97
Table 5-20: The DQ model Parameter estimation results for the stator voltage perturbation based on the measured signals considering the modified cost function. ....	97
Table 5-21: The ABC model Parameter estimation results for the angular velocity perturbation based on the measured signals considering the modified cost function. ....	98
Table 5-22: The DQ model Parameter estimation results for the angular velocity perturbation based on the measured signals considering the modified cost function. ....	99
Table 5-23: The ABC model Parameter estimation results for the stator voltage perturbation based on the measured signals considering the symmetrical components. ....	100
Table 5-24: The DQ model Parameter estimation results for the stator voltage perturbation based on the measured signals considering the symmetrical components. ....	101
Table 5-25: The ABC model Parameter estimation results for the angular velocity perturbation based on the measured signals considering the modified cost function. ....	101

Table 5-26: The DQ model Parameter estimation results for the angular velocity perturbation based on the measured signals considering the modified cost function. ....102

Table 6-1: Average error percentages for the parameter estimation results based on the simulated signals.....103

Table 6-2: Average error percentages for the parameter estimation results based on the measured signals. ....106

Table 6-3: Average error percentages for the parameter estimation results based on the measured signals considering the improvements.....106

## LIST OF ABBREVIATIONS AND SYMBOLS

A	Ampere
$C_p$	Power Coefficient
DFIG	Double-Fed Induction Generator
DQ	Represents the d and q reference axis respectively
GUI	Graphical User Interface
I	Current
IG	Induction Generator
MEX	MATLAB Executable
MIMO	Multi-Input-Multi-Output
Mmf	Magnetomotive Force
Nm	Newton meter
OOP	Object-Oriented Programming
P	Active Power
PM	Permanent Magnet
PV	Photo-Voltaic
Q	Reactive Power
RMS	Root-Mean-Square
rpm	Revolutions per minute
SG	Synchronous Generator
SISO	Single-Input-Single-Output
TSR	Tip Speed Ratio
V	Voltage

# 1 INTRODUCTION

## 1.1 Background

All the world is in energy crisis, while increasing rate of global warming mainly caused by increasing emissions of the greenhouse gasses and especially burning more fossil fuels, will make our planet an unbearable place to live for the next few decades. Under such circumstances, a new phenomenon called climate change can affect our daily life. This will lead to a variation in the statistical distribution of weather patterns. When this lasts for an extended time frame or a change in average weather conditions. Moreover, this phenomenon may result in the time variation of weather around longer-term average conditions [10]. In addition, huge fluctuations of fossil fuel prices have made them vulnerable for almost all industries to consider them as sustainable and reliable energy sources for their future industrial activities.

The only environmental friendly alternative form of the current and mostly air polluting forms of energy sources are renewable energies. Employing the capacities available in nature will contribute to a cleaner and safer environment. Furthermore, it guarantees reliable sources of energy.

Wind energy as one of the main types of renewable energies, can lessen our dependency on fossil fuels and simultaneously reduce the negative impacts of climate change. Moreover, it is plentiful, widely distributed, with the least possible environmental effects. There are two main versions of wind speed conversion systems in terms of speed variation, fixed speed wind generators and variable speed ones. Due to wind's nature, variable speed wind generators can harness more kinetic energy of the wind. Furthermore, they have a reduction in mechanical load, better controllability for active and reactive power, fewer oscillations in output power and better energy yield [1]. Among all the possible configurations of variable speed wind generators, doubly fed induction generators are the most widely wind generators used for units above 1MW [1]. The main advantage of this topology over the other ones is that the power electronic converters only have to utilize a part (about 20-30 %) of the total system power [10]. This causes a cost reduction in comparison to acquiring fully-rated power electronic converters. Studying the dynamic behavior of such wind generators requires an accurate knowledge

regarding the parameters of the machine [3]. These parameters are often unknown or inaccurate mainly because of the following reasons [2]:

- The most accurate models for such systems are usually the higher-order ones which are often the proprietary of the Turbine manufacturer. On the other hand, using lower-order models might cause parameter variation.
- There have been some turbine manufacturers around the world that disappeared from the market but their installed turbines are still in use.
- Even if the parameters of the system are identified during the commissioning, they are still subject to change because of the different operational conditions, aging, temperature, frequency, magnetic saturation, eddy currents.

Therefore, some methods are required to estimate these parameters accurately. Parameter estimation is very important not only for the machine designer but also for the operator of modern drives employing various types of controllers. Moreover, any changes in some certain parameters of the machine can show the existence of some certain types of malfunctions [3]. In addition, most of the conventional methods for determining the machine parameters have the downside that they are based on some hypotheses that are not possible under all conditions. These conventional methods might be expensive, require specially trained staff and preparation of machine in advance before measurements [3].

From the viewpoint of control applications, rotor flux oriented (RFO) control, as the most popular induction machine control method, requires the accurate value of at least some of the machine parameters for a robust control. Any kind of mismatch between the controller parameters and machine values could possibly result in loss of decoupled flux and torque control and consequently detuned operation [4]. Consequently, it is very crucial to estimate the parameters of the machine accurately.

Estimating the parameters of a machine is also useful in case of condition monitoring applications [3]. Condition monitoring is an essential factor in efficient and profitable operation for many industrial processes. Condition monitoring devices provide very crucial information about the health state of the machine and drive for both the designer and operator of the machine. Continuous tracking of the machine and its health condition, leads to obtain the accurate and detailed information about any kind of possible failure or damage or malfunction in the system, like rotor asymmetries, broken rotor bars, broken end-rings, imperfections in

die-cast rotor, inter-turn short circuits, loss of supply phase, asymmetrical supply sources, any kind of dynamic eccentricity and etc. This kind of information will result in a preparation or state of alertness to avoid potentially dangerous situations at early stages prior to getting to a sever stage. In addition, this will contribute to a noticeable reduction in maintenance costs and a better preparation for the next scheduled maintenances. As a result, the system will be much more reliable, which is the desired factor for all of the industrial applications [3].

## 1.2 Review of Related Research

There have been numerous research for estimating the parameters of a wind turbine system, but only a few of them focused on developing and employing a MATLAB toolbox to be used for parameter estimation applications. In [5],[6] different components of a wind turbine system, such as generator, gearbox and turbine blades are modeled and implemented as native C-code S-functions in order to be used as Simulink models for high-speed parameter estimation applications. In addition in [6], parameters of the system are estimated in different perturbation conditions and operating conditions according to the nonlinear least squares method. The most important wind turbine system parameters which can affect the system dynamics are categorized under three main groups [10]:

- Mechanical parameters: Aero turbine parameters and gearbox.
- Controller parameters: The induction generator parameters for the pitch controller and the power electronic converter.
- Electrical parameters: The induction generator parameters including stator and rotor resistances, stator and rotor leakage inductances and magnetizing inductance.

In this study, the main goal is estimating the electrical parameters of the system in practical situations. Therefore, application of the previously proposed native C-code S-function model for fast offline parameter estimation of a doubly-fed induction generator, according to some of squares cost function and numerous input and output topologies and perturbation conditions are considered in this study. A 18.5 kW wounded rotor induction generator is used as the doubly fed induction generator for practical tests. For more simplicity, in all the tests machine is running as an induction generator with the short-circuited rotor windings. Unlike the theoretical based study in [6], in this study, the main objective is to find out that the parameters of the system are capable being readily estimated with a small margin of error in practical situations. This will prove the practical application of the model.



### 1.3 Thesis Contributions

The contributions of this thesis are as follows:

- Forward simulations and parameter estimations for DFIG based on machine's real parameters acquired by the no-load and blocked rotor and DC tests are done. Simulated signals are used and the accuracy of parameter estimation in different perturbation conditions and with different initial conditions are evaluated.
- Practical tests are performed and the measured signals from the machine are substituted for simulated signals. The accuracy of parameter estimation based on real signals are evaluated.
- A comparison between the results of parameter estimation with the simulated signals and the ones with measured signals from the machine is done in order to compare the results and find the accuracy of the model in practical conditions. At the end, recommendations will be presented for future work.

### 1.4 Thesis structure

This thesis consists of six chapters. The following details are:

- *Chapter 1:* This chapter presents the overview, motivation and basic information about the research topic. In addition, the objectives of this research are also presented.
- *Chapter 2:* This chapter introduces a literature review of the primary aims of this study. Various wind turbine system topologies are explained and compared, a brief overview of system identification and parameter estimation, as well as an overview of different parameter estimation methods available in the literature are presented.
- *Chapter 3:* This chapter renders the mathematical modeling of the main components of a wind turbine system and a short summary on the implementation of such models in C-code S-functions in MATLAB Simulink and the parameter estimation process.
- *Chapter 4:* This chapter presents the parameter determination and test bench arrangement. In addition, the Labview software codes and the way they are used to synchronize different measurement tasks with different measurement cards and hardware to read different signals from different sensors are explained completely.
- *Chapter 5:* This chapter introduces the results of the parameter estimations based on both simulations and practical tests, in addition to the methods to improve the obtained results.
- *Chapter 6:* This chapter introduces the results, conclusions and suggests recommendations for future work.

## 2 LITERATURE REVIEW

### 2.1 Introduction

In this chapter, different wind turbine topologies categorised under the fixed speed, two-speed and variable speed wind topologies are shortly reviewed. In addition, a brief review on system identification and parameter estimation. Furthermore, a short review on all the available parameter estimation methods is presented.

### 2.2 Overview of the wind turbine systems topologies

#### 2.2.1 Introduction

In this section, two main types of wind turbine system topologies are shortly presented. In addition, their upsides and downsides are expressed, as well as their prominence according to the current turbine manufacturers around the world.

#### 2.2.2 Fixed speed wind turbine systems

This topology employs an asynchronous generator connected to a fixed frequency electrical network which rotates at quasi-fixed mechanical speed, not depending on the wind speed. The generator shaft is connected to the rotor blades via a gearbox [10]. In order to improve the rotor's power coefficient, a gearbox with the sufficient gear ratio is employed such that it decreases the generator speed and enhances the turbine torque [7], [8]. The schematic picture of this topology is shown in the figure 2-1.

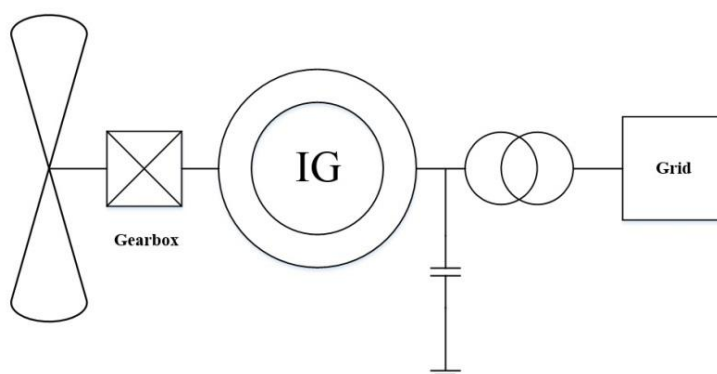


**Figure 2-1: Fixed-speed generator topology.**

The upside of this topology is that due to making use of an asynchronous machine, it does not need synchronization with grid [7],[8]. In addition, it is robust and has lower costs and maintenance.

The main drawback of this topology is the constraints of the asynchronous machine in slip percentage variation which is about 1-2%. This only allows the machine with a very narrow band in operational speed range (about 10%) to draw the optimal power from the wind. Any increase in wind speed out of this band reduces the system efficiency.

The other important disadvantage of this topology is the necessity of the asynchronous machine to the excitation power from the grid. This might become problematic in areas with weaker grids. Therefore, to attenuate this problem capacitors are required to be connected to the circuit. In addition, soft start equipment is considerable to be added to decrease the cut-in current [10], [11].

### 2.2.3 Two-speed induction generator wind turbine systems

This topology is similar to the fixed speed induction generator topology, except that it operates at two optimal wind speeds. It is suitable for areas which have two different average wind speeds during the different times of the year, therefore the annual energy production can be increased by using this topology. The power versus the angular velocity [rpm] generic graph for two-speed induction generators is expressed in the figure 2-2 [10].

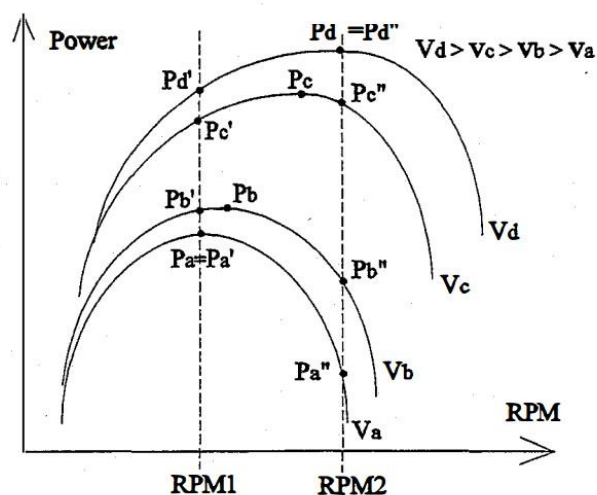


**Figure 2-2: Power versus the angular velocity [rpm] for two-speed induction generator [10].**

There are two ways to perform such an arrangement. The first one is employing dual output drivetrain with two different induction generators which have different synchronous speeds,

and making the shift between them is possible by using a switch. The second way is making use of two sets of windings inside the generator [7], [8], [9]. The schematic picture of the first method is shown in figure 2-3 [10].

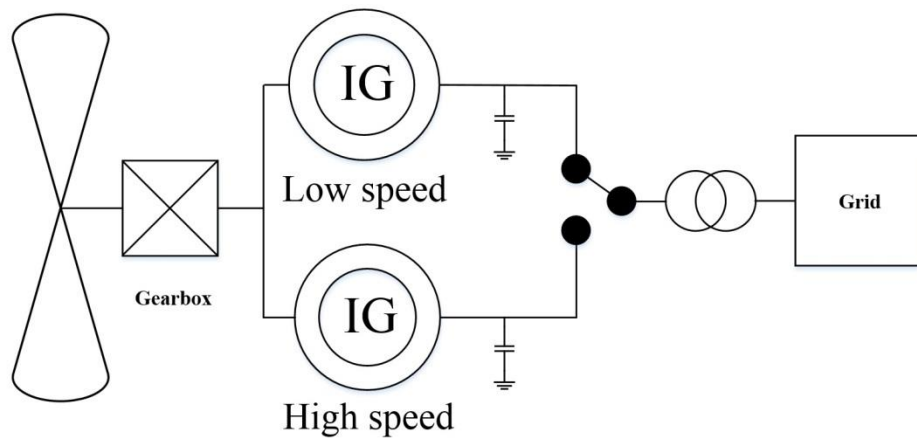


**Figure 2-3: Two-speed generator topology.**

The main upsides of the two-speed generator are that it is more efficient than the fixed speed induction generator and barely reaches the variable speed wind generators efficiency [9]. In addition, it has a reduction in the noise level and also rotor losses [8].

The drawbacks of this topology are that since the wind has a turbulent nature, such systems need regular changes that cause high stress on the system components and make them more vulnerable [9]. Furthermore, similar to the fixed speed wind generators, capacitors are required to provide excitation power for the induction generator.

#### 2.2.4 Variable speed wind turbine systems

The fixed speed wind turbines have major differences with the variable speed wind turbines that basically rises from the technological evolution from one to another. These major differences between them are [10]:

- Pitchable blades control the power in variable speed wind turbines
- Variable speed is feasible by means of the power electronic converters

One of the most widely used types of wind turbines around the world is variable speed ones. They are designed to function in a wider range of wind speeds to reach the maximum possible efficiency. In addition, these turbines are capable of continuously adapting the wind turbine rotational speed  $\omega$ , to the wind speed  $v$  in both accelerating and decelerating modes [8].

In this manner, tip speed ratio  $\lambda$  must remain constant at a predicted value that corresponds to its maximum power coefficient. In addition, the tip speed ratio  $\lambda$  is equal to  $\omega R/v$  where  $R$  is the radius of the rotor blades [9]. Unlike the fixed speed wind turbine systems, in variable speed wind turbines the generator torque is sufficiently constant and varies in the wind speed are compensated the generator speed variation [10].

The variable speed wind turbine generators are technically more complicated than the fixed speed ones. They are typically either provided with induction or synchronous generators connected by a power electronic converter to the power grid. The wind speed variations cause the power to fluctuate, therefore in order to absorb these fluctuations the power electronic converter controls the generator rotor speed and as a result, control the rotor speed.

The main upsides of this technology are higher energy yield, better power quality and reduced mechanical stress on the wind turbine blade. On the other hand, the main drawbacks of this technology are the losses in power electronic converters, more complexity in the system due to the higher number of components and higher costs.

The advent of this technology provided more options for considering in wind turbine topologies and created a new generation of wind turbine concepts by making use of a combination of generator and power electronic converters [7], [8], [9].

#### *2.2.4.1 Variable rotor resistance generator topology*

These versions of wind turbine generators have the similar topology to the fixed speed wind generators, except that it has internal variable resistors rotating with the rotor or external variable resistors connected to its winding terminals (via slip rings) instead of short-circuited rotor winding terminals. As a result in this topology, a the wind generator is capable of operating as a variable speed wind generator by changing the slip. As a result, the generator is capable of operating as a variable speed generator by changing the slip [7]. Unlike the conventional induction generators which are capable of using slip to alleviate the low power fluctuations, an induction generator with variable slip enables the wind turbine system to alleviate higher power fluctuations [15]. Accordingly, these systems are capable of operating in sudden gusts and harnessing the power created in such cases without any negative impacts on output frequency or power. Furthermore, the excessive power dissipates inside the variable resistors and turns into heat [7], [9].

The main upside of this topology is that speed variation is feasible up to about 10%. On the other hand, the downside of this topology is that high slips cause high losses in the rotor circuit and consequently a reduction in system efficiency [15]. In addition, like the fixed speed and two-speed topologies, this system has no control over reactive power. The schematic picture of this topology is shown in the figure 2-4 [10].

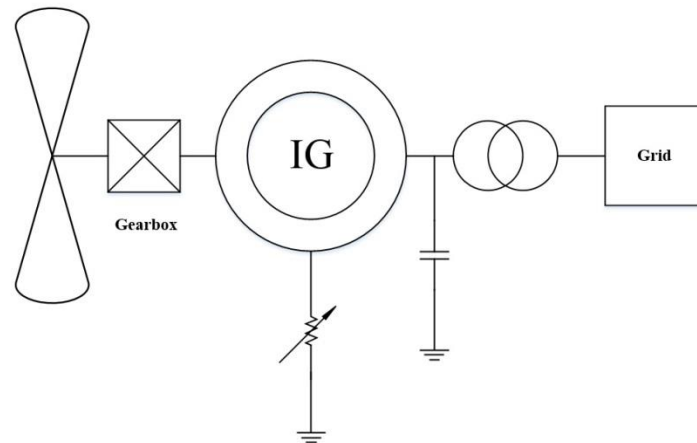


**Figure 2-4: Variable rotor resistance generator topology.**

#### 2.2.4.2 Generator with fully-rated converter topology

In this topology, as it is shown in the figure 2-5, a synchronous, an induction, or a permanent magnet generator is employed and connected to the turbine blades by a gearbox. From the other side, it is connected to a fully-rated power electronic converter [10].

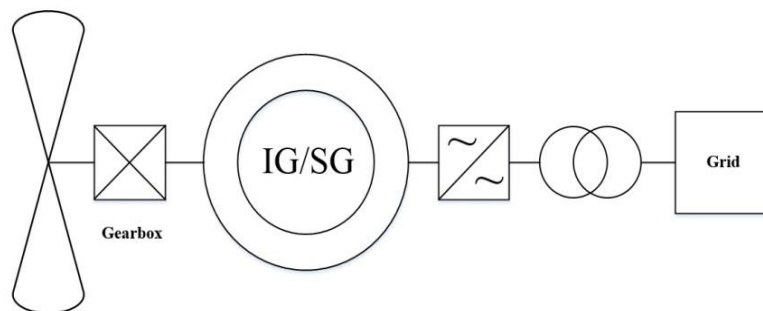


**Figure 2-5: Generator with fully-rated converter topology.**

The main upside of this topology is its variable speed operation ability. Thus, it can achieve its maximum power in different wind speeds while maintaining its value of optimal power coefficient [7]. In addition, its power electronic converters are capable of operating from the

distances which indeed is the desired factor for offshore applications. Moreover, it has the capability of reactive power control [8].

The main drawback of this technology which is very crucial is the reliability of the power electronic converter. Since all the power passes through this converter, any failure in the power electronic converter could result in the whole power getting disconnected from the grid [1]. In addition, fully-rated converters are still relatively expensive, regardless of the all advancements in the new technologies which can reduce the converter costs. Furthermore, they can produce harmonics which needs to be filtered out in order to satisfy the grid requirements. Moreover, they contribute to a portion of the system losses [10].

#### 2.2.4.3 Generator with direct drive and fully-rated converter topology

This topology is a gearless direct drive system. It makes use of a generator with a low synchronous speed and accordingly with higher numbers of poles. A fully-rated power electronic converter is also used in topology. The schematic picture of this topology is shown in the figure 2-6 [10].

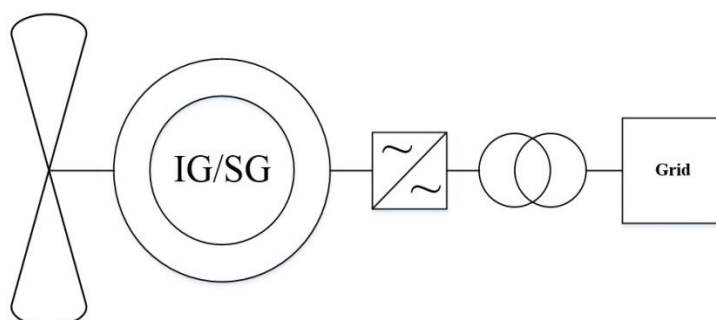


**Figure 2-6: Generator with direct drive and fully-rated topology.**

This generator has a very high efficiency. It has the same upsides mentioned in the previous section about the generator with fully-rated converter topology, in addition to omission of the gearbox. The Gearbox is an important contributing factor to the wind turbine downtime. Thus gearbox omission results in more monetary savings and higher turbine uptime [1]. Moreover, this causes a significant reduction in the noise level and vibrations [8] and lower power losses [7]. The main drawback of this topology is that permanent magnet has very restricted tolerance requirements since the field strength is not controllable which leads to higher costs [1]. Plus, permanent magnets are more expensive than electromagnets. The other downsides of this topology are the issues of reliability and higher costs of the fully-rated power electronic

converters. Moreover, the generators with higher counts of poles are heavier and more expensive.

#### 2.2.4.4 *Direct drive grid-connected slip-synchronous permanent magnet generator topology*

This new concept (SS-PMG) consists of two main permanent magnet machine units, a permanent magnet induction generator combined with a permanent magnet synchronous generator [11]. Unlike the conventional permanent magnet induction generators which are magnetically separated, both machine units are mechanically connected via a common permanent magnet rotor. The permanent magnet synchronous generator is connected to the power grid with its stationary stator, while the permanent magnet induction generator has its short-circuited rotor terminals connected the turbine and operates at slip speed proportionate to the synchronously rotating rotor [11]. Cross-sectional diagram of this new concept is shown in figure 2-7.

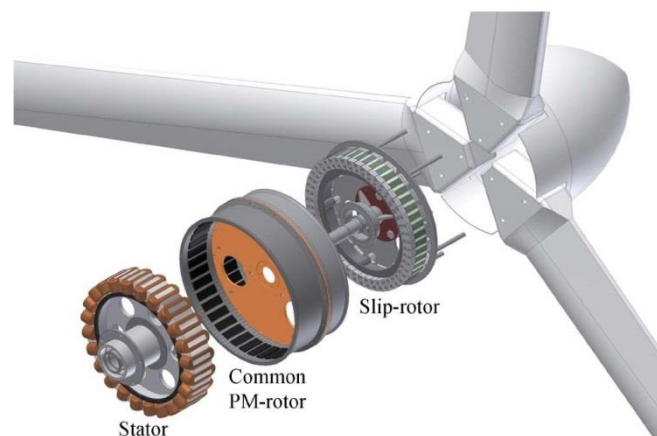


**Figure 2-7: Cross-sectional diagram of the SS-PMG [11].**

The main upsides of this new technology are that omitting the gearbox and power electronic converters as the most important contributing factors wind turbines downtime, results in higher turbine uptime, in addition to higher reliability and lower costs since this topology has fewer components.

The main drawbacks of this technology are due to the use of a permanent magnet, the system has very limited tolerance requirements because of the impossibility of field strength control



which results in higher costs in this regard. In addition, permanent magnet materials are more expensive than electromagnets and also more expensive to maintain or replace their defective ones. Permanent magnet materials need some special coatings on their surface to prevent corrosion which increases the costs. Furthermore, some other problems which might arise are the possibility of oversaturation and in some situations demagnetization of the permanent magnets which can cause overvoltage and undervoltage and control reliability issues [1]. The schematic picture of a SS-PMG topology is shown in the figure 2-8.

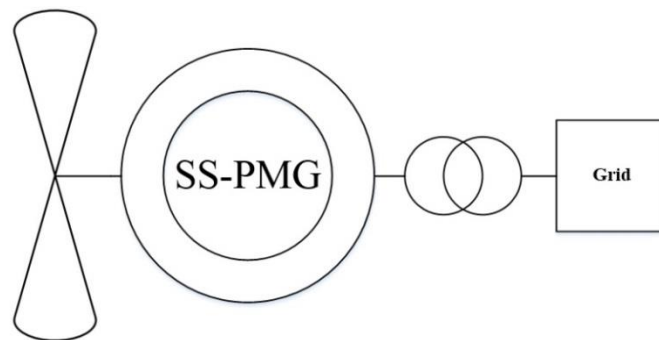


**Figure 2-8: SS-PMG topology [11].**

#### *2.2.4.5 Double-fed induction generator topology*

This topology consists of a double-fed wound rotor induction machine which is connected to a gearbox and then to the wind turbine blades. The stator is connected to the power grid directly, but the rotor terminals are connected to a partially-rated power electronics converter and then to the grid. The power in the rotor has a different frequency than the grid, therefore speed control is possible by changing the rotor frequency. The schematic picture of this topology is shown in the figure 2-9 [10].

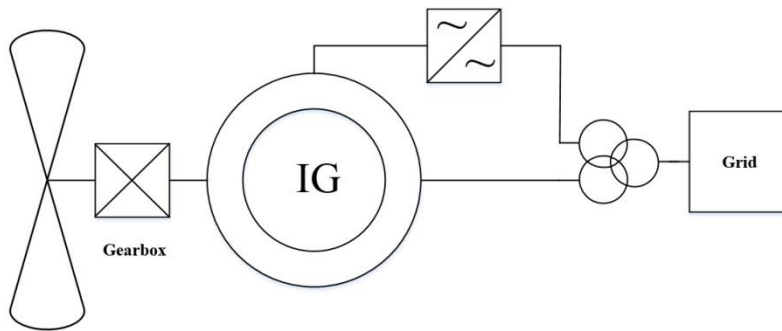


**Figure 2-9: Double-fed induction generator topology.**

The main upsides of this topology are that its variable speed capability enables the system to operate and extract the optimal power at different speeds. In addition, only about one-third of the total power will be transmitted to the grid from a partially-rated power electronic converter, that is less expensive than a fully-rated converter. Plus, the reactive power is also controllable [7].

The main drawbacks of this topology are the higher costs of power electronics in comparison to the topologies with no power electronic converters [8]. In addition, harmonics caused by the power electronic converters must be filtered out in order to satisfy the power grid requirements [7]. And at last, the reliability issues with the slip rings in wounded rotor induction machines are inevitable.

#### 2.2.4.6 Directly coupled synchronous generator with variable gearbox topology

This topology consists of a synchronous generator connected via a variable speed gearbox to the grid [10]. The schematic picture of this topology is shown in the figure 2-10.

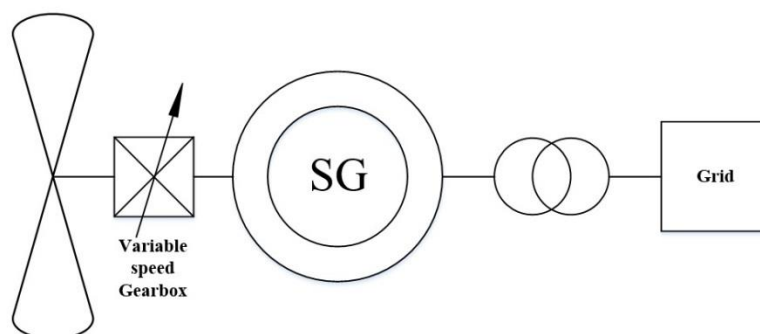


**Figure 2-10: Directly coupled synchronous generator with variable gearbox topology.**

The main upsides of this topology are that due to the elimination of the power electronics converter, all the losses and problems with its generated harmonics and reliability issues are gone. In addition, this topology is capable of capturing more energy in low wind speeds and at least equal energy in high wind speeds in comparison to the topologies that use power electronic converters to control the rotor speed. Therefore it has a higher energy yield [1].

But this topology is more problematic than beneficial. The main drawbacks of this topology are its noticeably higher mechanical losses, high costs and short maintenance cycles [1].

## 2.3 System identification and parameter estimation

### 2.3.1 Introduction

This section reviews the system identification and parameter estimation, in addition to a brief review of the cost functions and optimisation algorithms [14].

### 2.3.2 System identification and parameter estimation

The concept model is defined as “the hypothesized relationship among observed signals of a system” according to [12]. The preferred model for most of the engineering applications is a grey-box mathematical model. A grey-box model represents a model that is constructed from the basic laws of physics, unlike the black-box mathematical models which are constructed from the system identification.

The mathematical models of dynamic systems are classified as follows [13]:

- single input, single output vs. multivariable models
- linear vs. nonlinear models
- parametric vs. nonparametric models
- time-invariant vs. time-varying models
- time domain vs. frequency domain models
- discrete time- vs. continuous time models
- lumped vs. distributed parameter models
- deterministic vs. stochastic models

The main goal of the system identification is to get the mathematical model of a dynamic system based on the input-output data [6]. A black-box model is a model with very little

knowledge about the operation underneath its black-box. The process of system identification is shown in the figure 2-11 [12], [13], [14].

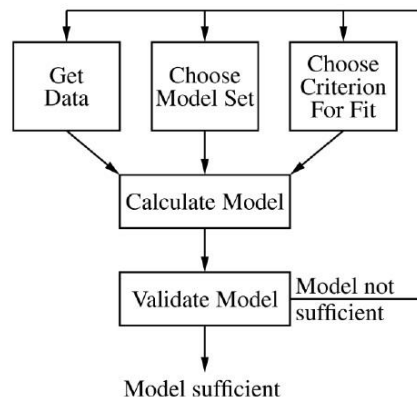


**Figure 2-11: Block diagram of the system identification process [12], [13].**

The *Get data* and the *Choose model set* and the *choose criterion for fit* blocks, all require sufficient information [12]. This information can be acquired from the general understanding of the system or from the data measured from an operational system, experimental measurements on the system, or combined methods between them [14].

The general model chosen for the system identification is a linear time-invariant single-input-single-output system can be represented as follows [12]:

$$A(q)y(t) = \frac{B(q)}{F(q)}u(t) + \frac{C(q)}{D(q)}e(t), \quad (2.1)$$

where

$y(t)$  represents the measured output of the system to be modelled

$u(t)$  represents the measured input of the system to be modelled

$e(t)$  represents the error

$A(q)$ ,  $B(q)$ ,  $C(q)$ ,  $D(q)$ ,  $F(q)$  denote the polynomials.

The main cause of the error could be the external disturbances or inaccuracy in measurement. It can be concluded from the equation (2.1) that depending on the polynomial used in the equation, 32 different types of model sets can be obtained as it is explained in [16, 17].

The elements of the system do not necessarily respect the real system, they are numerical values that represent a mathematical model which behaves similarly to the real system. After the input-output data and the model set are chosen, a cost function is required to determine the

coefficients of the system through an optimization algorithm [13]. This task is performed by the *choose criterion fit* and *calculate the model* blocks.

In order to make sure that the estimation results are extracted from a sufficient model, system identification is necessary. Thus, the *validate model* block have to function in this regard.

Insufficient estimation results might be as a result of one of the following reasons [13]:

- An insufficient model set selection
- The input-output data are insufficient in such a way that they do not excite the system suitably for the purpose of parameter estimation.
- An insufficient selection of the identification criteria for fitting which is not suitable for the chosen model.

An iterative process until reaching the sufficient model by considering all the required adjustments is necessary in this regard.

System identification is required only in cases where the system model is unknown in order to achieve the real system mathematical model, but it is not the case in the wind turbine systems. All the components of the wind turbine systems are made from the laws of physics, therefore the system identification is unnecessary [14].

Regardless of the differences between the system identification and parameter estimation, they both have a common interest [14]. That is to find the coefficients and parameters of the system in a manner that the extracted model behaves similarly to the real system as much as possible [12].

The functional block diagram of the parameter estimation process is shown in figure 2-12 [14].

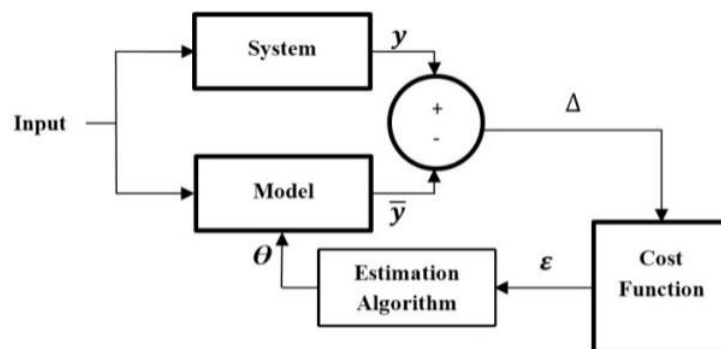


**Figure 2-12: Block diagram of the parameter estimation process [14].**

The *system* block indicates the real system, but the *model* block indicates the model of the system. *Input* indicates the measured input for the system, *y* indicates the real system output

and  $\bar{y}$  the simulated output of the model. The cost function defines the criteria that the model's performance is measured accordingly [14]. Then, the estimation algorithm makes use of this criteria and modifies the system parameters until reaching the desired optimized parameters.

### 2.3.3 Cost functions

Evaluation of how accurate the model simulates the behavior of the real system solidly depends on the difference between the system output and the model output for every data point [13]. This difference is known as the residual. It is very obvious that a more accurate model is a model with a smaller residual for all the data points. Defining a function namely as residual function or cost function enables the model to be optimised by optimising this function. This function can be defined by the summation of the absolute values of all the residuals. The reason for making use of the absolute values is to prevent the negative residuals canceling positive residuals [15], giving

$$\varepsilon = \sum_{i=1}^n |y_i - \bar{y}_i| = \sum_{i=1}^n |\Delta_i| \quad (2.2)$$

where

$y_i$  indicates the output of the real system at the  $i^{\text{th}}$  data point,

$\bar{y}_i$  indicates the output of model at the  $i^{\text{th}}$  data point,

$|\Delta_i|$  indicates the absolute residual at the  $i^{\text{th}}$  data point,

$n$  indicates the number of data points,

$\varepsilon$  indicates the absolute residual error.

In order to minimise the cost function, most of the estimation algorithms employ the derivative of the cost function to determine the parameters that minimises the residual error [13]. The problem that might occur in this regard is that the absolute value is not differentiable at all points. Therefore, the sum of squares criterion is used to solve this problem. In this criterion, the problem of the sign of the residuals is solved by making use of square of the residuals which is differentiable. Then, the residual function for the sum of squares is defined as [12]:

$$\varepsilon = \sum_{i=1}^n (y_i - \bar{y}_i)^2 = \sum_{i=1}^n (\Delta_i)^2. \quad (2.3)$$

In this criterion, since the error is squared the outlier data points which are caused by disturbances or noise make a very noticeable on increasing this squared error [12]. One of the possible methods is to reduce this error is to make use of a weight factor in a way that make

the outlier data weigh less. In equation, the sum of squares residual function is shown where  $w_i$  indicates the weight factor

$$\varepsilon = \sum_{i=1}^n w_i (y_i - \bar{y}_i)^2 = \sum_{i=1}^n w_i (\Delta_i)^2. \quad (2.4)$$

Making use of the sum of the sixth power terms residual function is also one of the possibilities in order to calculate the residual error.

In addition, the sum of squares criterion can be used in a way based on statistical approaches by using residuals gathered in different observations which are distributed identically and with normal distribution functions as it is completely explained in [15].

### 2.3.4 Optimisation algorithms

The cost function needs to be minimised in order to get a better accuracy as it was explained previously. This is carried out by utilizing the optimisation techniques. The term optimisation or programming is defined as the manipulation of the control variables of a function in order to minimise or maximise the function with or without definite constraints [17]. This function is also known as the criterion function, objective function, cost function or energy function [17]. For the purpose of parameter estimation, this function is usually known as objective or cost function. The optimisation algorithm has some specifications in order to be capable of reaching fair results. They are as follows [15]:

- Robustness which means the system is capable of solving a diverse range of problems.
- Efficiency which means efficient use of processor and memory while getting solutions quickly.
- Insensitivity or less sensitivity to errors caused by outlier data or computer implementation, while maintaining the accurate solution.

In practice, it is not feasible to achieve all the above-mentioned properties to its highest level together. In most cases, at least one of them might become undesirable due to the more severe effect of the other properties. In such cases, by decreasing the property with higher impact, the favorable result is obtainable [15].

The tree diagram of the variant optimisation problems in different categories are shown in the figure 2-13 .It is categorised based on the conduct of the objective function relative to the parameters [13].

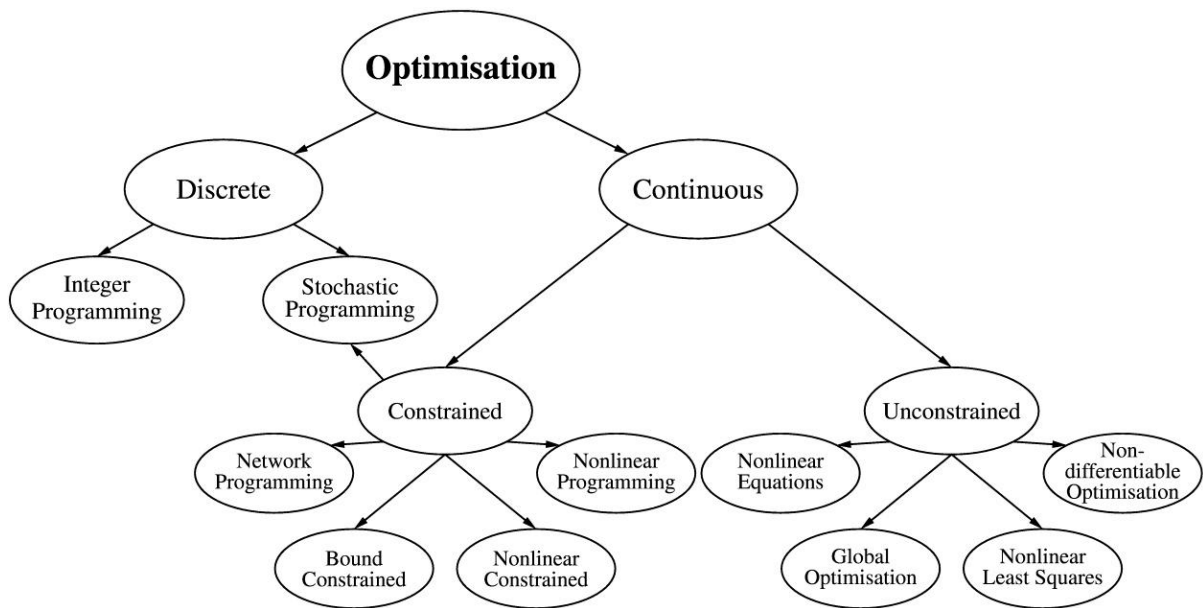


**Figure 2-13: Optimisation tree diagram [13].**

The most crucial considerations in this regard about choosing a sufficient optimisation algorithm are as follows [13]:

- Whether the optimisation is constrained or not.
- Whether the local or global minima or maxima is required.
- Whether the problem is continuous or it is discrete.
- Whether the optimization is stochastic or deterministic.

Improper selection of the optimisation algorithm could end up to a wrong solution with excessive computation time and complication.

There is no universal algorithm suitable for optimisation of all the objective functions and there are very different algorithms as they are explained in many references like [16].

Despite the differences among the optimisation algorithms, all of them have a similar iterative process. It begins with an initial guess for the intended parameters for estimation and then carries on with gradual improvements in each step of iteration until reaching the desired results [15].

The mathematical representation of this process is shown by [16]:

$$x_{i+1} = x_i + \Delta x_i \quad (2.5)$$

where

$x_i$  indicates the current n-element parameter vector



$x_{i+1}$  indicates the next  $n$ -element parameter vector

$\Delta x_i$  indicates the  $n$ -element parameter vector that makes changes to the current values of the parameters.

In addition,  $x_i$  can also be represented by using the step size  $\alpha$  (a scalar), multiplied by a direction vector  $d_i$  which yields

$$x_{i+1} = x_i + \alpha d_i \quad (2.6)$$

The result of  $f(x_i)$  is compared with  $f(x_i + \alpha d_i)$  for the objective function  $f(x)$ . The following measures are taken for each individual case:

- If  $f(x_i + \alpha d_i)$  is smaller than  $f(x_i)$ ,  $x_i + \alpha d_i$  is allocated as the new parameter vector.
- If  $f(x_i + \alpha d_i)$  is bigger than  $f(x_i)$ , the direction  $d$ , step size  $\alpha$ , or both have to be changed.

There are several algorithms available for the direction vector selection. A number of the most important of them are categorised as the Descent algorithms. The two main types of Descent methods are [16]:

- The gradient Descent or the Steepest Descent method
- The Coordinate Descent method.

The first one is where the direction vector for the current point is considered as the negative of the gradient at the same point

$$d_i = -\nabla f(x_i). \quad (2.7)$$

In the second method, a different parameter's direction is chosen as the direction vector for each step and it is usually used as the beginning of a procedure for more complex methods. The most common methods for choosing the sequence of parameters in the Coordinate Descent method are as follows [16]:

- The Cyclic coordinate descent method in which the  $x_1, \dots, x_n$  and  $x_1, \dots, x_n$  are chosen as the parameter sequence.
- The Aitken double sweep method where the chosen parameter sequence is  $x_1, \dots, x_n$  and  $x_n, \dots, x_1$ .
- The Gauss-Southwell in which the largest component of the gradient vector is considered and the parameter corresponding to that is chosen.

After determination of the direction vector  $d$ , the step size  $\alpha$  must be determined by solving the equation

$$\frac{d}{d\alpha} f(x_i + \alpha d_i) = 0. \quad (2.8)$$

Above mentioned equation usually does not have an exact solution, therefore a separate iterative process is required to make sure that  $f(x_i + \alpha d_i)$  is smaller than  $f(x_i)$ . This iterative process starts with is required to make sure that  $f(x_i + \alpha d_i) < f(x_i)$ . For this purpose, the well-known Newton algorithm is explained. In addition, the other most widely used algorithms for solving the least-squares objective function  $f(x_i)$  are explained. This objective function can be expressed as [16]

$$f(x) = \frac{1}{2} \sum_{j=1}^m r_j^2(x). \quad (2.9)$$

where

$r$  indicates the residual smooth function from  $R^n$  to  $R^m$

$$x = [x_1, x_2, \dots, x_n]$$

$m$  indicates the number of data points

$n$  indicates the number of parameters ( $m \geq n$ ).

The residual function can also be expressed in a vector form as

$$r(x) = (r_1(x), r_2(x), \dots, r_m(x))^T \quad (2.10)$$

and the objective function can also be written as  $f(x) = \frac{1}{2} \|r(x)\|^2$ .

In order to further clarify the most well-known algorithms for solving the least-squares objective functions, some other mathematical expressions are required to be defined. The Gradient is defined as [16]

$$\nabla f(x) = J(x)^T r(x) \quad (2.11)$$

and the Hessian is expressed as

$$\nabla^2 f(x) = J(x)^T J(x) + \sum_{j=1}^m r_j(x) \nabla^2 r_j(x) \quad (2.12)$$

where  $J(x)$  is defined as the  $m \times n$  Jacobian matrix as [17]

$$J(x) = \begin{bmatrix} \frac{\partial r_1(x)}{\partial x_1} & \frac{\partial r_1(x)}{\partial x_2} & \dots & \frac{\partial r_1(x)}{\partial x_n} \\ \frac{\partial r_2(x)}{\partial x_1} & \frac{\partial r_2(x)}{\partial x_2} & \dots & \frac{\partial r_2(x)}{\partial x_n} \\ \vdots & \vdots & \ddots & \vdots \\ \frac{\partial r_m(x)}{\partial x_1} & \frac{\partial r_m(x)}{\partial x_2} & \dots & \frac{\partial r_m(x)}{\partial x_n} \end{bmatrix}. \quad (2.13)$$

### 2.3.4.1 Newton method

This algorithm has a linear search method. The main purpose is finding the parameter value which minimizes the given one-dimensional objective function. This parameter value is called  $x_{opt}$  and since it must minimize the objective function. Therefore,  $\dot{f}(x_{opt}) = 0$  [16].

For the objective function, employing the first three terms of the Taylor expansion gives rise to a quadratic model which yields

$$f(x + \Delta x) = f(x) + f'(x)\Delta x + 0.5f''(x)\Delta x^2 \quad (2.14)$$

where  $x_{i+1}$  indicates the new point which will be estimated from the current point,  $x_i$ . In addition,  $\Delta x = x_{i+1} - x_i$ .

The extremum of  $f(x + \Delta x)$  is achievable by solving the following equation in a multi-dimensional scheme as [16]

$$\nabla f(x_i) + \nabla^2 f(x_i)\Delta x = 0, \quad (2.15)$$

where the second derivative  $f''(x)$  is replaced with the Hessian matrix  $\nabla^2 f(x_i)$ , and derivative  $f'(x)$  is replaced with the gradient matrix  $\nabla f(x)$ .

Substituting  $\Delta x = x_{i+1} - x_i$  the equation (2.15) can be rearranged and rewritten. For the new data point to be estimated in a multi-dimensional iteration scheme the equation is derived as follows

$$x_{i+1} = x_i - [\nabla^2 f(x_i)]^{-1}\nabla f(x_i), \quad (2.16)$$

where it converges to  $f'$  root.

The Newton algorithm has the following specifications [17]:

- It is known as a second-derivative algorithm due to use of the second derivative
- It is faster than the first derivative algorithms like the gradient method.
- The function must be twice differentiable which makes its computations more complicated and intense.

### 2.3.4.2 Gauss-Newton method

Many of the least-squares problems are based on this method, where it employs the Newton method by considering an assumption. The assumption is that the residual and Hessian are noticeably small in the proximity of the solution. Therefore this gives rise to the Hessian matrix to be approximated by [17]

$$\nabla^2 f(x_i) \approx J(r(x)) \nabla J(r(x)). \quad (2.17)$$

Substituting (2.11) and (2.16) into (2.17) gives rise to

$$x_{i+1} = x_i - [J(x_i)^T J(x_i)]^{-1} J(x_i)^T r(x_i). \quad (2.18)$$

Approximation of the Hessian matrix is done by neglecting its second term. This results in a noticeable reduction in computational time [15], [17].

This method is suitable for mildly linear systems which need one iteration for linear systems. It is not suitable for badly non-linear systems with big residuals, which cannot converge to local minimums.

The previous two methods (The Gauss-Newton and Newton) are both known as line search techniques. Their process is as followed respectively [17]:

- First finding the search direction  $d_i$  according to (2.6).
- Then finding a suitable step length  $\alpha$  according to (2.6).

The next methods described in the following sections employ the quadratic objective function model [17]. These methods are known as trust-region methods.

### 2.3.4.3 Trust-region method

This method is an iterative method like the Newton and Gauss-Newton methods and results in local minimums. It has a similar process with the previous methods, with a major difference. It starts with defining a region in the proximity of the current iteration where the model is trustworthy such that it represents the objective function in a good manner. Then, the process is followed by the two steps described in the last section [18]. Like the Newton method, the quadratic model  $q_i(\Delta x)$  can be achieved by making use of the first three terms of the Taylor expansion [18] as follows

$$q_i(\Delta x) = f(x_i) + \nabla f(x_i) \Delta x + 0.5 \Delta x^T \nabla^2 f(x_i) \Delta x. \quad (2.19)$$

It must be noted that the model precision depends on whether it is in the vicinity of  $x_i$  or not and preferably it must be as close as possible to  $x_i$ . The region around the point  $x_i$  where the model accuracy is trusted, is known as the trust region and has a radius called as the trust region radius.

This method has the following process respectively [18]:

- The initial value is chosen

- The quadratic model about the initial point approximates the objective function.
- The step size and the direction are achieved by solving the sub-optimization of the (2.19) problem in the trust region.
- In order to make sure that the new point achieved from the sub-optimisation is suitable and not an objective function which is noticeably expensive at an unnecessarily point, an evaluation must be done. This starts by defining the ratio of actual versus predicted reduction of the function  $f$  known as  $\rho_i$  and comparing it with the minimum step ratio  $\eta$  as follows

$$\rho_i = \frac{\text{Actual reduction of } f}{\text{Predicted model reduction of } f} = \frac{f(x_i) - f(x_i + \Delta x_i)}{q_i(0) - q_i(\Delta x_i)}. \quad (2.20)$$

- If  $\rho_i < \eta$ , then the step is rejected and recomputed.
- If  $\rho_i > \eta$ , then the point achieved from the sub-optimisation is allocated as the new point. It must also be noted that usually,  $\eta$  is small enough to prevent from being rejected.

The above-mentioned process reduces the number of expensive approximations of the objective functions but has some drawbacks, including [18]:

- An essential increase in function evaluations.
- The number of iterations might increase.
- Choosing the initial value is very important and different local minimums can be obtained by the different initial values.

Further information about this, like what algorithms are chosen for solving the optimisation of the sub-optimisation problem, the ranges of  $\rho_i$ , and more details can be found in [15].

#### 2.3.4.4 Levenberg-Marquardt method

This method has similarities with the Trust-Region method and uses the same assumptions for the Hessian like the Gauss-Newton.

The model of the trust region is replaced by [15]

$$q_i(\Delta x) = f(x_i) + \Delta x J(r(x))^T r(x) + 0.5 \Delta x^T J(r(x))^T J(r(x)) \Delta x \quad (2.21)$$

where

$$f(x) = \frac{1}{2} \|r(x)\|^2. \quad (2.22)$$

Further readings on this is available in [15], [17].

#### 2.3.4.5 Conclusion

Overall, the Newton and the Gauss-Newton are known as the line search algorithms, while the Trust-Region method and also the Levenberg-Marquardt method are categorised under the trust region algorithms [17].

In addition, the Gauss-Newton and the Levenberg-Marquardt employ the approximation of the Hessian matrix, but all the above-mentioned methods, make use of the quadratic model to model the objective function [15]-[18].

## 2.4 Overview of the parameter identification and estimation methods

### 2.4.1 Introduction

The most widely used method for AC machine control is known as the field oriented (or vector) control. For an induction machine, the vector flux oriented (RFO) needs some of the machine parameters in order to reach a robust control [3].

The machine parameters are subjected to change mostly due to the following reasons [19]:

- Different operational conditions
- Ageing
- Temperature
- Frequency
- Magnetic saturation
- Eddy currents

The parameter variation and mismatch between the machine parameters applied by the control system and the actual parameters of the machine might result in detuned operation of the drive as it is explained in [19].

These parameters must be achieved from measurements during the drive initialization [4]. All the vector controlled induction machines are fed with inverters, therefore some inverter supply based tests have been developed in this regard [4]. These methods are called “offline parameter identification methods”. Moreover, some methods are required to update these parameters identified by the offline methods during the operation of the drive. These methods are called “online parameter estimation methods” [19], [3].

Depending on the vector control scheme, the parameters to be identified offline or tracked online might differ. Considering the drive operating with a constant rated flux reference, the parameters required for identification or estimation are as follows [4]:

- Rated magnetizing inductance
- Stator resistance
- Rotor resistance
- Stator leakage inductance
- Rotor leakage inductance
- Transient stator inductance

If a variable flux reference is the way the drive is operating, including operation in the field weakening region, optimal efficiency drives and etc, the magnetizing curve is also required in addition to above-mentioned parameters [4]. Furthermore, in case of the torque drives widely used in electric or hybrid vehicles, or in any case where the drive controller includes kind of a iron loss compensation, the variation of the obtained iron loss resistance with frequency is also required [19], [20].

There are numerous methods available in the literature regarding the offline parameter identification and online parameter estimation. A comprehensive review of these methods is presented in [19]. These methods can be categorised to the following groups [4]:

- Offline parameter identification techniques
- Online rotor time constant estimation techniques
- Online estimation of stator resistance
- Online compensation of saturation and iron loss

These techniques are briefly explained in the following sections according to the review discussed in [4] and also other sources in the literature.

#### 2.4.2 Offline parameter identification techniques

Many of the manufacturers provide the inverter with a vector controller. The machine and the drive are usually from different manufacturers. Therefore, setting the controller parameters prior to commissioning the machine is not feasible and those parameters must be set onsite while the machine is connected to the inverter. The procedures required to fulfill this task for vector controlled induction machines are called the self-commissioning procedures [4], [21]. This means that the controller automatically detects the required parameters for machine

control by performing an automated test procedure followed by automatic calculation of parameters.

The self-commissioning tests identify the machine parameters at standstill, thus a single phase supply must be connected to the machine. This can be done by both ac and dc power supplies but the dc supply is preferred. The stator resistance is achievable as a result of such tests based on the dc resultant current and applied dc voltage. Determination of the rest of the parameters depends on the transient current response to the applied dc voltage as these self-commissioning schemes can be shown in [22].

In addition, in case of using the single-phase ac power supplies, the parameter identification is possible at standstill by making use of the standstill frequency test shown in [23] or using the rotor time constant (rotor resistance) identification method [24].

There are several methods which are known to be suitable for commissioning but not self-commissioning. For instance, in [25] it shows the application of pseudo-random binary-sequence voltage excitation along with an adaptive observer is employed. In [26] the procedure employs the maximum likelihood to achieve the transfer function by applying a step voltage to the stator terminals and recording the stator current and voltage responses. Then the transfer function is achieved by making use of both the Laplace transformation and maximum likelihood estimation. In [27], the method makes use of the recursive least squares technique.

The above-mentioned methods which are not suitable for self-commissioning can be described as one of the followings [4]:

- Some special conditions are needed to be met during the commissioning.
- The measurement results might need more complicated mathematical processes, in comparison to the self-commissioning methods.

In addition, there are numerous offline identification methods which make the commissioning procedures more complicated. These methods have the capability of identifying the machine's magnetizing curve and the other rated values of the parameters, like in [22], [23] and [28]. In [28], by making use of just one test, the magnetizing curve is identified at standstill. There are other methods where the magnetizing curve identification is done at standstill, like in [29].

There are also some of the parameter identification methods in cases where the commissioning conditions are less strict and the drive is allowed to rotate, like in [30]. In [30], in order to tune the rotor time constant (rotor resistance), the drive must operate in the torque mode and the



rated rotor flux must be considered as a reference. In addition, at a certain speed of operation, an alternating square-wave torque signal is used as the reference and applied to the system.

If the value used in the controller for the rotor resistance (rotor time constant) is true, the actual torque signal must have an alternating square-wave shape similar to the reference signal. Thus, the speed response must look like a triangular function. If not, this mismatch will result in detuned operation of the drive and the actual speed response deviates from a triangular shape signal. In order to avoid this mismatch, the rotor time constant must be tuned in a trial-and-error method until reaching the suitable results [30].

There are commissioning situations which allow the standard locked rotor test and no-load test to be carried out with PWM inverter supply. The parameter identification procedure in [31] is similar to the procedures which use sinusoidal supply. The parameters are identified by making use of the no-load, DC, and the pseudo-locked rotor tests, but in cases which the locked rotor test is not favorable, a new technique for pseudo-locked rotor test is introduced in [32].

The onsite commissioning conditions of the machine cause the magnetizing curve identification to be very straightforward when the machine is allowed to rotate during commissioning [19]. An analytical method for approximating the magnetizing curve is shown in [33], where the fundamental harmonic voltage measurements in steady state are carried out in the field weakening region. This enables identification of the magnetizing curve in a functional form. In addition, it is possible to identify the magnetizing curve by only making use of the signals available inside the drive controller including the stator voltages and the dc link voltage as it is described in [34]. The measurements can be done with the motor in the unloaded situation at the angular velocity at a relatively low speed about 100 r/min. This reduces the effect of mechanical losses, and also iron losses on the identification accuracy [34].

The magnetizing curve identification procedures in [35]-[37] describe the methods which are not very befitting the onsite commissioning of the drive. For example, the reason why the method described in [35] is unsuitable for onsite commissioning is due to the connection of a variable load to the vector controlled induction motor. In [35], only the current measurements are needed and the parameter identification is carried out at standstill. This is done by making use of a closed-loop speed control and all of the phases of the machine are excited. This is similar to the method described in [36] which makes use of a broadband excitation technique in a way that a supply with multiple frequencies is injected to the stator terminals of the machine. In addition, the dynamic and static inductances of the machine are identified in this method. The

method described in [37] is very accurate for measuring the magnetizing inductance but not very suitable in all the practical situations since the neutral point of the stator terminals in a star connection is needed.

The identification of the dynamic or differential inductance is unnecessary since the magnetizing curve inductance is enough for considering the effect of the saturation compensation. Nevertheless, the method described in [38] shows the procedure for identification of the differential inductance.

The iron loss compensation depends on the equivalent iron loss resistance which in fact is a function of the fundamental frequency [20]. In [39], the method describes the procedure resulting in the equivalent iron loss resistance identification during the commissioning of the drive.

In this commissioning condition, the drive is allowed to rotate and the no-load condition is feasible. The drive operates normally with the PWM voltage source inverter during a number of no-load tests at different fundamental frequencies [39]. Then, the equivalent iron loss resistance is calculated after performing the standard no-load test procedure and measuring fundamental harmonic input power by distinguishing between the mechanical losses from the fundamental iron losses [39].

The parameter determination in all offline methods has a certain margin of error and the accuracy crucially depends on the following items [40]:

- Sampling rate
- Quantization errors
- Resolution
- The accuracy of the sensors

In addition, some problems might arise in most of the offline identification methods at standstill and they are known to be as:

- The inverter lock-out time
- Nonlinearity

In the offline identification methods which employ the reconstructed voltage signals, these problems, in fact, deteriorate the estimation accuracy without any information on the inverter voltage drop characteristics [41]. In [42], a technique grounded on the recursive least squares

is proposed to address the above-mentioned problems. Furthermore, several other methods are available based on the commissioning and self-commissioning procedures described in [43].

### 2.4.3 Online rotor time constant estimation techniques

There are several methods regarding the rotor resistance (rotor time constant) online estimation which can be categorised to the following subgroups due to their diversity [4]:

- Spectral analysis techniques
- Observer-based techniques
- Model-reference based adaptive systems
- Other methods

Each of them is reviewed briefly as follows.

#### 2.4.3.1 Spectral analysis techniques

In this group, the current/voltage spectrum is inspected to see the measured response to an existing characteristic harmonic or an intentionally applied test signal [44]. The spectral analysis of the samples taken from the stator currents and voltages are employed to get the parameters. In no-load conditions, the induced currents and voltages of the rotor are zero and subsequently, the slip frequency becomes zero. Therefore, for the purpose of estimating the rotor parameters, a perturbation signal is required. In [44], the injected negative sequence components enable the disturbance for the system. The negative sequence voltage detection results in the rotor resistance determination. In cases which an induction motor is used in such a system as a torque drive, extra caution must be taken into consideration in order to avoid the outer loop from preventing the perturbation from being applied into the system. Thus, the torque-producing action must be undermined or avoided. The interaction between the rotating positive and negative components of MMF causes an intense second harmonic torque ripple which is known as the downside of this method [4].

The online estimation method presented in [45] makes use of a frequency domain  $d$ - $q$  model in a way that the machine torque remains undisturbed. This is feasible by keeping the  $q$ -axis component of the applied negative sequence at zero. Therefore, the machine flux is affected by the  $d$ -axis component. The voltage and current signals are analysed by employing the FFT and the parameters are determined by making use of the fundamental components of the sampled spectral values [45].

The method described in [46], makes use of the online tests resembling the full-load and no-load tests. In [47], the perturbation is provided for the system by applying a pseudo-binary sequence signal to the  $d$ -axis in addition to the correlation of stator current response the  $q$ -axis. Then the rotor time constant is updated by getting the direction from the sign of this correlation. In the method described in [48], the perturbation applied to the stator current component is sinusoidal. Unlike the previous method in [47], which was not suitable under light loads, in this method it is conceivable to estimate the rotor resistance at any load and speed with a good accuracy [48]. The main downside of this method is the extra cost caused by making use of an extra set of flux search coil. Furthermore, the method described in [49] are all similar and related to the previous category. In [50], the rotor resistance gets updated by inspecting the rotor slot harmonics in stator currents.

#### 2.4.3.2 *Observer-based techniques*

This group of methods mainly consists of the followings and their derivatives:

- Kalman filter
- Luenberger observer

The Kalman filter is an algorithm that makes use of a series of measurements over time which includes statistical noise and some other inaccuracies. It is a stochastic method based on designing a control system which faces the following problems [51]:

- Not all state variables are measurable
- The measured state variables are not pure and include noise
- Random disturbances are available in the system

The Kalman filter addresses such problems together. There are two other versions available for the Kalman filter known as the followings [2]:

- Extended Kalman filter (EKF)
- Unscented Kalman filter (UKF)

The extended Kalman filter is the nonlinear type of the Kalman filter and makes use of the linearization around an estimate of the covariance and the current mean [52]. The unscented Kalman filter is used in cases where the transition and observation models of the state are severely non-linear and the EKF results might become very poor. Therefore, to fix this problem a deterministic sampling method which is known as the unscented transform is employed to

select the minimal of the data points around the mean and finally these new data points are increased by non-linear functions and they form a new mean and covariance [53].

The method described in [54] employs the EKF to estimate the machine parameters in normal operating conditions where no test signal is injected into the system. The terminal voltages and currents, in addition to the angular velocity (rotor speed), are required to be measured. Tuning the indirect field oriented controllers can be done automatically by making use of this method. In addition, there are other applications to this method as it is explained in [54].

In [55], the rotor time constant is considered as the 5<sup>th</sup> state variable, with all the stator and rotor current signals. Finally the inverse rotor time constant is achievable by applying the EKF method. The required perturbation for exciting the system is provided externally by making use of the harmonics available in the PWM converter output voltage. The main downside in [55] is making the assumption that all the parameters known and changes in the magnetizing inductance causes high errors and deteriorates the rotor time constant accuracy. In [56], the rotor resistance and the magnetizing inductance are estimated online by the continuous Kalman filter. In this method, the motor magnetizing inductance is estimated along with the rotor resistance, in addition to the rotor time constant. The reason that makes this possible is that the motor flux is followed by the magnetizing inductance [4]. There are other methods regarding the KF method or its derivatives, like [57].

The Luenberger observer is the other observer-based method for parameter estimation [58].

The ELO (Extended Luenberger observer) is used for joint state parameter estimation in [59],[60]. In [59], a deterministic approach is proposed to estimate the motor states and parameters using ELO. In [60], three different full order ELO schemes are proposed and each one of them for one of the following estimations:

- Flux rotor time constant and the rotor flux
- Rotor flux and shaft speed
- Rotor flux, shaft speed, and load torque

In [59],[60] the ELO and EKF are compared together. Due to the nonlinear nature of the induction motor, for the goal of joint state and parameter estimation, the ELO has merits over the EKF. In EKF, the individual time constants' observations do not converge to the optimum point, whereas the ELO is flexible in choosing the gain and the convergence rate is adjustable without unfavorable effects on the observer precision. In addition, in ELO the observer

performance is improvable by only tuning the gain matrix in order to converge faster, unlike the EKF which can give some relatively biased estimation results [4].

The most common problems about the EKF and ELO are as follows [4]:

- Intensity of computations
- Assuming all the inductances as invariables.

Several methods have been proposed so far to address such problems including:

- Identifying the magnetizing inductance [55],[56]
- Considering the Iron loss in the model [61].

#### *2.4.3.3 Model reference adaptive system-based techniques*

This group of estimation techniques is based on the model reference adaptive control methods [62]. The principle of this group of methods is that one quantity is calculated from the control system and is compared to the value calculated from the measured signals. Then, the error signal between them is defined by the difference between the results. Eventually, this error is utilized in the control system to correct the rotor resistance by operating an adaptive mechanism [4].

The most important point about this group of estimation methods is that the model accuracy strongly affects the estimation accuracy. The methods in this group are very diverse. The most widely used method is independent of the stator resistance and is known as the reactive-based approach [63]. In [64], the stator voltage and current measurements are employed by making use of special criterion function. In [65] the adaptive system is based on choosing the air-gap power. In this method, the reference torque and frequency determines the reference air gap power. In addition, the measured input power and an estimation of stator losses determine the actual air gap power. It is also possible to measure the dc link power instead of the machine's input power. The need for estimating the stator losses or the dc link power noticeably reduces the accuracy of this method. There are several other adaptive methods available similar to this which include choosing the following quantities where the adaption mechanism is based on [4]:

- Torque
- Rotor back emf
- Rotor flux magnitude
- $d$  and  $q$  components of the rotor flux

- Stored magnetic energy
- Multiplication of the stator current  $q$  component and rotor flux
- Fundamental RMS voltage of stator
- $d$  and  $q$  component of the stator voltage
- $q$  component of the stator current

All the methods mentioned above have some similar specifications as follows [4]:

- The rotor resistance adaptation and the model used for this purpose is usually applicable in steady-state.
- The quantity for adaptation usually needs the stator voltage from either measured or reconstructed firing signals of the inverters and measured dc link voltage.
- In case of a zero speed and zero load torque usually, the identification does not work properly and accurately.
- Commonly the parameters are considered as constant, thus the accuracy of the model which represent the behavior of the machine noticeably affects the parameter identification. This in fact, is one of the main downsides to this group of techniques.

It must also be noted that because of the possible unfavorable results which might happen in the process of parameter identification, the dependency of such model-based techniques to the changes in the other parameter values can be reduced by taking the magnetizing inductance changes with saturation into account [64], [66].

#### 2.4.3.4 Other methods

The other methods are diverse but many of them can be categorised under the following groups [4]:

- Making use of special switching techniques for current regulated PWM inverters with much simpler computations without any need for a test signal [67].
- Making use of artificial intelligence (AI) by either employing the artificial neural networks [68] or the fuzzy logic [69].
- Joint estimation of rotor speed and time constant (rotor resistance) by using the model-based techniques which apply the sensorless vector control theories [70].

#### 2.4.4 Online estimation of stator resistance

Identification of the rotor time constant in decoupled flux and torque control based on the indirect rotor flux oriented control (IRFOC) is very vital. The IRFOC is an industrial standard set for rotor flux oriented control which employs sensors [4].

There are two main reasons for the increasing interest in online estimation of stator resistance:

- The rotor speed estimation is necessary for most of the methods based on the sensorless vector control since they make use of the induction machine model including the stator resistance. Inaccurate estimation of the rotor resistance might lead to losing stability especially at low speeds [71].
- The stator flux estimation from the measured stator voltages and currents is required for most of the methods based on the direct torque control (DTC). Detuned operation of this control method could be a result of inaccurate estimation of the stator resistance, especially in the lower frequencies.

Methods of this group have similarities with the methods previously mentioned about estimating the rotor resistance, like the observer-based techniques and the model reference adaptive system-based techniques and etc.

#### 2.4.5 Online compensation of saturation and iron loss

In order to include variation in the machine's inductances which is very fast, making use of nonlinear models which are modified for this purpose is very crucial. These models must include the following considerations [4]:

- Saturation to a variable degree
- The correct magnetizing curve
- For the purpose of compensation of the flux saturation, which results in online estimation of the magnetizing curve, the model must include nonlinearity in the magnetizing curve.

Several assumptions must be made in defining a model that includes the above-mentioned considerations. They are as follows [4]:

- It must be possible for the main flux and leakage flux components of both the stator and rotor flux to act and be treated independently from each other.
- Only the main flux saturates but the leakage ones are taken as constants.

If the main goal is only modifying the stator flux estimators, or making use of indirect vector controller in a way that the compensation of the main flux saturation is included in a model, employing the much simpler lower order models can perform this task without any difficulties [72]. On the other hand, in cases where the higher order models are used for rotor flux estimation by employing the  $d$  and  $q$  rotor flux variables, a similar procedure is applied and identifying the magnetizing curve (either offline or during commissioning) is a necessity for being used in a control system [4].



The other methods for estimating the magnetizing curve online, needless of prior knowledge to the magnetizing curve are based on the basic  $d-q$  model of the induction machine and are more accurate in the steady state than transient since they only consider the main flux saturation approximately [66].

Considering the leakage inductance in the machine model enables the rotor leakage flux saturation to be included in the system. Changing the rotor parameters can be taken into account by including the two branches of rotor windings [73]:

- A scheme for compensation of rotor leakage flux saturation and based on the air-gap flux oriented control.
- A scheme based on the modified model of an induction machine for variation of rotor parameters with frequency.

In [73], the method has a better performance than the ones which consider the machine parameters as constants.

All the iron loss compensation methods are vector control approaches modified to be used as model-based methods which include the iron loss. The iron loss must be identified during commissioning, then updated online and modeled by a series of resistances or equivalent resistance [74]. In addition, several other methods are available in the literature, like in [75] that make use of estimating the rotor flux position.

### 3 MODELING AND PARAMETER ESTIMATION METHODOLOGY

#### 3.1 Introduction

In this chapter, different components of a wind turbine system are modeled [14]. In addition, a short review of how they are implemented as C-code and S-functions, and also a brief explanation of the parameter estimation process is presented.

#### 3.2 Mathematical models

##### 3.2.1 System overview

The functional block diagram of the different components of a wind turbine system is shown in figure 3-1. It consists of the following [76]:

- Aerodynamic block: This block models the wind turbine blades element.
- Mechanical block: This block models the gearbox model.
- Electrical block: This block represents the generator model in ABC and DQ reference frame.

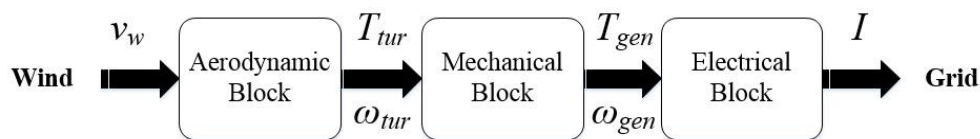


**Figure 3-1: Wind turbine system functional block diagram**

Where  $v_w$  denotes the wind speed in  $m/s$ ,  $T_{tur}$  denotes the turbine mechanical torque in  $Nm$  and  $\omega_{tur}$  denotes the turbine angular velocity in  $rad/s$ ,  $T_{gen}$  denotes the generator mechanical torque in  $Nm$  and  $\omega_{gen}$  denotes the generator angular velocity in  $rad/s$  and  $I$  denotes the stator and rotor currents vector in Amperes. Since the wind turbine control system is beyond the scope of this research, no feedback loop is drawn from the electrical block to the aerodynamic block.

##### 3.2.2 Components Modelling

Based on the wind turbine topology, different components are considerable for modeling. In this study, because the main objective is an evaluation of a previously proposed offline method on parameter estimation of a doubly fed induction generator, therefore the intended components for modeling are aero turbine (aerodynamic block), gearbox and induction generator with exception of the power electronic converter.

### 3.2.2.1 Aerodynamic block

This block absorbs the kinetic energy of the wind by the rotor blades and converts it to mechanical energy by the rotor shaft connected to the axis of rotor blades [10]. Then, based on the system's topology, for power generation section, it can either provide the mechanical energy directly for generator or indirectly via a gearbox.

Kinetic energy ideally absorbable by the turbine blades  $E_K$  [J] is easily obtainable by the following formula [77]:

$$E_K = \frac{1}{2}mv^2 \quad (3.1)$$

where  $m$  is the mass of moving air and  $v$  is the wind speed [ $m/s$ ]. Now, from (3.1) the total mechanical power is:

$$P_T = \frac{1}{2}\dot{m}v^2 \quad (3.2)$$

where  $m$  is the mass flow per second [ $kg/s$ ]. It is obtained as:

$$\dot{m} = \rho Av \quad (3.3)$$

where  $\rho$  and  $A$  are air density [ $kg/m^3$ ] and area swept by the blades [ $m^2$ ] respectively.

The total mechanical power is obtainable by combining (3.2) with (3.3). This yields:

$$P_T = \frac{1}{2}\rho Av^3 \quad (3.4)$$

In fact, extracting all the wind's mechanical power absorbed by turbine blades is feasibly impossible. Extractable energy for each turbine differs than the other ones and it is dependent on the blade's aerodynamics. Therefore, the ratio of extracted mechanical power to the total mechanical power is called power coefficient  $C_p$  [10]. Considering this fact, equation (3.4) can be rewritten for extracted mechanical power  $P$ :

$$P = \frac{1}{2}\rho Av^3 c_p \quad (3.5)$$

The power coefficient can either be provided by the turbine manufacturer or obtained by experimental tests. It basically depends on several parameters, including turbine rotational speed  $\omega$ , wind speed  $v$  and blade pitch angle  $\beta$ . It is very common to combine the rotational speed and wind speed as one variable which is called tip speed ratio (TSR) as  $\lambda$  based on the following equation:

$$\lambda = \frac{R\omega}{v} \quad (3.6)$$

Where  $R$  is the rotor blade's length [ $m$ ].

The following figure 3-2 shows the power coefficient graph with lines for the blade pitch angles as the y-axis and the TSR as the x-axis.

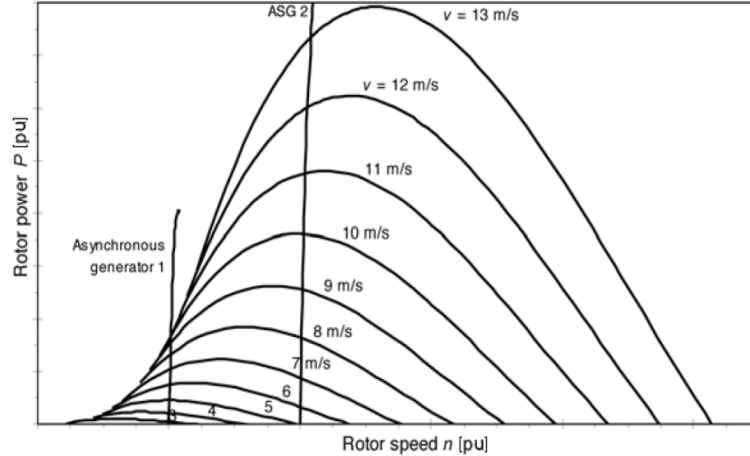


**Figure 3-2: Operating points for a wind turbine with a two-speed induction generator topology [7].**

From the following graph,  $n$  denotes as the rotor speed [ $r/min$ ] can be obtained from:

$$n = \frac{60\omega}{2\pi} \quad (3.7)$$

In addition, the resultant mechanical torque is obtainable from (3.5) by dividing the extracted mechanical power by rotational speed [77]:

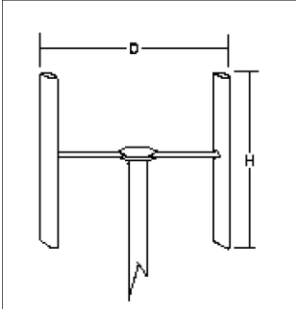
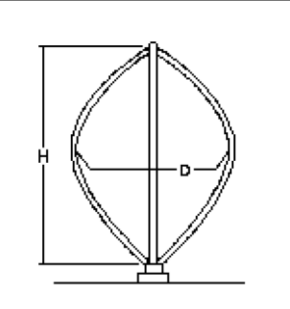
$$T = \frac{0.5\rho Av^3 c_P}{\omega} \quad (3.8)$$

It is worth noting that the swept area  $A$  depends on the rotor blades shape and configuration. For the conventional three blades rotor, the swept area is equal to the area of the hypothetical circle created by rotation of rotor blades over the turbine's horizontal axis where  $R$  as the length of rotor blades is the radius of this circle. Therefore, for conventional rotor blade configuration, the Torque equation in (3.8) can be written as:

$$T = \frac{0.5\rho\pi R^2 v^3 c_P}{\omega} \quad (3.9)$$

The swept area for the other possible configuration of rotor blades like H-rotor and Darrieus rotor is shown in the following Table 3-1 [10]:

**Table 3-1: Swept area for H-rotor and Darrieus rotor [10].**

	
H-rotor $A = DH$	Darrieus rotor $A = 0.65DH$

According to (3.9) the mathematical model of the wind turbine system's rotor blades component is described, with parameters such as blade length  $R$  [m], power coefficient  $C_p$ , inputs as wind speed [m/s] and hub speed [rad/s] (turbine angular velocity) and air density [ $kg/m^3$ ]. In addition, the mechanical torque [Nm] as output.

Different mechanisms for controlling the output power or in other words the output torque of the wind turbine systems exist and mainly concentrated over changing the blade characteristics, like changing the blade pitch angle  $\beta$  [degrees]. In addition, all of them have limitations for cut-in and cut-out wind speed such that if the wind speed is over than the cut-out speed, or is lower than the cut-in wind speed the mechanical brake will halt the blade from rotating [10].

### 3.2.2.2 Mechanical block

As it stated in the description in components modeling section, depends on the wind turbine topology, the aerodynamic block of wind turbine system model can either be connected to the electrical block directly or via mechanical block (gearbox). Here, the gearbox model will be presented for the mechanical block. In addition, for gearless topologies, it is feasible to integrate the mechanical block into the electrical block in order to model the electrical machine's inertia and shaft stiffness.

Gearbox can be modeled in different ways but there are three most common ways, including one-mass, two-mass and finally three-mass models. Due to the higher complexity in three-mass models and also the weakness of one mass model, and the fact that two-mass model can simulate the system dynamics in a reasonable way, the two mass model is chosen in this study.

Simplifying a three-mass model to a two-mass model with a few assumptions is described in [76]. These assumptions are as followed:

- The stiffness  $K_{tur}$  and the damping  $D_{tur}$  of the rotor blade shaft are combined with their equivalent parameter in the generator ( $K_{gen}$  and  $D_{gen}$  respectively) in order to form a single parameter for each stiffness and damping denotes as  $K$  and  $D$ .
- The inertias  $J$  [Nm] of the shaft and the gearbox are relatively small in comparison to the ones for generator and rotor blades. Therefore they are neglected in the two-mass model and only the gear ratio  $k$  is used in this model.

The equivalent damping and stiffness calculations can be expressed as follows [76]:

$$D = D_{tur} + D_{gen}k^2 \quad (3.10)$$

and:

$$K = K_{tur} + K_{gen}k^2 \quad (3.11)$$

A two mass gearbox model is shown in Figure 3.2, which is simplified from a three-mass gearbox model:

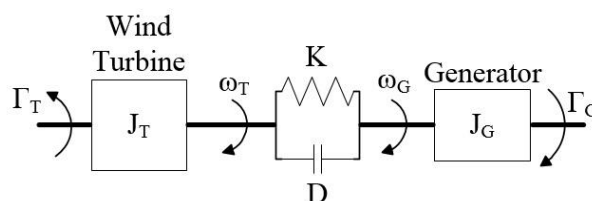


**Figure 3-3: Two-mass gearbox model [5].**

The other important relations between a two-mass model and a three mass one are the following formulas, where  $T$  denotes the rotor blades of the two-mass model and  $G$  refers to the generator on the rotor blades side of the two-mass model and  $tur$  referring to the rotor blades of the three-mass model and  $gen$  as the generator of the three-mass model. In addition,  $J$  refers to inertia,  $\Gamma$  refers to torque and  $\omega$  angular velocity and finally  $\theta$  as angular position [5].

$$\begin{aligned} \Gamma_T &= \Gamma_{rot} & \Gamma_G &= K_{gear}\Gamma_{gen} & J_T &= J_{rot} & J_G &= J_{gen}k_{gear}^2 \\ \omega_T &= \omega_{rot} & \omega_G &= \omega_{gen}/k_{gear} & \theta_T &= \theta_{rot} & \theta_G &= \theta_{gen}/k_{gear} \end{aligned}$$

In addition, dynamic torque equations are achievable based on the model presented in Figure 3.3 [76].

### 3.2.2.3 Electrical block

#### 3.2.2.3.1 Introduction

Based on the wind turbine topology, this block models the generator or generator with power electronic converter which converts the mechanical energy to electrical energy [5] and delivers it to the grid. For Induction generators in a fixed speed topology, only a generator is considered, or an induction generator with a fully-rated converter. For DFIG or doubly fed induction generator, an induction generator with the partially rated converter is considered. DFIG can also operate as an induction generator with no voltage applied to its rotor circuits (short-circuited rotor). Therefore, for more simplicity in this research such configuration is considered and DFIG model is derived from modeling the induction generator's ABC and DQ models with short-circuited rotor windings.

#### 3.2.2.3.2 Doubly fed induction generator ABC model

The following figure 3.4 shows the DFIG's simplified diagram. Subscripts a,b,c and refer to different phases and s,r refer to rotor and stator windings [5],[78].

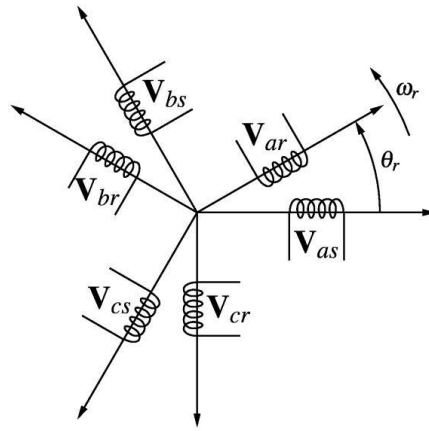


Figure 3-4: Three-phase machine diagram [78].

Equations for terminal voltages with assuming a sinusoidal magnetomotive force and neglecting the saturation and core losses are as follows, where the variable  $r$  stands for resistance and  $\lambda$  for flux linkage, also  $v$  stands for voltage and  $i$  for current [78]:

$$\begin{aligned} v_{as} &= r_{as}i_{as} + \frac{d\lambda_{as}}{dt} & v_{ar} &= r_{ar}i_{ar} + \frac{d\lambda_{ar}}{dt} \\ v_{bs} &= r_{bs}i_{bs} + \frac{d\lambda_{bs}}{dt} & v_{br} &= r_{br}i_{br} + \frac{d\lambda_{br}}{dt} \end{aligned} \quad (3.12)$$

$$v_{cs} = r_{cs}i_{cs} + \frac{d\lambda_{cs}}{dt} \quad v_{cr} = r_{cr}i_{cr} + \frac{d\lambda_{cr}}{dt}$$

Flux linkage for each phase is dependent on self-inductance and leakage inductance and also the mutual inductance with the other windings. For phase A, flux linkage is:

$$\lambda_{as} = L_{asas}i_{as} + L_{asbs}i_{bs} + L_{ascs}i_{cs} + L_{asar}i_{ar} + L_{asbr}i_{br} + L_{ascr}i_{cr} \quad (3.13)$$

The terminal voltage matrix is obtainable by substituting the flux linkage equation for each phase in terminal voltage equations (3.12) which yields the followings:

$$\begin{bmatrix} v_{as} \\ v_{bs} \\ v_{cs} \\ v_{ar} \\ v_{br} \\ v_{cr} \end{bmatrix} = \begin{bmatrix} r_{as} & 0 & 0 & 0 & 0 & 0 \\ 0 & r_{bs} & 0 & 0 & 0 & 0 \\ 0 & 0 & r_{cs} & 0 & 0 & 0 \\ 0 & 0 & 0 & r_{ar} & 0 & 0 \\ 0 & 0 & 0 & 0 & r_{br} & 0 \\ 0 & 0 & 0 & 0 & 0 & r_{cr} \end{bmatrix} \begin{bmatrix} i_{as} \\ i_{bs} \\ i_{cs} \\ i_{ar} \\ i_{br} \\ i_{cr} \end{bmatrix} + p \left\{ \begin{bmatrix} L_{asas} & L_{asbs} & L_{ascs} & L_{asar} & L_{asbr} & L_{ascr} \\ L_{bsas} & L_{bsbs} & L_{bscs} & L_{bsar} & L_{bsbr} & L_{bscr} \\ L_{csas} & L_{csbs} & L_{cscs} & L_{csar} & L_{csbr} & L_{cscr} \\ L_{aras} & L_{arbs} & L_{arcs} & L_{arar} & L_{arbr} & L_{arcr} \\ L_{bras} & L_{brbs} & L_{brcs} & L_{brar} & L_{brbr} & L_{brcr} \\ L_{cras} & L_{crbs} & L_{crcs} & L_{crar} & L_{crbr} & L_{crCs} \end{bmatrix} \begin{bmatrix} i_{as} \\ i_{bs} \\ i_{cs} \\ i_{ar} \\ i_{br} \\ i_{cr} \end{bmatrix} \right\} \quad (3.14)$$

where  $p$  represents the time derivative, and the subscripts  $asas$ ,  $bsbs$ ,  $cses$ ,  $arar$ ,  $brbr$ ,  $crcr$  refer to the self-inductances, in addition to the leakage inductances and the other subscripts represent the mutual inductances [78].

The matrix equation format of the equation (3.14) can be expressed as follows:

$$\mathbf{V} = \mathbf{RI} + \frac{d\mathbf{L}}{dt}\mathbf{I} + \mathbf{L}\frac{d\mathbf{I}}{dt} \quad (3.15)$$

All the inductances are a function of  $\theta_r$ . The chain rule is applied to the time derivative of the induction matrix in (3.15) which yields:

$$\frac{d\mathbf{L}}{dt} = \frac{d\mathbf{L}}{d\theta_r} \frac{d\theta_r}{dt} = \frac{d\mathbf{L}}{d\theta_r} \omega_r \quad (3.16)$$

Combining the last two equations yields:

$$\mathbf{V} = \mathbf{RI} + \frac{d\mathbf{L}}{d\theta_r} \omega_r \mathbf{I} + \mathbf{L}\frac{d\mathbf{I}}{dt} \quad (3.17)$$

If the rotor and stator are magnetically symmetrical, resistance and inductance matrix are obtainable by:



$$\mathbf{R} = \begin{bmatrix} r_s & 0 & 0 & 0 & 0 & 0 \\ 0 & r_s & 0 & 0 & 0 & 0 \\ 0 & 0 & r_s & 0 & 0 & 0 \\ 0 & 0 & 0 & r_r & 0 & 0 \\ 0 & 0 & 0 & 0 & r_r & 0 \\ 0 & 0 & 0 & 0 & 0 & r_r \end{bmatrix} \quad (3.18)$$

and

$$\mathbf{L} = \begin{bmatrix} L_s & -0.5M_{sr} & -0.5M_{sr} & M_{sr}a_1 & M_{sr}a_2 & M_{sr}a_3 \\ -0.5M_{sr} & L_s & -0.5M_{sr} & M_{sr}a_3 & M_{sr}a_1 & M_{sr}a_2 \\ -0.5M_{sr} & -0.5M_{sr} & L_s & M_{sr}a_2 & M_{sr}a_3 & M_{sr}a_1 \\ M_{sr}a_1 & M_{sr}a_3 & M_{sr}a_2 & L_r & -0.5M_{sr} & -0.5M_{sr} \\ M_{sr}a_2 & M_{sr}a_1 & M_{sr}a_3 & -0.5M_{sr} & L_r & -0.5M_{sr} \\ M_{sr}a_3 & M_{sr}a_2 & M_{sr}a_1 & -0.5M_{sr} & -0.5M_{sr} & L_r \end{bmatrix} \quad (3.19)$$

where:

$$\begin{aligned} L_s &= L_{ls} + M_{sr} \\ L_r &= L_{lr} + M_{sr} \\ a_1 &= \cos(\theta_r) \\ a_2 &= \cos\left(\theta_r + \frac{2\pi}{3}\right) \\ a_3 &= \cos\left(\theta_r - \frac{2\pi}{3}\right). \end{aligned}$$

Rearranging the (3.17) in state variable format with current as a variable:

$$\frac{dI}{dt} = L^{-1} \left\{ -R - \omega_r \frac{dL}{d\theta_r} \right\} I + L^{-1}V \quad (3.20)$$

Instantaneous power is also obtainable from [5]:

$$P_{ins} = I^T V = I^T R I + I^T \frac{dL}{d\theta_r} \omega_r I + I^T L \frac{dI}{dt}. \quad (3.21)$$

Dividing the mechanical power by the mechanical speed gives the mechanical torque [Nm]:

$$T = \frac{P_{mech}}{\Omega_r} \quad (3.22)$$

Where  $\Omega_r = 2 \frac{\omega_r}{P}$ .

Substituting the mechanical torque and mechanical speed gives rise to:

$$T = \frac{P}{2} I^T \frac{dL}{d\theta_r} I \quad (3.23)$$

further simplification of the torque by using the inductance matrix and matrix operations yields to the following equation for generator torque [78]:

$$T = -\frac{P}{2}M_{sr} \left\{ (i_{as}i_{ar} + i_{bs}i_{br} + i_{cs}i_{cr})\sin(\theta_r) + (i_{as}i_{br} + i_{bs}i_{cr} + i_{cs}i_{ar})\sin\left(\theta_r + 2\frac{\pi}{3}\right) + (i_{as}i_{cr} + i_{bs}i_{ar} + i_{cs}i_{br})\sin\left(\theta_r - 2\frac{\pi}{3}\right) \right\} \quad (3.24)$$

### 3.2.2.3.3 Doubly fed induction generator Direct–Quadrature (DQ) model

Here, the DFIG is modeled by converting a three-phase machine to a two-phase machine via a DQ reference frame [80]. Figure 3-4 shows a two-phase machine.

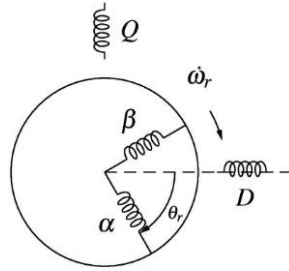


Figure 3-5: Two-phase machine diagram [80].

The DFIG terminal voltages are given by the following equations [79], [80]:

$$\begin{aligned} v_D &= R_{DD}i_D + p(L_{DD}i_D) + p(L_{DQ}i_Q) + p(L_{D\alpha}i_\alpha) + p(L_{D\beta}i_\beta) \\ v_Q &= p(L_{QD}i_D) + R_{QQ}i_Q + p(L_{QQ}i_Q) + p(L_{Q\alpha}i_\alpha) + p(L_{Q\beta}i_\beta) \\ v_\alpha &= p(L_{\alpha D}i_D) + p(L_{\alpha Q}i_Q) + R_{\alpha\alpha}i_\alpha + p(L_{\alpha\alpha}i_\alpha) + p(L_{\alpha\beta}i_\beta) \\ v_\beta &= p(L_{\beta D}i_D) + p(L_{\beta Q}i_Q) + p(L_{\beta\alpha}i_\alpha) + R_{\beta\beta}i_\beta + p(L_{\beta\beta}i_\beta) \end{aligned} \quad (3.25)$$

Due to the uniformity of the air gap, by neglecting the saturation all the self-inductances are independent of the angular position (unlike the ABC model) [79]. In addition by assuming the windings as balanced ones,  $L_{DD} = L_{QQ}$ ,  $L_{\alpha\alpha} = L_{\beta\beta}$ ,  $R_{DD} = R_{QQ}$ ,  $R_{\alpha\alpha} = R_{\beta\beta}$ . Therefore, such qualities are substituted by  $L_S, L_R, R_S, R_R$  respectively. Because of the symmetry in arrangement,  $L_{\alpha\beta} = L_{\beta\alpha} = 0$  and also  $L_{QD} = L_{DQ} = 0$ . Therefore:

$$\begin{aligned} v_D &= R_D i_D + p(L_S i_D) + p(L_{D\alpha} i_\alpha) + p(L_{D\beta} i_\beta) \\ v_Q &= R_S i_Q + p(L_S i_Q) + p(L_{Q\alpha} i_\alpha) + p(L_{Q\beta} i_\beta) \\ v_\alpha &= p(L_{\alpha D} i_D) + p(L_{\alpha Q} i_Q) + R_r i_\alpha + p(L_r i_\alpha) \\ v_\beta &= p(L_{\beta D} i_D) + p(L_{\beta Q} i_Q) + R_r i_\beta + p(L_r i_\beta) \end{aligned} \quad (3.26)$$

The remaining mutual inductances are all functions of rotor position and thus functions of time [80]. By assuming their variation in a sinusoidal way, and also the other assumptions about a uniform air gap and symmetric windings, the maximum value for all of them is the same. Therefore [79]:

$$\begin{aligned}
 v_D &= R_S i_D + L_S p i_D + M_p (\cos \theta_r i_\alpha) + M_p (\sin \theta_r i_\beta) \\
 v_Q &= R_S i_Q + L_S p i_Q - M_p (\sin \theta_r i_\alpha) + M_p (\cos \theta_r i_\beta) \\
 v_\alpha &= M_p (\cos \theta_r i_D) - M_p (\sin \theta_r i_Q) + R_r i_\alpha + p (L_r i_\alpha) \\
 v_\beta &= M_p (\sin \theta_r i_D) - M_p (\cos \theta_r i_Q) + R_r i_\beta + p (L_r i_\beta)
 \end{aligned} \tag{3.27}$$

Two new variables  $i_d$  and  $i_q$  based on the previous equations can be defined as follows [80]:

$$\begin{bmatrix} i_d \\ i_q \end{bmatrix} = \begin{bmatrix} \cos \theta_r & \sin \theta_r \\ -\sin \theta_r & \cos \theta_r \end{bmatrix} \begin{bmatrix} i_\alpha \\ i_\beta \end{bmatrix} \tag{3.28}$$

Equation (3.28) can be expressed in the symbolic format as follows [79]:

$$[i_{dq}] = S [i_{\alpha\beta}] \tag{3.29}$$

Substituting  $i_d$  and  $i_q$  in (3.27) yields:

$$\begin{aligned}
 v_D &= R_S i_D + L_S p i_D + M_p i_d \\
 v_Q &= R_S i_Q + L_S p i_Q + M_p i_q
 \end{aligned} \tag{3.30}$$

Currents  $i_\alpha$  and  $i_\beta$  are obtainable from (3.28). This yields:

$$\begin{aligned}
 i_\alpha &= \cos \theta_r i_d - \sin \theta_r i_q \\
 i_\beta &= \sin \theta_r i_d + \cos \theta_r i_q
 \end{aligned} \tag{3.31}$$

Substituting in  $i_\alpha$  and  $i_\beta$  in (3.27) gives the following:

$$\begin{aligned}
 v_\alpha &= M_p (\cos \theta_r i_D) - M_p (\sin \theta_r i_Q) + R_r (\cos \theta_r i_d - \sin \theta_r i_q) + L_r p (\cos \theta_r i_d - \sin \theta_r i_q) \\
 v_\beta &= M_p (\sin \theta_r i_D) + M_p (\cos \theta_r i_Q) + R_r (\sin \theta_r i_d + \cos \theta_r i_q) + L_r p (\sin \theta_r i_d + \cos \theta_r i_q)
 \end{aligned}$$

(3.32)

Two new variables are defined as  $v_d$  and  $v_q$ . This gives rise to:

$$v_d = \cos\theta_r v_\alpha + \sin\theta_r v_\beta \quad (3.33)$$

$$v_q = -\sin\theta_r v_\alpha + \cos\theta_r v_\beta$$

After further simplifications, the following equations are obtainable [5]:

$$P_{ins} = I_{DQdq}^T R I_{DQdq} + \omega_r I_{DQdq}^T H I_{DQdq} + I_{DQdq}^T L \dot{I}_{DQdq} \quad (3.34)$$

$$P_{mech} = \omega_r I_{DQdq}^T H I_{DQdq} \quad (3.35)$$

And the electromagnetic torque is achievable by [5]:

$$T = \frac{P}{2} I_{DQdq}^T H I_{DQdq} = \frac{P}{2} M (i_D i_q - i_Q i_d) \quad (3.36)$$

### 3.3 Overview of MATLAB C-code and S-functions

This section presents a brief about an overview of the functionality of MATLAB S-function according to [6]. Intensive simulations along with the optimisation processes require longer time. In order to address this issue, MATLAB SIMULINK has the capability of employing models implemented as C-codes and S-functions. This is a desired factor for the parameter estimation purposes to reduce the total estimation time. This is shown in Figure 3-6 [6].

Coding the MATLAB S-functions is possible in programming languages like C, Ada, Fortran or M. This coding must be performed in a specific MATLAB format and compiled as a MEX-file [81].

The way all the parameters of each S-function block is set is shown in Figure 3-6 [6]. The S-function field receives all the parameters needed for the model in a vector form. The Figure 3-6 that shows the functionality of C-code S-function consists of three main sections as follows [6]:

- Initialisation: Includes the general settings for parameters, states, initial conditions and input and output ports, timing, and data verification.
- Simulation: Includes the simulation loop and the conditions for the simulation loop.
- Termination: Shows the finishing point of the C-codes and S-functions flow diagram.

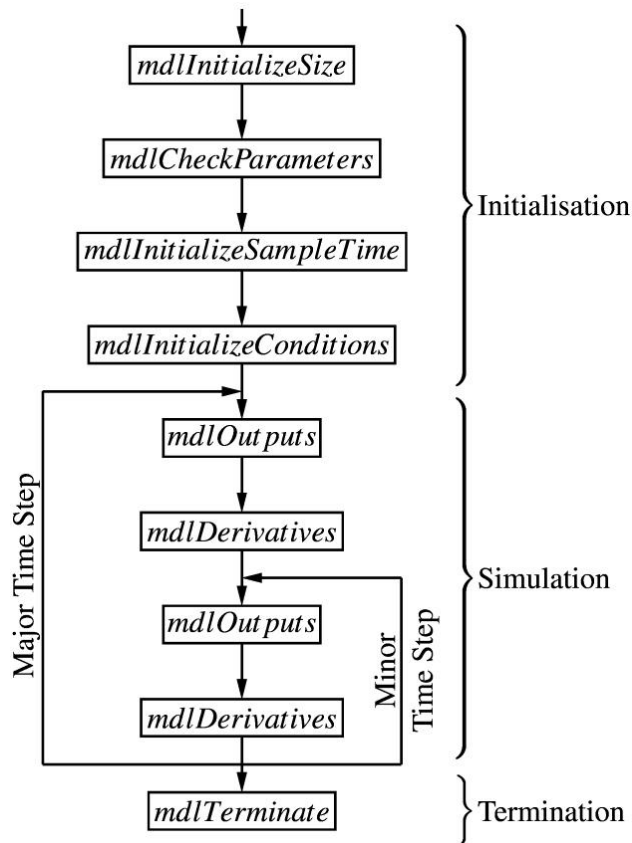


**Figure 3-6: Flow diagram of the main functional components of C-code S-function [6].**

Implementation of models as S-functions is completely described in [6].

### 3.4 Parameter Estimation Process

The Parameter estimation process in this study is described by Fig. 3-6 [14], [6]. The System block demonstrates a forward simulation filled with predetermined parameters. The Model block refers to the same model implementation while the parameters are estimated by making use of the chosen optimization strategy [14]. The multivariate output signals of the System and Model block are defined by  $y$  and  $\bar{y}$  respectively. Furthermore, the residuals, known as the instantaneous difference between the simulated output signals from the System and Model blocks, are denoted by vector  $\Delta$ . The objective function to be minimised by the optimisation algorithm is demonstrated by the Cost Function block [14].

Due to the practical-based nature of this study, actual signals measured from the machine are substituted for the forward simulation, while actual parameters identified during commissioning by performing the tests in are substituted for the predetermined parameter set. Therefore in the estimations based on the actual signals, the System block and its input and

outputs in fig. 3-6 are replaced by the measurement results. Offline parameter estimation means that once the parameters are identified during commissioning, they are considered constant and as actual values. Then, the estimations results are compared to them in order to validate the estimation accuracy. The parameter estimation block diagram is shown in figure 3-6 [6].

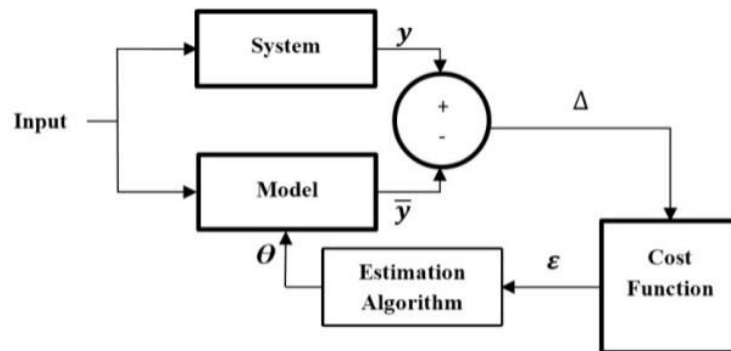


**Figure 3-7: Parameter estimation process diagram [6].**

After the determination of actual parameters through various tests during commissioning, a special perturbation condition for each new test is chosen and the test is conducted for a predetermined period of time. All of the DFIG's stator and rotor voltage and current signals, as well as the torque and angular velocity signals, are measured and saved simultaneously for that period of time. These signals are then fed into the algorithm shown in fig 3-6. In order to determine the cost function from the torque and the current output signals, the sum of squares method and subsequently Levenberg-Marquardt and Trust Region estimation algorithms are employed [17]. Moreover, for the purpose of solving the Least Square (LS) objective functions, the well-known Levenberg-Marquardt and Trust Region estimation algorithms [17], implemented in MATLAB Simulink parameter estimation toolbox are utilized in this study.

## 4 PARAMETER DETERMINATION AND TEST ARRANGEMENT

### 4.1 Introduction

According to the thesis structure stated in chapter 1, in this chapter information about the components of the test bench, sensors and data acquisition hardware system used in this arrangement are presented. In addition, a short review of the data acquisition software and the way it is used to acquire and synchronize different signals is presented. A simplified schematic picture of the test bench is shown in the figure 4-1.

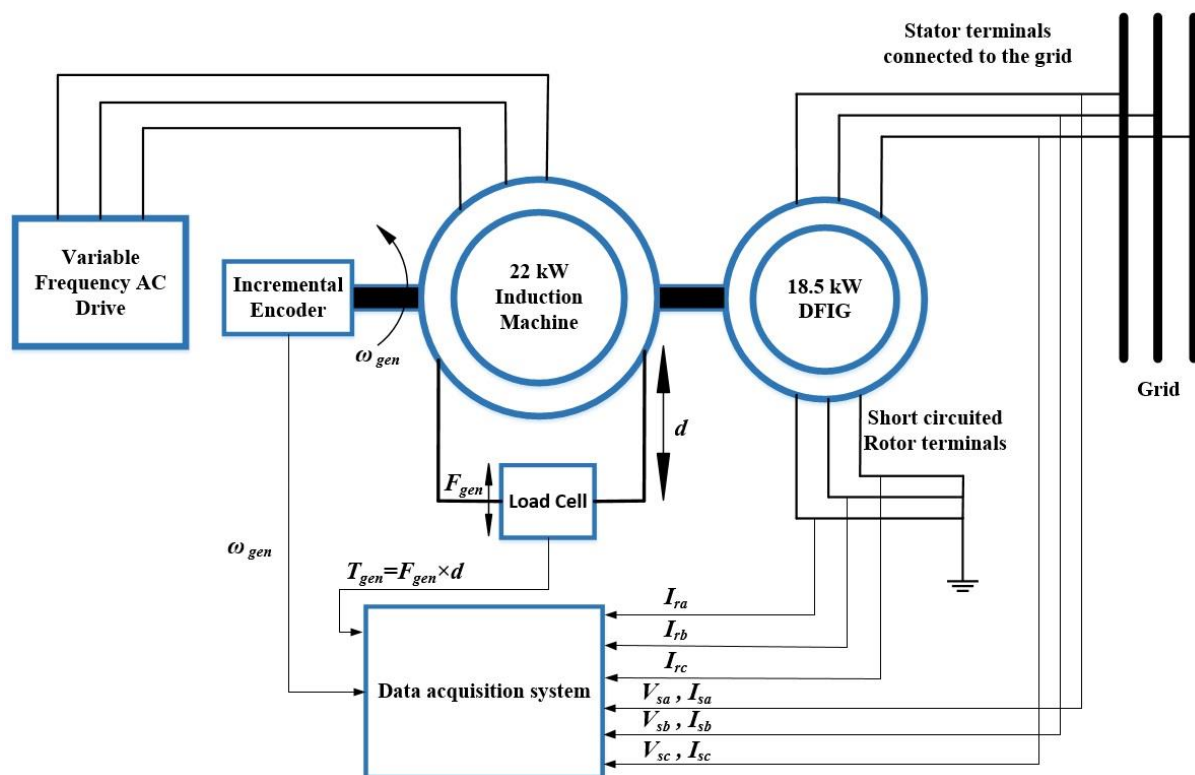


**Figure 4-1: Simplified schematic picture of the test bench.**

Due to the practical objective of this research, the test setup shown in Figure 4-1 is considered to perform different tests with different perturbation signals to excite system eigenvalues for purpose of parameter estimation. Since the 18.5 KW slip ring induction machine should operate as an induction generator, another machine is required to drive its shaft and provide mechanical energy for it. So, a 22 kW induction motor will act as the prime mover in this setup. In addition, a variable speed AC drive is required in this setup, as well as three-phase excitation voltage for the induction generator and also load cell and incremental encoder. First, the machine

parameters will be identified during the commissioning by performing the tests fully described in [82] and they will be considered as machine's actual parameters. Then a special perturbation condition for each new test will be chosen and the test will be conducted for a predetermined period of time. All of the induction generator's stator and rotor voltage and current signals, as well as the torque and angular velocity signals, will be measured and saved simultaneously for that period of time. Later on, these signals will be fed into the algorithm stated in chapter 3 of this study in order to determine the cost function based on the sum of squares method and subsequently Levenberg-Marquardt and Trust Region estimation algorithms [17] will be employed in order to solve Least Square (LS) objective functions as it is mentioned in chapter 2. Finally, estimation results will be compared to the parameters identified during commissioning to verify the method accuracy.

#### 4.2 18.5 kW wounded rotor induction machine

This 18.5 kW slip ring induction machine is used in order to operate as doubly fed induction generator with short-circuited rotor. This machine has the following specifications highlighted in Table 4-1 according to the manufacturer.

**Table 4-1: SPER 200 L4, 18.5 kW wounded rotor induction machine data provided by VEM.**

Type	P [kW]	n [rpm]	$\eta$ [%]	$\text{Cos}\varphi$ [-]	$I_1$ [A]	$M_k/M_n$ [-]	$I_2$ [A]	$U_2$ [V]	S [-]	$R_2$ [ $\Omega$ ]	J [kgm <sup>2</sup> ]	m [kg]
SPER 200 L4	18.5	1470	89	0.86	35	3.8	52	220	Y	0.0346	0.33	280

In the above table, P denotes the rated power in kW, n denotes the rated angular velocity in rpm,  $\eta$  denotes the machine efficiency, and  $\text{Cos}\varphi$  is the power factor. In addition,  $I_1$  and  $I_2$  denote the rated stator and rotor currents in Amperes.  $M_k/M_n$  denotes the ratio of the start-up torque to the nominal torque. Furthermore,  $U_2$  and  $R_2$  denote the rotor voltage and rotor resistance in volts and ohms respectively. Moreover, S denotes the connection type, J denotes the moment of inertia in kgm<sup>2</sup> and m denotes the whole mass of the machine in kg.

The machine nameplate is shown in figure 4-2.





**Figure 4-2: SPER 200 L4, 18.5 kW wound rotor induction machine nameplate.**

#### 4.2.1 18.5 kW Induction machine parameter determination

The machine parameters are achievable by some tests including the DC test, no load test and blocked rotor test as it is stated in [82].

##### 4.2.1.1 DC tests

The aim of this test is to calculate the stator resistance of the machine based on the measured voltage and current [82]. The stator terminals of the 18.5 kW induction machine are excited by a DC power source while rotor terminals are short-circuited such that the nominal currents are drawn from the stator windings. Due to the limitation of the current in the available DC power source in the lab facilities, DC tests are done in lower currents than the nominal current. The stator terminals connection type is delta. The results of the DC tests carried out on the 18.5 kW induction machine based on different currents and terminals and also connection types are presented in Table 4-2.

**Table 4-2: DC tests results of the 18.5 kW induction machine.**

Connection	Terminals	DC current [A]	Measured DC Voltage [V]
Delta	U1-V1	10	3.133
Delta	U1-W1	10	3.145
Delta	V1-W1	10	3.355
Delta	U1-V1	15	4.701
Delta	U1-W1	15	4.708
Delta	V1-W1	15	5.02
Wye	U1-V1	10	9.85
Wye	U1-W1	10	9.18
Wye	V1-W1	10	9.83
Wye	U1-V1	15	15.01
Wye	U1-W1	15	14
Wye	V1-W1	15	15.08

It is evident in the above table that the measured voltage for V1-W1 terminals in delta connection and also for U1-W1 terminals in star connection are noticeably different than the other measured voltages. This is mainly because of the difference in resistance for one of the terminals or asymmetry in power source which can cause this significant difference for measured voltages.

#### 4.2.1.2 No-load test

The aim of this test is to calculate the no-load reactance based on the measured current and active power [82]. The 18.5 kW induction machine is operating at no load and three-phase nominal voltages are applied to stator terminals while rotor windings are short-circuited. Then, based on the no-load current and voltages, no load impedance is achievable. In addition, the no-load resistance is achievable by measuring the active power and also no load current. The results of the no-load test carried out on the 18.5 kW induction machine for each phase are presented in Table 4-3. It should be noted that this data was measured by a Fluke Norma 4000 Power Analyser.

**Table 4-3: No load test results of the 18.5 kW induction machine.**

Phase	Phase A	Phase B	Phase C
Voltage [V]RMS	230.37	230.1	230
Current [A]	17.57	16.05	16
Active Power [kW]	0.46	0.4	0.3395
Reactive Power [kVAR]	4.08	3.669	3.845
Apparent Power [kVA]	4.076	3.715	3.85
Power Coefficient	0.1138	0.096	0.085

Like the DC tests, in this test, it is also evident that the results for one of the phases are noticeably different than the other two phases. In addition, it can be observed from the above data that the three-phase power source used for the test did not provide the machine with completely symmetrical sinusoidal waves such that phase A has a higher magnitude of the voltage. Furthermore, it is also possible that the phase A might have a lower resistance in comparison to the other phases.

#### 4.2.1.3 Blocked rotor test

The aim of this test is to calculate the blocked rotor reactance based on the measured voltage and active power [82]. The rotor of the 18.5 kW induction machine is blocked such that it cannot rotate. In addition, three-phase sinusoidal voltage is applied to the stator such that it draws the stator nominal current while rotor terminals are short-circuited. Then, based on the blocked rotor current and voltages, blocked rotor impedance is achievable. In addition, the blocked rotor resistance is achievable by measuring the active power and also blocked rotor current. The stator terminals connection type is delta. The results of the no-load test carried out on the 18.5 kW induction machine for each phase are presented in Table 4-4. It should be noted that this data was measured by a Fluke Norma 4000 Power Analyser.

**Table 4-4: Blocked rotor test results of the 18.5 kW induction machine.**

Phase	Phase A	Phase B	Phase C
Voltage [V]	37.285	36.51	36.613
Current [A]	35.01	35.73	35.36
Active Power [KW]	0.55038	0.48632	0.48522
Reactive Power [KVAR]	1.134	0.9664	1.0269
Apparent Power [KVA]	1.2264	1.0563	1.114
Power Coefficient	0.38857	0.4047	0.38521

Like the DC and no load test results, it observable that phase A has a noticeably different current and voltage. This is mainly due to the asymmetry in the power source applied to the stator terminals and also probably because of the different resistance of phase A in comparison to the other phases.

#### 4.2.1.4 Parameters calculation

After performing the DC and no load and block rotor tests, the parameters of the 18.5 kW machine are achievable [82]. For delta connected stator windings in DC tests, stator resistance  $R_S$  is achievable from (4.1) where  $V_{DC}$  and  $I_{DC}$  are DC voltage and current respectively:

$$R_S = \frac{V_{DC}}{I_{DC}} \quad (4.1)$$

And for star connected windings:

$$R_S = \frac{V_{DC}}{2I_{DC}} \quad (4.2)$$

In the no-load test, the no-load impedance  $Z_{NL}$  and resistance  $R_{NL}$  are achievable from (4.3) where the subscript  $NL$  denotes the no load parameters and  $P$  is the active power:

$$\begin{aligned} Z_{NL} &= \frac{V_{NL}}{I_{NL}} \\ R_{NL} &= \frac{P_{NL}}{3I_{NL}^2} \end{aligned} \quad (4.3)$$

In addition, the no-load reactance is obtainable from (4.4):

$$X_{NL} = \sqrt{Z_{NL}^2 - R_{NL}^2} = X_1 + X_M \quad (4.4)$$

Where  $X_1$  is the stator reactance and  $X_M$  is magnetising reactance.

In the blocked rotor test, the blocked rotor impedance  $Z_{BR}$  and resistance  $R_{BR}$  are achievable from (4.5) where the subscript  $BR$  denotes the blocked rotor parameters and  $P$  is the active power:

$$\begin{aligned} Z_{BR} &= \frac{V_{BR}}{I_{BR}} \\ R_{BR} &= \frac{P_{BR}}{3I_{BR}^2} \end{aligned} \quad (4.5)$$

The blocked rotor reactance is obtainable from (4.6):

$$X_{BR} = \sqrt{Z_{BR}^2 - R_{BR}^2} \quad (4.6)$$

Where

$$\begin{aligned} X_{BR} &= X_1 + X_2 \\ R_{BR} &= R_1 + R_2 \end{aligned} \quad (4.7)$$

And also  $X_2$  and  $R_2$  are the rotor reactance and resistance respectively and also  $R_1 = R_S$ .

The relation between the rotor and stator reactance with  $X_{BR}$  depends on the machine class and for a wounded rotor induction machine, it is [82]:

$$X_1 = X_2 = \frac{X_{BR}}{2} \quad (4.8)$$

According to all the equations stated in this chapter so far for the DC and no load and blocked rotor tests, and also the data acquired from the tests, the 18.5 kW machine parameters are obtained and are presented in Table 4-5. It should be noted that due to the difference among the values calculated for each phase or terminal, an average of different values for each parameter is considered in the table.

**Table 4-5: Calculated parameters of 18.5 kW induction machine based on the tests data.**

Parameter	Value
$R_1$ [ $\Omega$ ]	0.483293096
$R_2$ [ $\Omega$ ]	0.759088985
$X_M$ [ $\Omega$ ]	0.04197744679
$X_1$ [ $\Omega$ ]	0.002119423709
$X_2$ [ $\Omega$ ]	0.002119423709

### 4.3 22 kW induction machine

As it is stated at the beginning of this chapter, a 22 kW induction machine is required to act as the prime mover and provide mechanical power for the 18.5 kW wounded rotor induction machine such that the latter acts as a generator.

In Figure 4-3 the nameplate of the 22 kW machine is presented.



**Figure 4-3: 22 kW induction machine nameplate.**

#### 4.4 Powerflex 700 variable frequency AC drive

A variable frequency AC drive is required to control the angular velocity of the 22 kW induction machine which acts as a prime mover for the 18.5 kW induction generator. For this purpose, AC drive controls the angular velocity and also by changing its acceleration rate to a very short time it simulates the perturbations required for the intended tests. Powerflex 700 variable frequency drive is shown in the figure 4-4.



**Figure 4-4: Powerflex 700 Variable frequency AC drive.**

#### 4.5 Torque measurement

Torque measurement is done indirectly in this study, by measuring the force applied to the load cell connected to the 18.5 kW machine. Then, multiplying the force measured in Newtons by the distance from center of the load cell to 18.5 kW machine axis in meters gives the mechanical torque in newton-meters. Therefore, mechanical torque is obtainable from (4.9):

$$T_m = F \times d \quad (4.9)$$

The maximum force created by the 22 kW machine on the load cell with a distance of about 240 mm from the horizontal axis of the machine, can be approximated by first measuring the torque created by such machine in its nominal speed according to its nameplate (1460 rpm with 380 volts excitation in delta connection).

$$T_{max} = \frac{Power [kW]}{Angular Velocity [rpm] \times \frac{\pi}{30}} = \frac{22 kW}{1460 \times \frac{\pi}{30}} = 143.8935102 Nm$$

Then, considering the 240 mm distance from the center of the load cell to the horizontal axis of the machine, the maximum force in Newtons is obtainable:

$$F_N = \frac{143.8935102 \text{ Nm}}{240 \text{ mm} \times 10^{-3}} = 599.5562925 \text{ N}$$

And dividing the result to the gravity constant gives the force in kg:

$$F_{kg} = \frac{599.5562925 \text{ N}}{9.8} = 61.17921352 \text{ kg}$$

Therefore, a load cell capable of measuring at least twice as this number is chosen. The closest load cell to this selection is a 200 kg load cell capable of having the best accuracy in this force range and for this application. A picture of a CNCELL PA6110 200 kg load cell is shown in the figure 4-5.



Figure 4-5: CNCELL PA6110 200 kg load cell.

#### 4.6 Current measurement

In order to measure 6 current signals including 3 stator and 3 rotor currents, 6 current sensors are required in the test setup. Since the current rating for the 18.5 kW induction machine is 35 amperes for the stator and 52 amperes for the rotor windings, sensors capable of measuring at least two times as these numbers are required. For this purpose, LEM Hass 50-S current transducer is considered which is capable of measuring currents up to 150 amperes. A picture of this sensor is shown in figure 4-6.

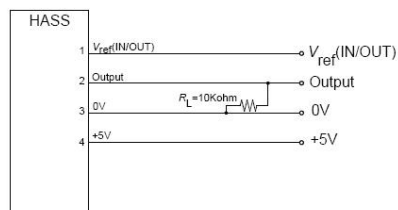


**Figure 4-6: LEM Hass 50-S current sensor.**

The principle of current measurement is based on measuring the voltage over two out of the four terminals of the current sensor where a 10 k $\Omega$  resistance is connected, then multiplying it by a factor ( $\frac{1}{0.625}$ ) according to its datasheet.

The required connection circuit for the sensor as well as its operation principle diagram is shown in figure 4-7.

### Required connection circuit



### Operation principle

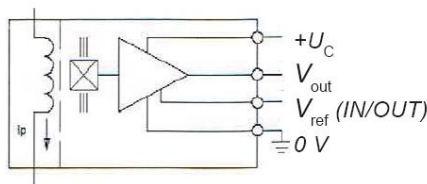


**Figure 4-7: LEM Hass 50-S current sensor connection circuit and operation diagram.**

## 4.7 Voltage measurement

According to the scope of this research and the cases studies considered for that, 3 stator voltage signals are required to be measured, while no voltage is applied to rotor windings and they are short-circuited. Because of the 18.5 kW machines ratings, a voltage transducer capable of



measuring voltages in the preferred range is chosen. LEM voltage transducer LV 25-P is the desired sensor for this application which can measure voltages up to 500 volts. Picture of this sensor is shown in figure 4-8.



**Figure 4-8: LEM LV 25-P voltage transducer.**

The principle of voltage measurement with this sensor is that a current proportional to the measured voltage is passed through an external resistor  $R_1$  which is chosen by the user in the beginning and installed in series with the primary circuit of the sensor [83]. In addition, a measuring resistance or  $R_M$  must be chosen on the secondary side and connected to the terminal with the zero or reference voltage of the power source. These resistances must be chosen that a current close to the nominal current flows through the primary side. Choosing the correct resistances for  $R_1$  and  $R_M$  are very important since they can significantly affect the accuracy of the measurement, also they must be chosen in a way that do not overheat or burn due to their low wattage. Considering these facts, a  $330 \Omega$  resistance as  $R_M$  and a  $220 k\Omega$  as  $R_1$  are chosen. The connection diagram needed for this voltage transducer is shown in figure 4-9

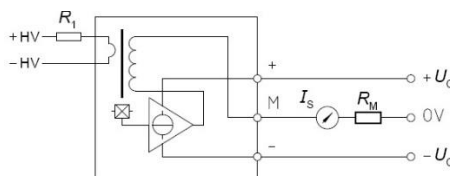


**Figure 4-9: LEM LV 25-P voltage transducer connection diagram.**

#### 4.8 Angular position and angular velocity measurement

One of the other signals required to be measured for parameter estimation in this study is the angular velocity, as well as the angular position which can possibly affect the estimation results. In order to do so, a position sensor is required. Among all the available sensors, optical encoders have advantages over magnetic encoders mainly due to their higher reliability. In addition, among all the optical rotary encoders, the incremental encoders have advantages over the absolute encoders like more simplicity, especially in connection terminals and lower cost. But unlike absolute encoders, they cannot show the exact position of the rotor. For this study, a Baumer GI342 hollow shaft incremental encoder with a resolution of 100 pulses per revolution is chosen (3.6 degrees of accuracy). The picture of this encoder is shown in the figure 4-10.



**Figure 4-10: Baumer GI342 incremental encoder.**

Output signals and also the terminal assignment of this sensor are shown in figure 4-11 and 4-12 respectively.

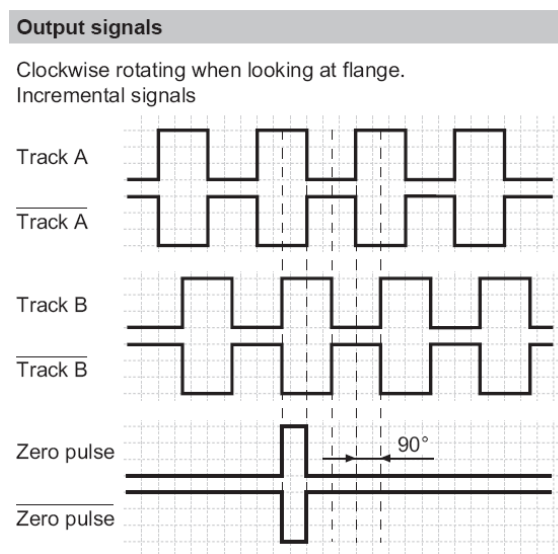


**Figure 4-11: Baumer GI342 incremental encoder output signals.**

Terminal assignment	
<b>Without commutating tracks</b>	
Core colour	Assignment
grey	Track B
pink	Track B inv.
red	Track N (zero pulse)
black	Track N inv. (zero pulse inv.)
brown	Track A
green	Track A inv.
white/green	GND
brown/green	UB

**Figure 4-12: Baumer GI342 incremental encoder terminal assignment.**

## 4.9 Data acquisition hardware and software

In this section, the data acquisition hardware and software is briefly explained. In addition, a short review on how they are used together in order to acquire signals is presented [84].

### 4.9.1 Data acquisition hardware

This subsection introduces the data acquisition chassis and cards used in acquiring the desired signals.

#### 4.9.1.1 NI CompactDAQ 9178 8-Slot USB Chassis

NI CompactDAQ 8-Slot USB is chosen as the chassis to host different cards for the purpose of data acquisition. A picture of this chassis is shown in the figure 4-13.



**Figure 4-13: NI CompactDAQ 9178 USB Chassis.**

This chassis has the following capabilities for measurement and data acquisition [84]:

- Four general-purpose 32-bit counter/timers built into chassis (access through digital module).
- Run up to 7 hardware-timed analog I/O, digital I/O, or counter/timer operations simultaneously.
- Stream continuous waveform measurements with patented NI Signal Streaming technology.
- Built-in BNC connections for external clocks and triggers (up to 1 MHz)
- Measure in minutes with NI-DAQmx software and automatic code generation using the DAQ Assistant.

#### 4.9.1.2 NI 9215 measurement card

This card is an analog card used to measure the voltage and current signals. It measures in differential mode and for the non-referred signals it is necessary that the negative terminal must be connected to the common point (as a ground) through a suitable resistance (1 M $\Omega$  according to its datasheet) in order to match the input impedance required for this card. A picture of this card is shown in the figure 4-14.



**Figure 4-14: NI 9215 measurement card.**

In addition, this card has the following capabilities for measurement and data acquisition [84]:

- 4 differential channels, 100 kS/s per channel sample rate.
- $\pm 10$  V measurement range, 16-bit resolution.

- 250 Vrms channel-earth, CAT II (screw terminal), or 60 VDC channel-earth, CAT I (BNC) isolation.
- 10-position screw-terminal or BNC connectors available.
- -40 °C to 70 °C operating, 5 g vibration, 50 g shock.

#### 4.9.1.3 NI 9401 measurement card

This card is a digital card used to measure angular position and subsequently angular velocity based on the data it reads from the incremental encoder. A picture of this card is shown in the figure 4-15.



**Figure 4-15: NI 9401 measurement card.**

In addition, this card has the following capabilities for measurement and data acquisition [84]:

- 8-channel, 100 ns high-speed digital I/O.
- 5 V/TTL, sinking/sourcing digital I/O.
- Compatible with NI CompactDAQ counters.
- 60 VDC, CAT I isolation.
- Industry-standard 25-pin D-SUB connector.
- 40 °C to 70 °C operating, 5 g vibration, 50 g shock.

#### 4.9.1.4 NI 9237 measurement card

This card has a bridge analog input and is used to measure force from the load cell and subsequently convert it to torque by considering a factor (the distance). It has a limited selection of sampling frequencies (50/31, 50/30, 50/29, ... , 50/1 kS/s). A picture of this card is shown in the figure 4-16.



**Figure 4-16: NI 9237 measurement card.**

In addition, this card has the following capabilities for measurement and data acquisition [84]:

- 4 channels, 50 kS/s per channel simultaneous AI.
- $\pm 25$  mV/V input range, 24-bit resolution.
- Programmable half- and full-bridge completion with up to 10 V internal excitation.
- 60 VDC, Category I bank isolation.
- 40 °C to 70 °C operating range, 5 g vibration, 50 g shock.

#### 4.9.2 Data acquisition software

Labview software is employed to be used for data acquisition in order to read the data from the hardware explained in the previous section. In this section, a short review of how each of these measurement tasks is structured in Labview is presented. In all of the following subsections, instead of using the common DAQ Assistant VI for measurements as a configuration based method to interact with the hardware, an alternative way is used. DAQ Assistant VI uses NI-DAQmx functions under the hood. It might seem easier to use DAQ Assistant VI but in fact, it can become problematic while using different kinds of signals and measurement methods, for instance in reading analog and digital signals with different measurement cards and methods simultaneously. Using NI-DAQmx functions directly gives the capabilities of accessing to the low-level programming timing and all the other settings which enables to synchronize different types of signals together [84].

#### 4.9.2.1 Voltage and current measurement task

The left side of the following figure shows how the voltage and current measurements are structured in Labview. First, a NI-DAQmx *create virtual channel* function defines the type of task as voltage type for both current and voltage measurements due to the same principle used in measuring both of them. Then, the channel which the data must be read from is also defined. A NI-DAQmx timing function defines the timing settings of the measurement, including the sampling rate (number of samples per second) and the total number of samples to be read in each loop. After that, a function to define the buffer size this task manually is defined to prevent any possible data overflow. Then the execution of the task starts and then the task continues until it reaches the while loop where the read function starts reading the data continuously for each loop according to the settings defined for that and the task will stop when it reaches an error or when it acquires the desired data. The generic block diagram of the voltage and current measurements is shown in figure 4.17.

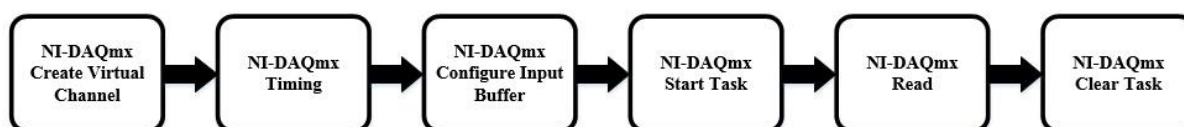


**Figure 4-17: Current and voltage measurement task structured by NI-DAQmx functions.**

#### 4.9.2.2 Load cell measurement task

Like the previous subsection, here the load cell measurement task starts with NI-DAQmx create virtual channel function where it defines the virtual channel and its related port, as well as the measurement task which is force measurement. Then the timing setting is defined by the sample clock function and later on the shunt calibration and offset null is done. Then the execution starts and the task wire goes inside the while loop where reading the data starts in the loop. Then the measured force will be multiplied to the distance factor 240 mm or 0.24 m and then it is shown on the graph as mechanical torque. Figure 4-18 shows the generic block diagram of the load cell measurement task structured by the NI-DAQmx functions.

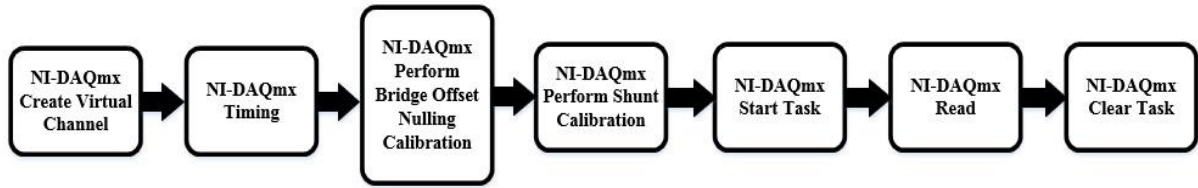


**Figure 4-18: load cell measurement task structured by NI-DAQmx functions.**

#### 4.9.2.3 Angular position and angular velocity measurement task

Angular position and angular velocity measurement task is shown the figure 4-19. This task also starts with NI-DAQmx create virtual channel function where it defines the virtual channel and its related port, as well as the measurement task which is angular encoder task. Then the execution starts and the task wire goes to a loop where the data acquisition starts. The main difference between this task with the other tasks like voltage and current measurements is the acquisition mode. Unlike the other tasks, the acquisition mode in this task is discrete. Therefore, only one sample is read in every loop, and the loop execution time depends on the block in the corner the while loop called “wait until the next milliseconds”.

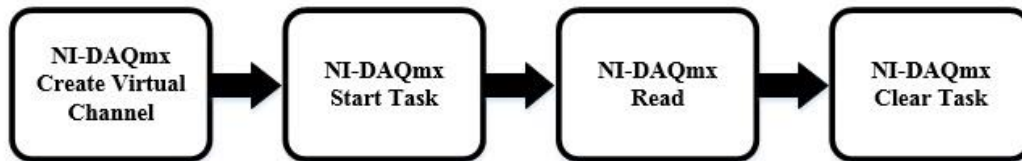


**Figure 4-19: Angular position and angular velocity task structured by NI-DAQmx functions.**

#### 4.9.2.4 Front panel structure

Figures 4-20 and 4-21 each show a part of the front panel of the codes written to acquire and read the data. In 4-20, the settings used in the codes are shown and in 4-28 the virtual screens for showing the signals are presented.





Figure 4-20: Front panel of the codes written for the measurements including the settings in Labview.

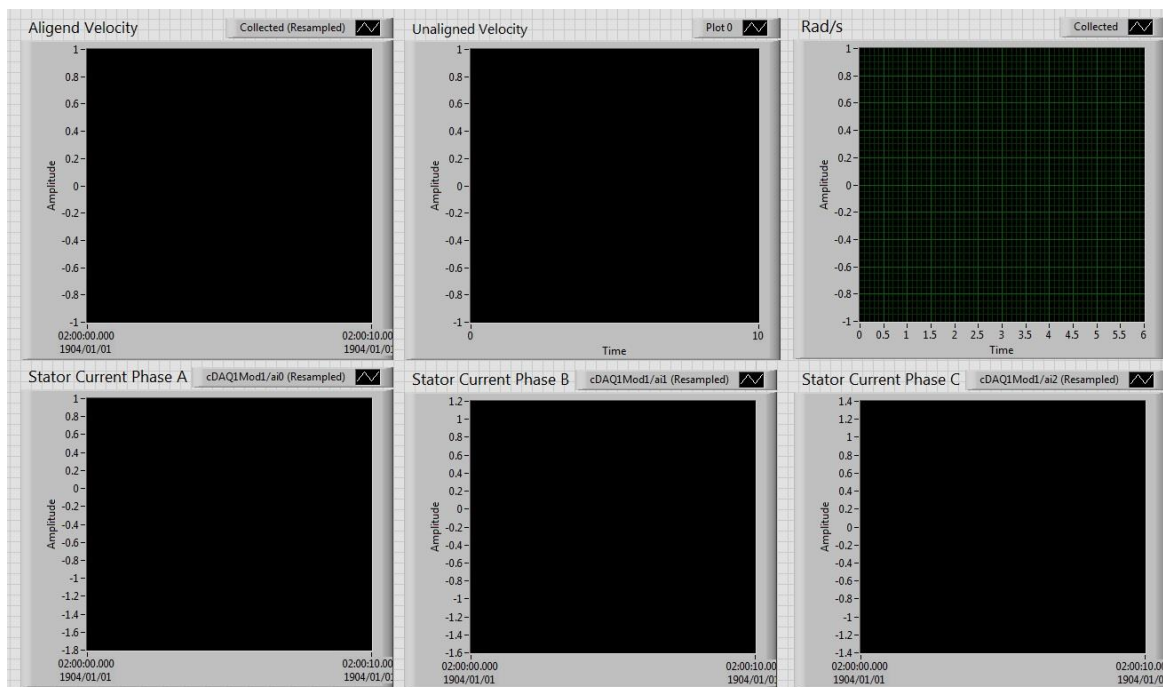
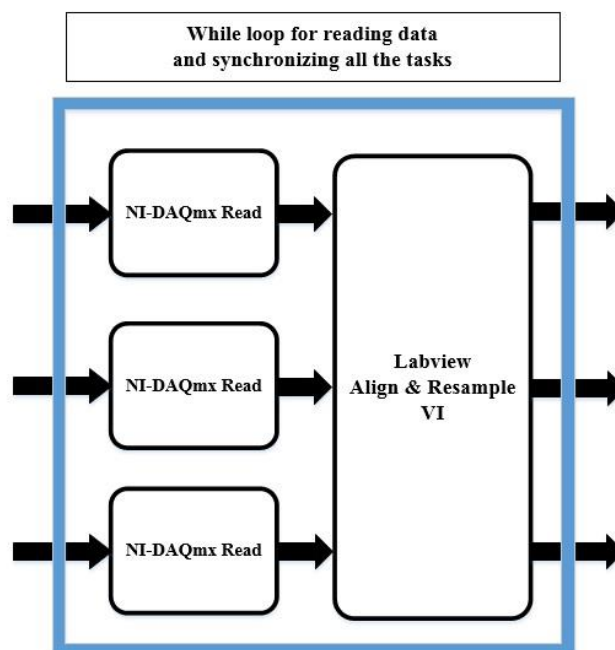


Figure 4-21: Front panel of the codes written for the measurements including some of the virtual screens.

#### 4.9.2.5 Task synchronization

Due to the inherent differences in signal types and their acquiring methods and also hardware and measurements cards, the acquired signals do not have the same starting time and also the same sampling rate. For the purpose of parameter estimation and any mathematical operations with the signals, they must have the same time interval and also the data points. In order to synchronize these tasks, a VI called “Align and resample” is employed to synchronize these signals and make the signals with the same sampling rate and same start and finishing point. This is shown in the figure 4-22 where all the signals are being read in the same loop. Then they are aligned and resampled with each other.



**Figure 4-22: Generic block diagram of the Align and resample VI for synchronizing different signals.**

In addition, the data acquisition generic block diagram for the whole system including all the tasks and synchronized signals are shown in the figure 4-23. Each of the tasks is explained in the previous sections.

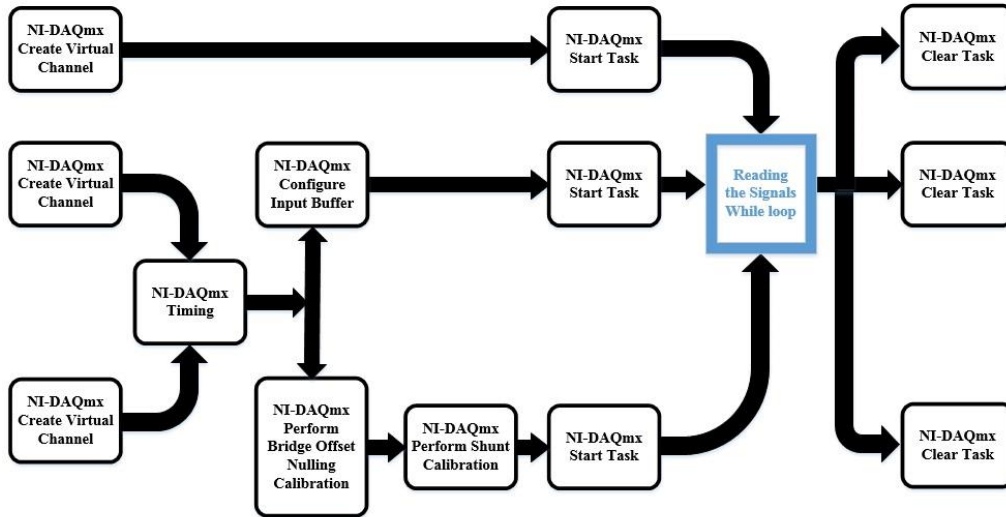


Figure 4-23: Complete Labview generic block diagram with all the tasks used in this study.

## 5 PARAMETER ESTIMATION RESULTS

### 5.1 Introduction

In this chapter, estimation results based on simulated signals and also the signals measured from the machine are presented. Electrical parameters of the machine are estimated in different case studies and then compared together to investigate the accuracy and capability of the model.

### 5.2 Parameter estimation procedure

In order to perform parameter estimation, the MATLAB has a graphical user interface (GUI) designed specifically for this purpose known as the control and estimation GUI. The alternative method to this is making use of MATLAB command lines. In this manner, it is very simple to apply the necessary changes to the signals during estimation to see the possible variations in estimation results for each case study or test [6].

The parameter estimation procedure in MATLAB consists of the following segments that employ object-oriented programming methods [6]:

- *Transient Data*
- *State Data*
- *Transient experiment*
- *Parameter*
- *State*
- *Estimation*
- *Simulation options*
- *optimization options*

The above-mentioned segments are explained briefly according to [6]:

The *Model* block represents the Simulink model required for the purpose of parameter estimation where all the input and output data are fed into its input and output ports. The *Transient Data* is defined for each port and has the following properties [6]:

- Port type
- Port number
- Port data
- Time interval
- Weight factor

For every Simulink block including objects, one *State Data* object is formed. In addition, for the experiment, the states' initial values are assigned to the state data objects. The *transient experimental* objects consist of two main components known as the *input-output data* and *initial states*. These objects are filled with the *transient data* objects and the *State Data* objects in tandem. Then, for the *estimation* object, the *transient experiment* is allocated to the *experiment data* property [6].

The *parameter objects* are further configured. Every parameter of the model requires a *Parameter* object. The main components of this object are as follows [6]:

- *Dimension*
- *Value*
- *Estimation flag*
- *Initial guess*
- *Boundaries*
- *Typical values*

For a one dimensional parameter, the property related to the *estimation flag* is a Boolean variable that becomes true for the parameter which is going to be estimated and becomes false for the parameter that is not going to be estimated [6]. The property related to the *value* is filled with an initial guess for the parameter and varies while the parameter is being estimated. The *typical value* property can be used for the purpose of scaling the parameter if it is known, but if it is unknown, this property will be filled with the initial value of the parameter. The other *Parameter* objects stated above do not need a further explanation [6].

If the parameter is in the form of a vector or matrix, all the properties of its objects are in the same form with the same dimensions. In addition, for every element in the property, there is a corresponding element in the parameter in each vector or matrix. Furthermore, the *Estimation* object's *Parameter* property is created from the combination of all the *Parameter* objects.

Similarly, the *State* object is configured in the same way as the *Parameter* object with the same properties. Then, the *Estimation* object's *States* property is created from the combination of all the *State* objects [6].

In the optimization section, the algorithms employ numerical solvers for the estimation processes. In order to configure the optimization algorithms and numerical solvers, a *simulation options* object needs to be defined and configured. The *simulation options* object has the following properties [6]:

- *Solver*
- Minimum step size
- Maximum step size
- Start time
- Stop time

The *Estimation* object's *simulation options property* is allocated by the above-mentioned *simulation options* object. Moreover, the *Estimation* object's *optimisation options* property requires an *Optimisation Options* object which has the following properties [6]:

- *Method*: This property represents the method employed for the optimisation process.
- *Algorithm*: This refers to the algorithm employed for the optimisation process.
- *DiffMin* and *DiffMax*: They represent the properties regarding the minimum and maximum variations respectively.
- *TolX*: This property refers to the tolerance of the Parameter or the minimum step size.
- *TolFun*: This property represents the tolerance of the objective function.
- *MaxIter*: This property represents the maximum number of iterations.
- *MaxFunEvals*: This property refers to the maximum number of times the objective function can be evaluated.
- *Display*: This property is an option which allows showing various information during estimation.

More information on this is explained in [6].

### 5.3 Estimation results based on simulated signals

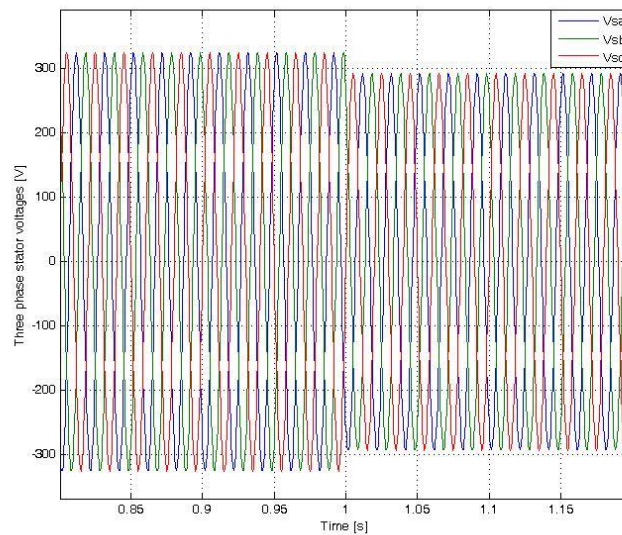
In this section, estimation results based on simulated signals on doubly fed induction generator ABC and DQ model will be given. Two different types of perturbation conditions are considered. The first one is angular velocity perturbation and the second one is the stator voltage perturbation. Assumptions considered for both case studies, are the rotor windings are short-circuited such that the machine was operated as an induction generator, the stator terminals were excited with symmetrical 50 Hz three-phase voltages with RMS phase voltage of 230 V. The cost function is obtained from the torque and the current output signals measured from the machine. In addition, the MATLAB estimation settings for both types of perturbations are shown in Table 5-1.

**Table 5-1: Parameter estimation settings.**

Solver	MaxStep	RelTol	DifMin	DifMax	TolX	TolF
Ode23s	$10^{-4}$	$10^{-5}$	$10^{-8}$	$10^{-1}$	$10^{-5}$	$10^{-5}$

### 5.3.1 Stator voltage perturbation

In this case study, the angular velocity is maintained constant at 160.221 rad/s, while stator voltages decreased fast by 10 percent at  $t=1$ s as it is shown in Fig 5-1.

**Figure 5-1: Three-phase stator voltages perturbation.**

In addition, the three-phase stator currents, three-phase rotor currents and mechanical torque are shown in figures 5-2, 5-3 and 5-4 respectively.

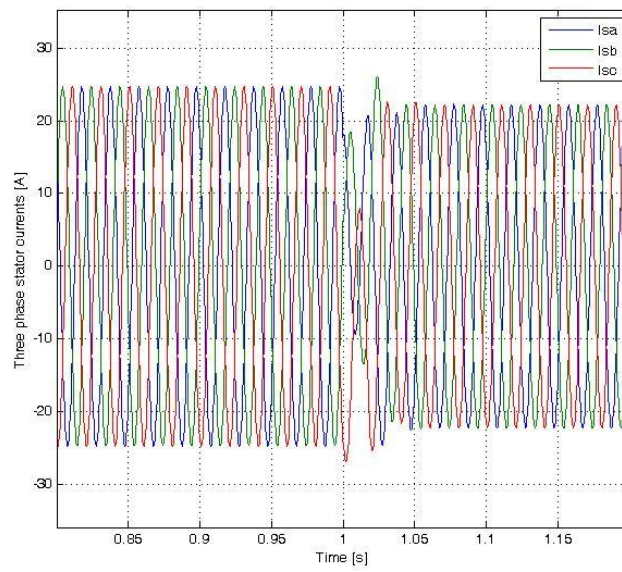


**Figure 5-2: Three-phase stator currents**

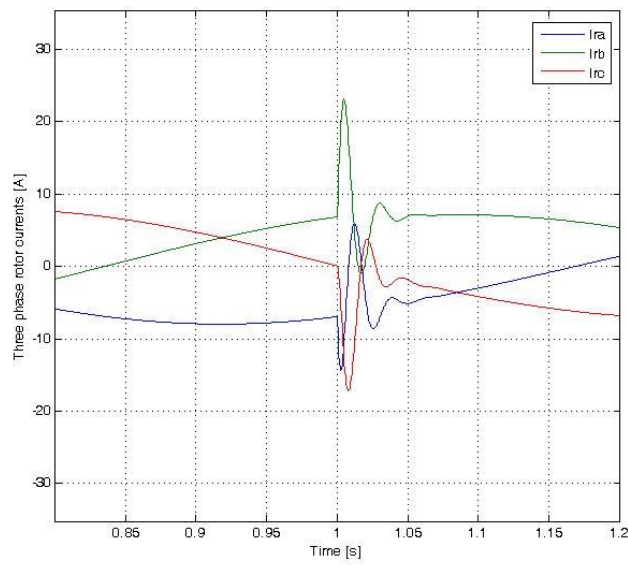


**Figure 5-3: Three-phase rotor currents.**



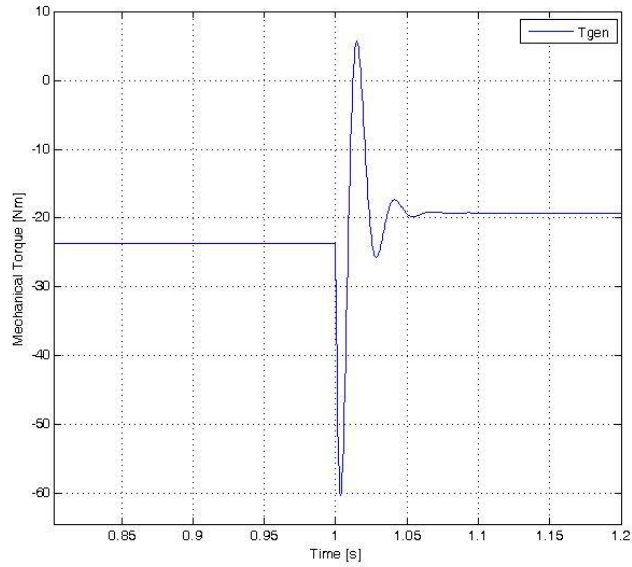


**Figure 5-4: Mechanical torque.**

### 5.3.1.1 ABC model

The estimation results for the stator voltage perturbation based on the simulated signals regarding the ABC model are presented in table 5-2.

**Table 5-2: The ABC model Parameter estimation results for the stator voltage perturbation based on the simulated signals.**

Parameter	Initial Guess	Actual	Estimated	Error
$L_r$ [H]	$10^{-4}$	0.0021194	0.002131	-0.54%
$L_s$ [H]	$10^{-4}$	0.0021194	0.002109	0.49%
$L_m$ [H]	$10^{-4}$	0.0419774	0.042	0.05%
$R_r$ [ $\Omega$ ]	$10^{-4}$	0.7590889	0.75828	0.106%
$R_s$ [ $\Omega$ ]	$10^{-4}$	0.4832930	0.48308	0.102%

### 5.3.1.2 DQ model

The estimation results for the stator voltage perturbation based on the simulated signals for the ABC model is presented in table 5-3.

**Table 5-3: The DQ model Parameter estimation results for the stator voltage perturbation based on the simulated signals.**

Parameter	Initial Guess	Actual	Estimated	Error
$L_r$ [H]	$10^{-4}$	0.0021194	0.0021157	- 0.42%
$L_s$ [H]	$10^{-4}$	0.0021194	0.0021119	0.41%
$L_m$ [H]	$10^{-4}$	0.0419774	0.0419931	- 0.03%
$R_r$ [ $\Omega$ ]	$10^{-4}$	0.7590889	0.758530	0.89%
$R_s$ [ $\Omega$ ]	$10^{-4}$	0.4832930	0.48314	0.76%

### 5.3.2 Angular velocity perturbation

In [7], a step signal added to the angular velocity input signal is considered. It is practically impossible for angular velocity to change instantaneously like a step signal; therefore, in this study angular velocity will increase with a relatively high slope, like a ramp signal defined for a specific time interval instead of changing instantaneously as it is shown in fig 5-5, while stator voltages will still be an RMS value of 230 V. The three-phase stator voltages, three phase stator currents, three-phase rotor currents and mechanical torque are presented in figures 5-6, 5-7, 5-8 and 5-9 respectively.

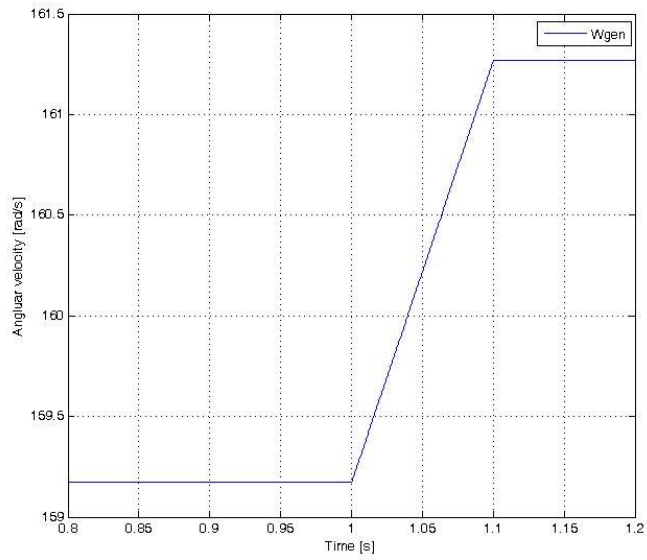


**Figure 5-5: Angular velocity perturbation.**

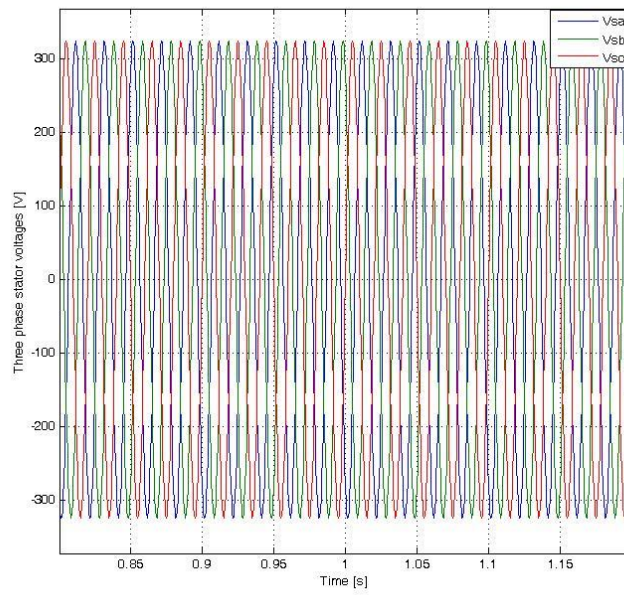


**Figure 5-6: Three-phase stator voltages.**

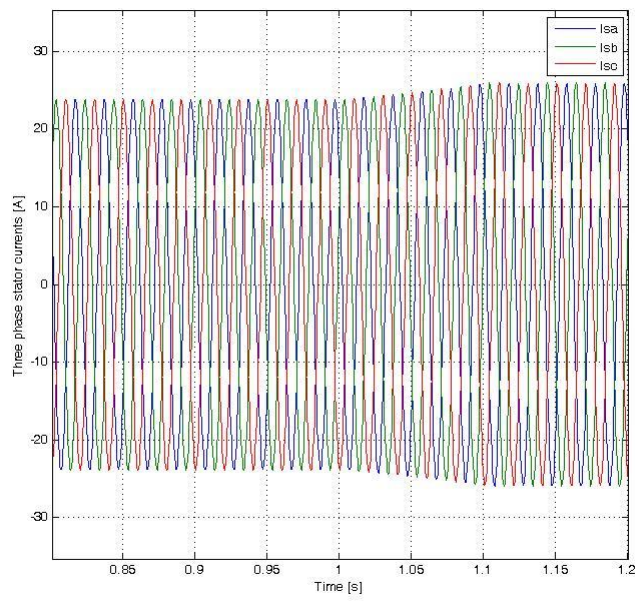


**Figure 5-7: Three-phase stator currents.**

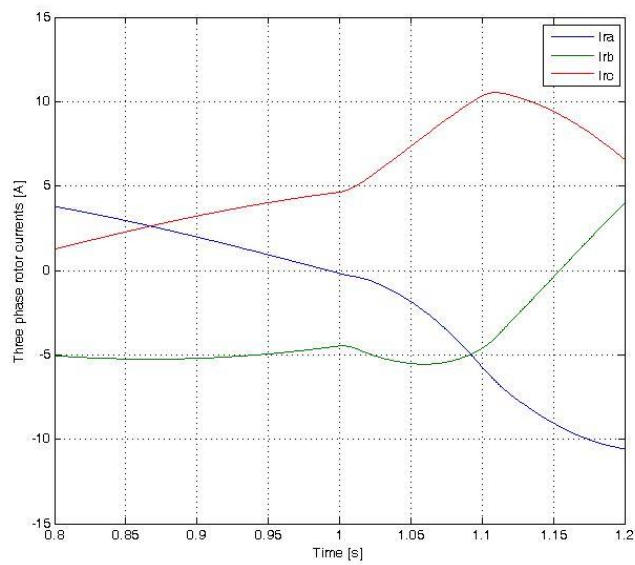


**Figure 5-8: Three-phase rotor currents.**

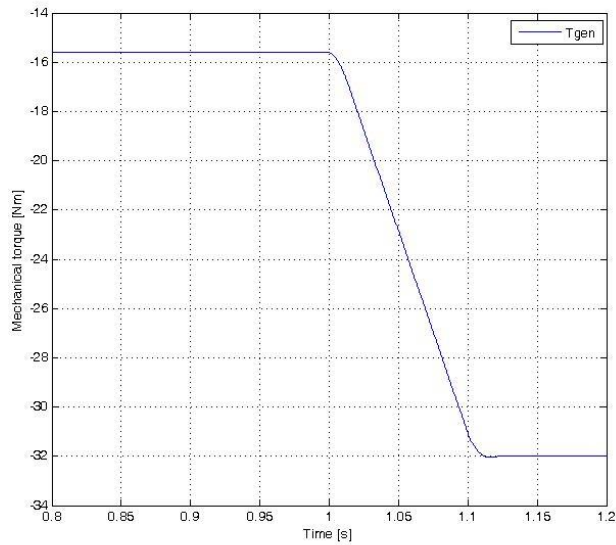


**Figure 5-9: Mechanical torque.**

### 5.3.2.1 ABC model

The estimation results for the angular velocity perturbation based on the simulated signals regarding the ABC model are presented in table 5-4.

**Table 5-4: The ABC model Parameter estimation results for the angular velocity perturbation based on the simulated signals.**

Parameter	Initial Guess	Actual	Estimated	Error
$L_r$ [H]	$10^{-4}$	0.0021194	0.0021176	0.084%
$L_s$ [H]	$10^{-4}$	0.0021194	0.002122	-0.122%
$L_m$ [H]	$10^{-4}$	0.0419774	0.041962	-0.036%
$R_r$ [ $\Omega$ ]	$10^{-4}$	0.7590889	0.75953	-0.058%
$R_s$ [ $\Omega$ ]	$10^{-4}$	0.4832930	0.48339	-0.02%

### 5.3.2.2 DQ model

The estimation results regarding the angular velocity perturbation based on the simulated signals for the DQ model are presented in table 5-5.

**Table 5-5: The DQ model Parameter estimation results for the angular velocity perturbation based on the simulated signals.**

Parameter	Initial Guess	Actual	Estimated	Error
$L_r$ [H]	$10^{-4}$	0.0021194	0.0021210	-0.12%
$L_s$ [H]	$10^{-4}$	0.0021194	0.0021167	0.185%
$L_m$ [H]	$10^{-4}$	0.0419774	0.042	0.02%
$R_r$ [ $\Omega$ ]	$10^{-4}$	0.7590889	0.7589	0.03%
$R_s$ [ $\Omega$ ]	$10^{-4}$	0.4832930	0.4831117	0.3%

### 5.3.3 Conclusion

The results obtained from the Tables 5-2 to 5-5, shows that the estimation results have a great accuracy with errors less 1%. It is mainly because of the estimation settings which was applied, as it was demonstrated in Table 5-1.

## 5.4 Estimation results based on measured signals

In this section, the test setup shown in figure 4-1 in chapter 4 is considered to perform different tests with different perturbation signals to excite system eigenvalues for purpose of parameter estimation. The 18.5 kW slip ring induction machine should operate as an induction generator. Therefore another machine is required to drive its shaft and provide mechanical energy for it. In addition, a 22 kW induction motor will act as the prime mover in this setup. Moreover, a variable speed AC drive is required, as well as three-phase excitation voltage for an induction generator and also torque and speed sensor. The estimation settings for both types of perturbations are presented in Table 5-6.

**Table 5-6: Parameter estimation settings.**

Solver	MaxStep	RelTol	DifMin	DifMax	TolX	TolF
Ode23s	$10^{-4}$	$10^{-5}$	$10^{-8}$	$10^{-1}$	$10^{-5}$	$10^{-5}$

Similar to the previous section, two types of perturbation conditions with the same assumptions and estimation settings are considered. The first one investigates the estimation results based on the measured signals for the angular velocity perturbation on ABC and DQ models. In addition, the second one investigates the estimation results based on measured signals for the stator voltages perturbation.

#### 5.4.1 Stator voltage perturbation

The stator voltages should directly be connected to the power grid. Therefore, in this practical case study, the main aim is to simulate a perturbation on the grid side, while angular velocity will remain constant. This will be feasible by maintaining the angular velocity on a certain speed with the variable frequency drive while changing the stator voltage for a specific time interval. A zoom in a portion of the three-phase stator voltage signals as inputs, as well as further zoom in the signal showing the perturbation point, are shown in the figures 5-10 and 5-11 respectively. Furthermore, a zoomed in part of the three-phase stator current signals and the rotor current signals in addition to mechanical torque signals as outputs are shown in Fig. 5-12, 5-13 and 5-14 respectively. It should be noted that the rotor current signals, as well as the torque signal, are not very smooth signals and include noises. Therefore, the original signals in addition to the smoothed signals are shown in the above-mentioned figures.

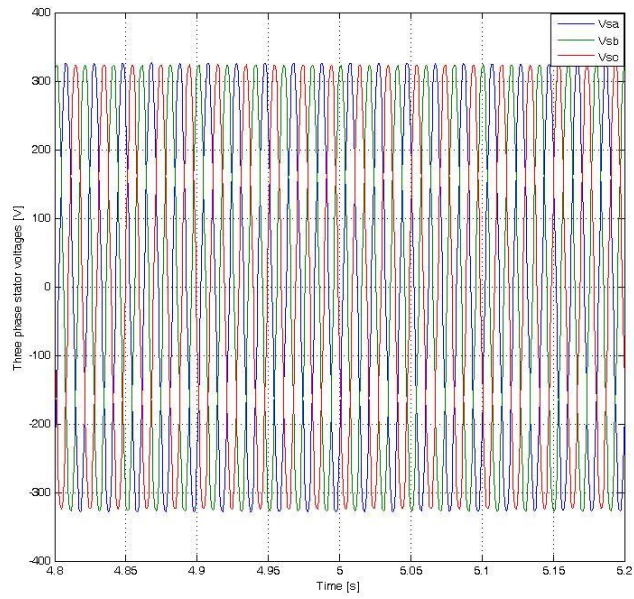


**Figure 5-10: Three-phase stator voltages.**

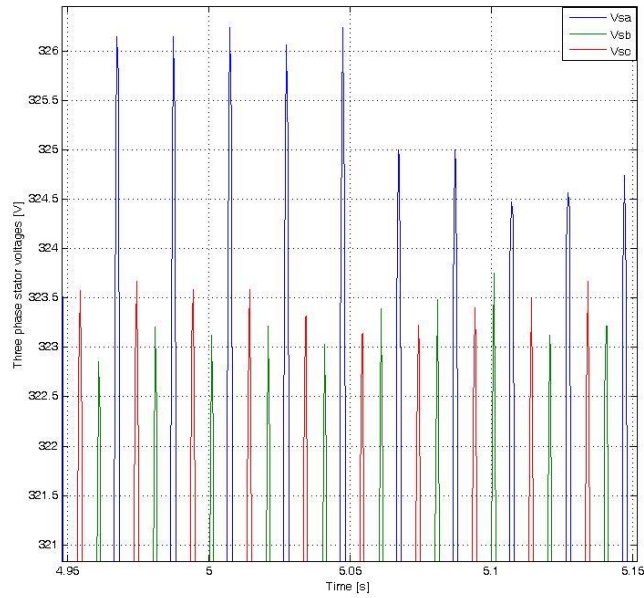


**Figure 5-11: Three-phase stator voltages showing the perturbation point.**



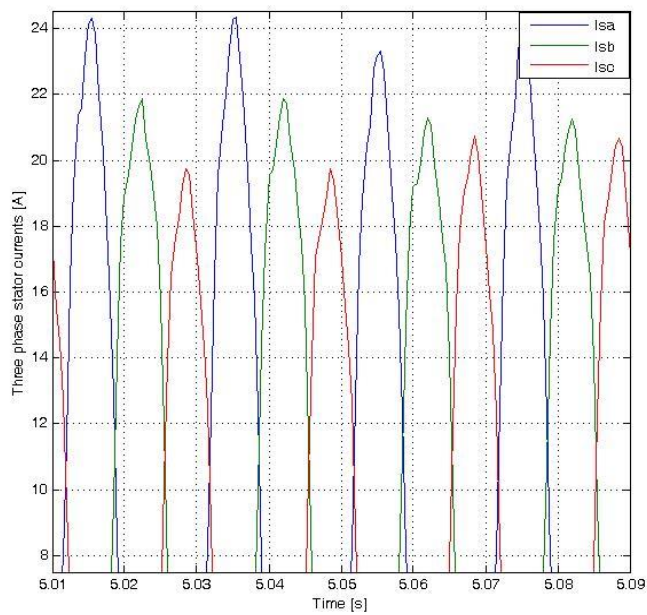


**Figure 5-12: Three-phase stator currents.**

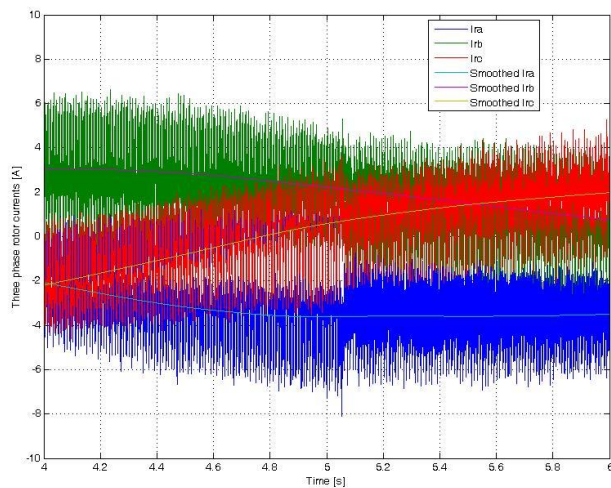


**Figure 5-13: Three-phase rotor currents.**

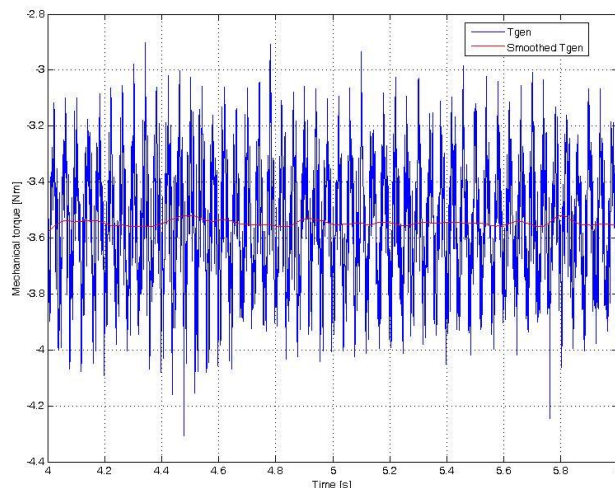


**Figure 5-14: Mechanical torque.**

#### 5.4.1.1 ABC model

The estimation results for the stator voltage perturbation based on the measured signals regarding the ABC model are presented in table 5-7.

**Table 5-7: The ABC model Parameter estimation results for the stator voltage perturbation based on the measured signals.**

Parameter	Initial Guess	Actual	Estimated	Error
$L_r$ [H]	$10^{-4}$	0.0021194	0.005198676	-145.29%
$L_s$ [H]	$10^{-4}$	0.0021194	0.00504502	-138.04%
$L_m$ [H]	$10^{-4}$	0.0419774	0.107638449	-156.42%
$R_r$ [ $\Omega$ ]	$10^{-4}$	0.7590889	1.682216911	-121.61%
$R_s$ [ $\Omega$ ]	$10^{-4}$	0.4832930	1.045556076	-116.34%

### 5.4.1.2 DQ model

The estimation results regarding the angular velocity perturbation based on the measured signals for the DQ model are presented in table 5-8.

**Table 5-8: The DQ model Parameter estimation results for the stator voltage perturbation based on the measured signals.**

Parameter	Initial Guess	Actual	Estimated	Error
$L_r$ [H]	$10^{-4}$	0.0021194	0.004981226	-135.03%
$L_s$ [H]	$10^{-4}$	0.0021194	0.00480468	-126.7%
$L_m$ [H]	$10^{-4}$	0.0419774	0.100032144	-138.3%
$R_r$ [ $\Omega$ ]	$10^{-4}$	0.7590889	1.629156597	-114.62%
$R_s$ [ $\Omega$ ]	$10^{-4}$	0.4832930	0.951265612	-96.83%

### 5.4.2 Angular velocity perturbation

In this practical case study, the perturbation will take place on the input wind. In other words, a wind speed perturbation will be simulated by changing the angular velocity of the 22 kW induction motor via the variable frequency drive for a specific time interval, while the stator voltages of the 18.5 kW induction generator are constant at its rated value. This task is done indirectly, by changing the torque via the variable frequency drive and consequently the angular velocity changes as a result of perturbing the machine torque. The angular velocity and a zoomed in part of the three-phase stator voltage signals as inputs are shown in figure 5-15 and 5-16 respectively. Moreover, a zoomed in part of the three-phase stator currents signals and the rotor current signals in addition to mechanical torque signals as outputs are shown in figures 5-17, 5-18 and 5-19 respectively. It should be noted that the rotor current signals, as well as the torque signal, are not very smooth signals and include noises. Therefore, the original signals in addition to the smoothed signals are shown in the above-mentioned figures.

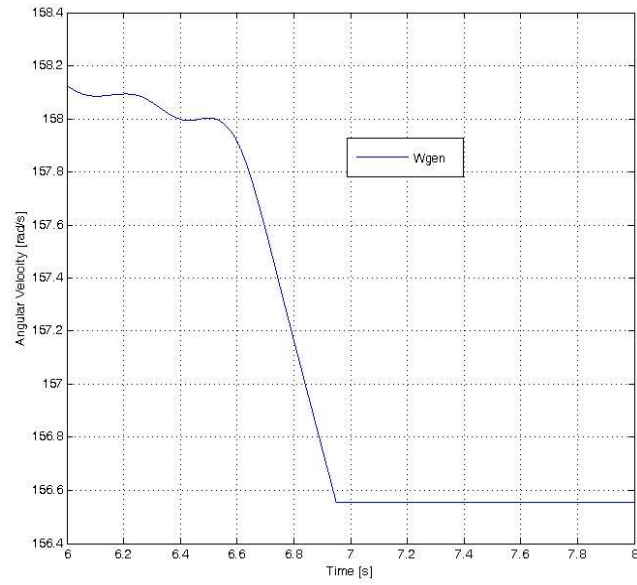


**Figure 5-15: Angular velocity perturbation.**

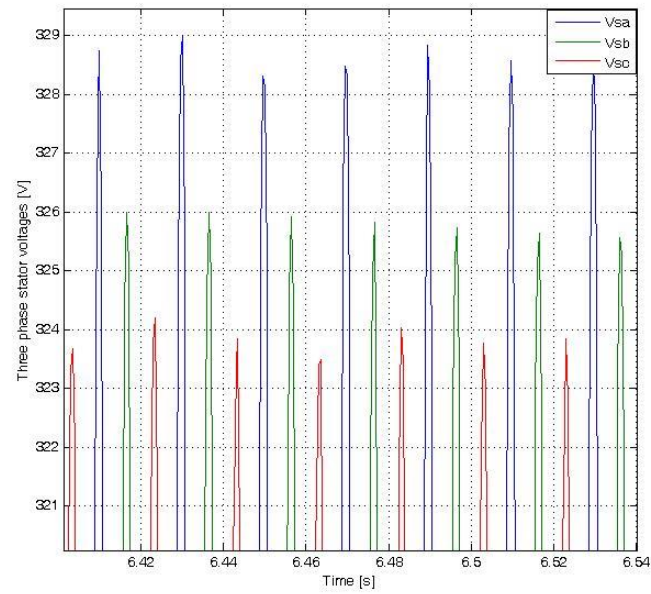


**Figure 5-16: Three-phase stator voltage perturbation.**

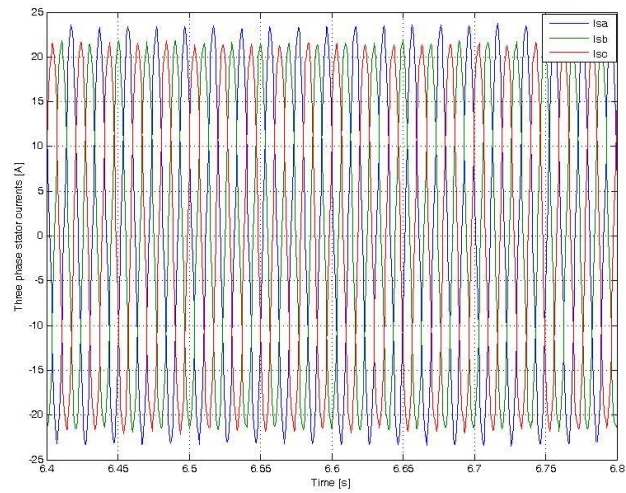


**Figure 5-17: Three-phase stator currents.**

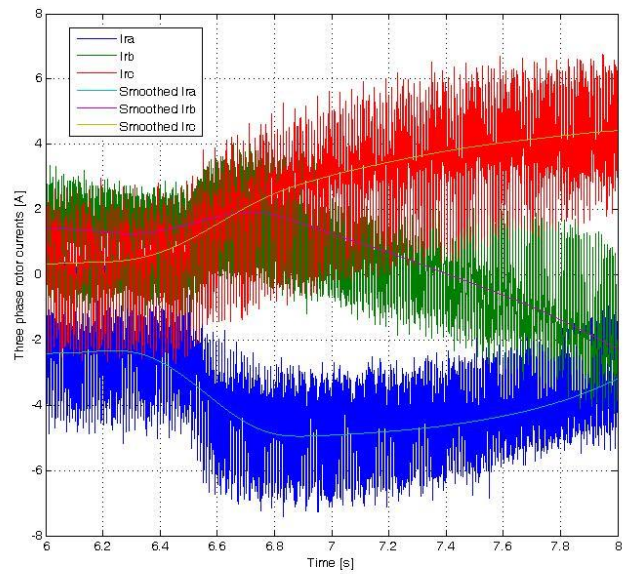


**Figure 5-18: Three-phase rotor currents.**

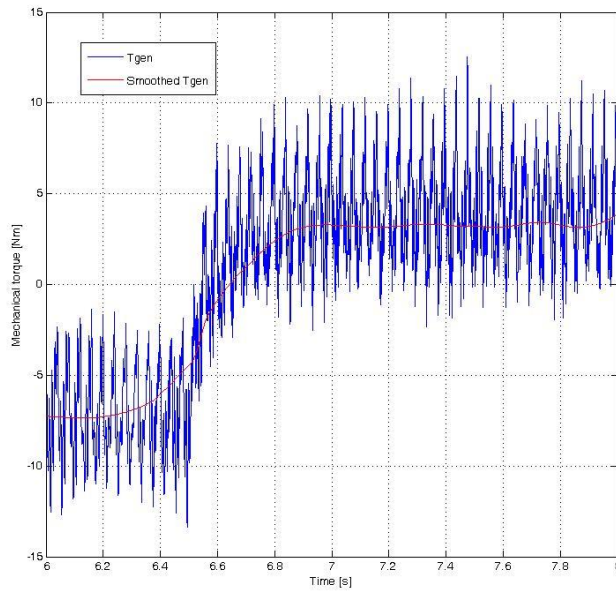


**Figure 5-19: Mechanical torque.**

#### 5.4.2.1 ABC model

The estimation results for the angular velocity perturbation based on the measured signals regarding the ABC model are presented in table 5-9.

**Table 5-9: The ABC model Parameter estimation results for the angular velocity perturbation based on the measured signals.**

Parameter	Initial Guess	Actual	Estimated	Error
$L_r$ [H]	$10^{-4}$	0.0021194	0.005280273	-149.14%
$L_s$ [H]	$10^{-4}$	0.0021194	0.005038026	-137.71%
$L_m$ [H]	$10^{-4}$	0.0419774	0.102441647	-144.04%
$R_r$ [ $\Omega$ ]	$10^{-4}$	0.7590889	1.617117447	-113.034%
$R_s$ [ $\Omega$ ]	$10^{-4}$	0.4832930	1.083368921	-124.164%

### 5.4.2.2 DQ model

The estimation results regarding the angular velocity perturbation based on the measured signals for the DQ model are presented in table 5-10.

**Table 5-10: The DQ model Parameter estimation results for the angular velocity perturbation based on the measured signals.**

Parameter	Initial Guess	Actual	Estimated	Error
$L_r$ [H]	$10^{-4}$	0.0021194	0.005111357	-141.17%
$L_s$ [H]	$10^{-4}$	0.0021194	0.004950918	-133.6%
$L_m$ [H]	$10^{-4}$	0.0419774	0.100493896	-139.4%
$R_r$ [ $\Omega$ ]	$10^{-4}$	0.7590889	1.557270878	-105.15%
$R_s$ [ $\Omega$ ]	$10^{-4}$	0.4832930	1.061939709	-119.73%

### 5.4.3 Conclusion

The estimations results obtained from the measured signals, obviously shows that the accuracy is very poor and the results are very inaccurate for both the ABC and DQ models in both angular velocity and stator voltage perturbation as it was demonstrated in the Tables 5-7 to 5-10. Therefore, some techniques have to be used to find the main source of error and to reduce it.

## 5.5 Result improvement for the measurement based estimations

### 5.5.1 Introduction

In this section, some techniques are employed to rectify the estimation accuracy for the results acquired from the measured signals.

### 5.5.2 Considering the initial conditions

By choosing the initial conditions to be considered and estimated during the estimation, the results might improve. As it was stated in chapter 3, the initial conditions of the system, are the initial value of the stator current signals for each of the three phases, the initial value of the rotor current signals for each phase and the initial position of the rotor. Now, they are chosen

to be estimated during the estimation process, and eventually the effects of this change on estimating the major electrical parameters of the machine will be presented to see the possible improvements.

### 5.5.2.1 Stator voltage perturbation

#### 5.5.2.1.1 ABC model

The estimation results regarding the stator voltage perturbation based on the measured signals for the ABC model, considering the initial conditions are presented in table 5-11.

**Table 5-11: The ABC model Parameter estimation results for the stator voltage perturbation based on the measured signals considering the initial conditions.**

Parameter	Initial Guess	Actual	Estimated	Error
$L_r$ [H]	$10^{-4}$	0.0021194	0.00464212182	-119.03%
$L_s$ [H]	$10^{-4}$	0.0021194	0.00447553698	-111.17%
$L_m$ [H]	$10^{-4}$	0.0419774	0.0916786416	-118.4%
$R_r$ [ $\Omega$ ]	$10^{-4}$	0.7590889	1.436196199	-89.2%
$R_s$ [ $\Omega$ ]	$10^{-4}$	0.4832930	0.904241203	-87.1%

#### 5.5.2.1.2 DQ model

The estimation results regarding the stator voltage perturbation based on the measured signals for the DQ model, considering the initial conditions are presented in table 5-12.



**Table 5-12: The DQ model Parameter estimation results for the stator voltage perturbation based on the measured signals considering the initial conditions.**

Parameter	Initial Guess	Actual	Estimated	Error
$L_r$ [H]	$10^{-4}$	0.0021194	0.004949011	-133.51%
$L_s$ [H]	$10^{-4}$	0.0021194	0.004762292	-124.7%
$L_m$ [H]	$10^{-4}$	0.0419774	-0.03320412	179.1%
$R_r$ [ $\Omega$ ]	$10^{-4}$	0.7590889	1.230710834	-62.13%
$R_s$ [ $\Omega$ ]	$10^{-4}$	0.4832930	0.826672677	-71.05%

### 5.5.2.2 Angular velocity perturbation

#### 5.5.2.2.1 ABC model

The estimation results regarding the angular velocity perturbation based on the measured signals for the ABC model, considering the initial conditions are presented in table 5-13.

**Table 5-13: The ABC model Parameter estimation results for the angular velocity perturbation based on the measured signals considering the initial conditions.**

Parameter	Initial Guess	Actual	Estimated	Error
$L_r$ [H]	$10^{-4}$	0.0021194	0.005100972	-140.68%
$L_s$ [H]	$10^{-4}$	0.0021194	0.004939686	-133.07%
$L_m$ [H]	$10^{-4}$	0.0419774	0.001452418	96.54%
$R_r$ [ $\Omega$ ]	$10^{-4}$	0.7590889	1.337438733	-76.19%
$R_s$ [ $\Omega$ ]	$10^{-4}$	0.4832930	0.914970308	-89.32%

### 5.5.2.2.2 DQ model

The estimation results regarding the angular velocity perturbation based on the measured signals for the DQ model, considering the initial conditions are presented in table 5-14.

**Table 5-14: The DQ model Parameter estimation results for the angular velocity perturbation based on the measured signals considering the initial conditions.**

Parameter	Initial Guess	Actual	Estimated	Error
$L_r$ [H]	$10^{-4}$	0.0021194	0.004918492	-132.07%
$L_s$ [H]	$10^{-4}$	0.0021194	0.004793023	-126.15%
$L_m$ [H]	$10^{-4}$	0.0419774	-0.00431107	-110.27%
$R_r$ [ $\Omega$ ]	$10^{-4}$	0.7590889	1.375165451	-81.16%
$R_s$ [ $\Omega$ ]	$10^{-4}$	0.4832930	0.846197714	-75.06%

### 5.5.3 Windowing the output signals

One of the other possible ways to improve the estimation accuracy is by windowing the first moments of the output signals to alleviate the destructive effects of the start-up transients. This might improve the estimation results. The reason for using this method is that usually in the first moments of the parameter estimation, due to the numerically unstable functions created in the estimation process with very high dimension fluctuations, the cost function might have difficulties reaching the suitable point and converging to the global minimum. Therefore, withdrawing this deteriorating effect is of great importance.

This is feasible by multiplying the signals that the cost function is originated from them (the torque and the three-phase stator and rotor current signals), by a matrix corresponding to the size of these signals with the same dimension. All the arrays of this new matrix in a vector format must be zero (a scholar) for the predetermined period of time, and 1 (a scholar) for the

time after this period, in order to neutralize the high dimension fluctuations during the start-up. An element-wise multiplication is then performed for the newly defined matrix and the output signals for a predetermined period of time that the oscillations happen in that period. Finally, the new output signals are created as a result of these multiplications. The new output signals will then be utilized in order to create the new cost function.

### 5.5.3.1 Stator voltage perturbation

#### 5.5.3.1.1 ABC model

The estimation results regarding the stator voltage perturbation based on the measured signals for the ABC model, considering the windowed start-up output signals are presented in table 5-15.

**Table 5-15: The ABC model Parameter estimation results for the stator voltage perturbation based on the measured signals considering the windowed output signals.**

Parameter	Initial Guess	Actual	Estimated	Error
$L_r$ [H]	$10^{-4}$	0.0021194	0.004360242	-105.73%
$L_s$ [H]	$10^{-4}$	0.0021194	0.004485498	-111.64%
$L_m$ [H]	$10^{-4}$	0.0419774	0.084458529	-101.2%
$R_r$ [ $\Omega$ ]	$10^{-4}$	0.7590889	1.284226601	-69.18%
$R_s$ [ $\Omega$ ]	$10^{-4}$	0.4832930	0.807340957	-67.05%

#### 5.5.3.1.2 DQ model

The estimation results regarding the stator voltage perturbation based on the measured signals for the DQ model, considering the windowed start-up output signals are presented in table 5-16.

**Table 5-16: The DQ model Parameter estimation results for the stator voltage perturbation based on the measured signals considering the windowed output signals.**

Parameter	Initial Guess	Actual	Estimated	Error
$L_r$ [H]	$10^{-4}$	0.0021194	0.004305985	-103.17%
$L_s$ [H]	$10^{-4}$	0.0021194	0.004548444	-114.61%
$L_m$ [H]	$10^{-4}$	0.0419774	0.087497693	-108.44%
$R_r$ [ $\Omega$ ]	$10^{-4}$	0.7590889	1.304494275	-71.85%
$R_s$ [ $\Omega$ ]	$10^{-4}$	0.4832930	0.804972821	-66.56%

### 5.5.3.2 Angular velocity perturbation

#### 5.5.3.2.1 ABC model

The estimation results regarding the angular velocity perturbation based on the measured signals for the ABC model, considering the windowed start-up output signals are presented in table 5-17.

**Table 5-17: The ABC model Parameter estimation results for the angular velocity perturbation based on the measured signals considering the windowed output signals.**

Parameter	Initial Guess	Actual	Estimated	Error
$L_r$ [H]	$10^{-4}$	0.0021194	0.004308528	-103.29%
$L_s$ [H]	$10^{-4}$	0.0021194	0.004419161	-108.51%
$L_m$ [H]	$10^{-4}$	0.0419774	0.086481839	-106.02%
$R_r$ [ $\Omega$ ]	$10^{-4}$	0.7590889	1.242628529	-63.7%
$R_s$ [ $\Omega$ ]	$10^{-4}$	0.4832930	0.782306379	-61.87%

### 5.5.3.2.2 DQ model

The estimation results regarding the angular velocity perturbation based on the measured signals for the DQ model, considering the windowed start-up output signals are presented in table 5-18.

**Table 5-18: The DQ model Parameter estimation results for the angular velocity perturbation based on the measured signals considering the windowed output signals.**

Parameter	Initial Guess	Actual	Estimated	Error
$L_r$ [H]	$10^{-4}$	0.0021194	0.00429666	-102.73%
$L_s$ [H]	$10^{-4}$	0.0021194	0.00438843	-107.06%
$L_m$ [H]	$10^{-4}$	0.0419774	0.087871291	-109.33%
$R_r$ [ $\Omega$ ]	$10^{-4}$	0.7590889	1.23708718	-62.97%
$R_s$ [ $\Omega$ ]	$10^{-4}$	0.4832930	0.780469866	-61.49%

### 5.5.4 Cost function modification

As it was stated before, the cost function is created from the output signals including the torque (mechanical) and the current signals (stator and rotor). Thus, removing each of them might have a noticeable effect of the estimation results and also might indicate that where does the main source of error originate from. In order to find out if the main origin of the high error percentage is coming from the current output signals, or from the torque output signal, in this section, the effects of removing the stator and rotor currents from the cost function are evaluated.

#### 5.5.4.1 Stator voltage perturbation

##### 5.5.4.1.1 ABC model

The estimation results regarding the stator voltage perturbation based on the measured signals for the ABC model, considering the modified cost function (current and voltage output signals removed from the cost function), are presented in table 5-19.

**Table 5-19: The ABC model Parameter estimation results for the stator voltage perturbation based on the measured signals considering the modified cost function.**

Parameter	Initial Guess	Actual	Estimated	Error
$L_r$ [H]	$10^{-4}$	0.0021194	0.004001215	-88.79%
$L_s$ [H]	$10^{-4}$	0.0021194	0.003806654	-79.61%
$L_m$ [H]	$10^{-4}$	0.0419774	0.081490727	-94.13%
$R_r$ [ $\Omega$ ]	$10^{-4}$	0.7590889	1.14751469	-51.17%
$R_s$ [ $\Omega$ ]	$10^{-4}$	0.4832930	0.720348217	-49.05%

**5.5.4.1.2 DQ model**

The estimation results regarding the stator voltage perturbation based on the measured signals for the DQ model, considering the modified cost function (current and voltage output signals removed from the cost function), are presented in table 5-20.

**Table 5-20: The DQ model Parameter estimation results for the stator voltage perturbation based on the measured signals considering the modified cost function.**

Parameter	Initial Guess	Actual	Estimated	Error
$L_r$ [H]	$10^{-4}$	0.0021194	0.003957768	-86.74%
$L_s$ [H]	$10^{-4}$	0.0021194	0.003700049	-74.58%
$L_m$ [H]	$10^{-4}$	0.0419774	0.08072254	-92.3%
$R_r$ [ $\Omega$ ]	$10^{-4}$	0.7590889	1.139696074	-50.14%
$R_s$ [ $\Omega$ ]	$10^{-4}$	0.4832930	0.706719354	-46.23%

### 5.5.4.2 Angular velocity perturbation

#### 5.5.4.2.1 ABC model

The estimation results regarding the angular velocity perturbation based on the measured signals for the ABC model, considering the modified cost function (current and voltage output signals removed from the cost function), are presented in table 5-21.

**Table 5-21: The ABC model Parameter estimation results for the angular velocity perturbation based on the measured signals considering the modified cost function.**

Parameter	Initial Guess	Actual	Estimated	Error
$L_r$ [H]	$10^{-4}$	0.0021194	0.003999732	-88.72%
$L_s$ [H]	$10^{-4}$	0.0021194	0.003777831	-78.25%
$L_m$ [H]	$10^{-4}$	0.0419774	0.079824224	-90.16%
$R_r$ [ $\Omega$ ]	$10^{-4}$	0.7590889	1.154042855	-52.03%
$R_s$ [ $\Omega$ ]	$10^{-4}$	0.4832930	0.717013495	-48.36%

#### 5.5.4.2.2 DQ model

The estimation results regarding the angular velocity perturbation based on the measured signals for the DQ model, considering the modified cost function (current and voltage output signals removed from the cost function), are presented in table 5-22.

**Table 5-22: The DQ model Parameter estimation results for the angular velocity perturbation based on the measured signals considering the modified cost function.**

Parameter	Initial Guess	Actual	Estimated	Error
$L_r$ [H]	$10^{-4}$	0.0021194	0.003923009	-85.10%
$L_s$ [H]	$10^{-4}$	0.0021194	0.003754305	-77.14%
$L_m$ [H]	$10^{-4}$	0.0419774	0.079190365	-88.65%
$R_r$ [ $\Omega$ ]	$10^{-4}$	0.7590889	1.140227437	-50.21%
$R_s$ [ $\Omega$ ]	$10^{-4}$	0.4832930	0.70908749	-46.72%

### 5.5.5 Symmetrical components method

In this section, the effect of partially using the Fortescue [82] method in extracting the symmetrical component from the three-phase system which has fault, is considered to see the possible improvements in the estimation accuracy. The basic idea in the Fortescue method is that a three-phase unbalanced system (containing fault) can be described as three balanced systems with positive, negative and zero sequences. Each of the positive and negative systems, contain a three-phase balanced system, but the zero sequence system contains three single-phase components with the same magnitude [82].

To alleviate the error percentage created by the asymmetry in the system, this method is utilized. Here, the magnitude of the positive sequence system is extracted from the unbalanced voltages and currents (based on their signal peaks and maximum and minimum) and will be used to reconstruct the new voltage and current signals, before and after the perturbation point. Then, this new data will be fed to the estimation algorithms in order to be used in the estimation process. With the new signals taken into the account, the results might improve.

It must be noted that only the magnitude of the positive sequence is employed in this utilization and the effect of “phase shift” is neglected, since the shift in phase can move the perturbation point for the new signals and push them out of synchronization with the other signals in the system. Hence, the positive component is mainly used to scale up or down (adjust) the three phases to reconstruct the new three-phase balanced system.



### 5.5.5.1 Stator voltage perturbation

#### 5.5.5.1.1 ABC model

The estimation results for the stator voltage perturbation based on the measured signals for the ABC model, considering the symmetrical components method are presented in table 5-23.

**Table 5-23: The ABC model Parameter estimation results for the stator voltage perturbation based on the measured signals considering the symmetrical components.**

Parameter	Initial Guess	Actual	Estimated	Error
$L_r$ [H]	$10^{-4}$	0.0021194	0.002522298	-19.01%
$L_s$ [H]	$10^{-4}$	0.0021194	0.002588423	-22.13%
$L_m$ [H]	$10^{-4}$	0.0419774	0.049701242	-18.4%
$R_r$ [ $\Omega$ ]	$10^{-4}$	0.7590889	0.882061302	-16.2%
$R_s$ [ $\Omega$ ]	$10^{-4}$	0.4832930	0.546604383	-13.1%

#### 5.5.5.1.2 DQ model

The estimation results for the stator voltage perturbation based on the measured signals for the DQ model, considering the symmetrical components method are presented in table 5-24.

**Table 5-24: The DQ model Parameter estimation results for the stator voltage perturbation based on the measured signals considering the symmetrical components.**

Parameter	Initial Guess	Actual	Estimated	Error
$L_r$ [H]	$10^{-4}$	0.0021194	0.00247122	-16.6%
$L_s$ [H]	$10^{-4}$	0.0021194	0.002530776	-19.41%
$L_m$ [H]	$10^{-4}$	0.0419774	0.050482021	-20.26%
$R_r$ [ $\Omega$ ]	$10^{-4}$	0.7590889	0.866499979	-14.15%
$R_s$ [ $\Omega$ ]	$10^{-4}$	0.4832930	0.536793535	-11.07%

### 5.5.5.2 Angular velocity perturbation

#### 5.5.5.2.1 ABC model

The estimation results regarding the angular velocity perturbation based on the measured signals for the ABC model, considering the symmetrical components method are presented in table 5-25.

**Table 5-25: The ABC model Parameter estimation results for the angular velocity perturbation based on the measured signals considering the modified cost function.**

Parameter	Initial Guess	Actual	Estimated	Error
$L_r$ [H]	$10^{-4}$	0.0021194	0.002530564	-19.4%
$L_s$ [H]	$10^{-4}$	0.0021194	0.00257931	-21.7%
$L_m$ [H]	$10^{-4}$	0.0419774	0.048685389	-15.98%
$R_r$ [ $\Omega$ ]	$10^{-4}$	0.7590889	0.871661784	-14.83%
$R_s$ [ $\Omega$ ]	$10^{-4}$	0.4832930	0.545154504	-12.8%

### 5.5.5.2.2 DQ model

The estimation results regarding the angular velocity perturbation based on the measured signals for the DQ model, considering the symmetrical components method are shown in table 5-26.

**Table 5-26: The DQ model Parameter estimation results for the angular velocity perturbation based on the measured signals considering the modified cost function.**

Parameter	Initial Guess	Actual	Estimated	Error
$L_r$ [H]	$10^{-4}$	0.0021194	0.002484361	-17.22%
$L_s$ [H]	$10^{-4}$	0.0021194	0.002550486	-20.34%
$L_m$ [H]	$10^{-4}$	0.0419774	0.048467106	-15.46%
$R_r$ [ $\Omega$ ]	$10^{-4}$	0.7590889	0.866499979	-14.15%
$R_s$ [ $\Omega$ ]	$10^{-4}$	0.4832930	0.531767288	-10.03%

### 5.5.6 Conclusion

The estimation results obtained from the Tables 5-11 to 5-26, shows that considering the initial conditions to be estimated, and also windowing the start-up transients, do not have a noticeable effect on the estimation accuracy, though it makes estimation accuracy slightly better. Modifying the cost function has a more significant effect on estimation accuracy, compared to the previous methods, but the results are still inaccurate. On the other hand, effects of employing the symmetrical components method are by far greater than the other methods and results have a great accuracy with a maximum error of about 22%.

## 6 CONCLUSIONS AND RECOMMENDATIONS

All the parameter estimations in the previous chapter, showed a great accuracy in estimations when the simulated signals were employed, with a maximum error of about 1%. As it was mentioned before, this accuracy is a result of the proper selection of the estimation options shown in Table 5-1, and also the fact that the ideal situations were considered without any noises or imperfections in the signals. A summary of the results for these estimations and the average error percentage in estimating the parameters is given in Table 6-1. It must be noticed that the absolute values for the error percentages are considered and the effects of negative signs are neglected.

**Table 6-1: Average error percentages for the parameter estimation results based on the simulated signals.**

Perturbation type	ABC model average error %	DQ model average error %
Stator voltages	0.2576	0.502
Angular velocity	0.064	0.083

In cases where the measured signals were used (instead of the simulated signals), a noticeable inaccuracy was evident, mostly due to the following reasons which affect the accuracy of the offline methods and was addressed before in literature:

- Sampling rate selections
- Quantization errors
- Resolution
- The accuracy of the sensors

For the purpose of parameter estimation, all of the input and output signals have to have the same time interval and sampling rate and consequently the same data points. This synchronization in Labview was done by using Align & resample VI function with some compromises. Because of the rotary encoder's accuracy, and its measurement mode which was discrete unlike the other tasks, in the beginning, it was not possible to sample angular velocity measurement as fast as the other tasks. Also, the time interval for its output was not

synchronized with the other tasks. So, the output signals were resampled. Plus, unlike the other cards, one of the measurement cards (NI-9237) could only take a certain selection of sampling rates and it was needed to define the whole system's sampling frequency based on that.

Therefore, it is not guaranteed that the signals are completely and 100% synchronized in reality. The other problem was that the three-phase wounded rotor Induction machine used as a DFIG has one issue. One of the phases is drawing a noticeably more current than the other two phases and this was evident in both the DC and AC tests. It was obvious during the DC tests that one of the phases has a deviation from its expected current and voltage for the tests and it has probably a lower impedance than the other two phases which was proven by using different measurement devices (this problem can also be related the test bench), other than the machine. Consequently, the above-mentioned problems cause the system to act as an unbalanced and asymmetric machine as opposed to what we expect and also the fact that the model used for simulation and also parameter estimation, is based on a three-phase balanced system in ideal conditions.

The other problem similar to above one, is that the test bench used in the tests was not providing the machine with smooth three-phase sinusoidal waves and for the phase A, the voltage is slightly higher than the other two phases. This can also contribute to a high, unequal and asymmetric error for different phases in the process of parameter estimation. The test bench should have three-phase smooth sinusoidal waves with equal dimensions. It was shown in the figures 5-11 and 5-12 that the peaks for signals have different shapes, some have sharp peaks and some have round peaks, other than different dimensions in a period which was evident for different phases.

Furthermore, for the angular velocity perturbation, it was not possible to perform the perturbation as quick as expected like the MATLAB simulations. The reason for that is that the machine's shaft has inertia and cannot change instantaneously like the ideal simulations. Moreover, for the stator voltage perturbation, another limitation was that it was not possible to change the voltage of the bench very much because the bench was being pushed to its current limitations that might cause the circuit breaker of the bench to deploy.

Considering all the problems stated above during the estimation process, including the practical limitations and hardware imperfections, the parameters will never converge to a global minimum and estimation process will terminate without reaching to an acceptable margin of

error because of have high percentage of error for one of the phases and asymmetric and unbalanced error for my signals.

It was evident that in such cases, the parameter tends to converge either to the minimum or the maximum interval defined for that. In the cases studied in this research, the parameters tend to converge to the maximum number which causes the final parameter to be much greater than the actual parameters and the error becomes negative most of the time.

In the “results improvement” section in chapter 5, several methods were evaluated but most of them had little effect on the results, except for the last method. Analysing the results obtained from such methods gives the following conclusions:

- By considering the initial conditions to be estimated, the estimation results were slightly improved.
- Windowing the start-up transients also did not make a significant change in the results and only a very minor improvement was evident.
- The cost function modification showed that by removing the stator and rotor current signals from the cost function, results can improve noticeably compared to the previous methods, but they are still highly inaccurate with high percentages of error. This showed that the major source of the error comes from the asymmetric current and voltage signals measured in the practical tests.
- The estimation results did not change significantly despite all the previous methods which were implemented. However, by making use of the Fortescue symmetrical components method and extracting the positive components for the corresponding current and voltage signals and reconstructing the three-phase currents, followed by the voltage signals accordingly, the results were significantly improved and a better accuracy was achieved with a maximum error of about 22%, but it still has room for a better accuracy and more improvement.

Briefly, A summary of the average error percentages regarding the parameter estimation results, before and after making use of the above-mentioned methods are presented in the Tables 6-2 and 6-3 respectively.

**Table 6-2: Average error percentages for the parameter estimation results based on the measured signals.**

Perturbation type	ABC model average error %	DQ model average error %
Stator voltages	135.54	122.296
Angular velocity	133.6176	127.81

**Table 6-3: Average error percentages for the parameter estimation results based on the measured signals considering the improvements.**

Improvement method	Stator voltages perturbation		Angular velocity perturbation	
	ABC model	DQ model	ABC model	DQ model
Considering the initial conditions	104.98	114.098	107.16	104.942
Windowing the output signals	90.96	92.926	88.678	88.716
Cost function modification	72.55	69.998	71.504	69.564
Symmetrical components	17.768	16.298	16.942	15.44

It is recommended that:

- More accurate sensors to be used
- Better synchronization of the tasks can be done by using better data acquisition systems since the data points might not correlate precisely while using interpolation.
- Higher sampling rate to be chosen in a way suitable to the hardware that the system does not run out of memory while running estimation.
- A three-phase unbalanced model to be used to improve accuracy.
- All the above-mentioned recommendations must be implemented together since a three-phase unbalanced model cannot fix all the inaccuracies solely.

## 7 REFERENCES

- [1] T. Ackermann, *Wind Power in Power Systems*, 2nd Edition, Wiley, 2012.
- [2] Azad, S.P.; Tate, J.E., "Parameter estimation of doubly fed induction generator driven by wind turbine," Power Systems Conference and Exposition (PSCE), 2011 IEEE/PES, vol., no., pp.1,8, 20-23 March 2011.
- [3] P. Vas, *Parameter Estimation, Condition Monitoring, and Diagnosis of Electrical Machines*, Oxford: Clarendon Press, 1998.
- [4] Toliyat, H.A.; Levi, E.; Raina, M., "A review of RFO induction motor parameter estimation techniques," Energy Conversion, IEEE Transactions on, vol.18, no.2, pp.271,283, June 2003.
- [5] Iov, F., Hansen, A.D., Sorensen, P., Blaabjerg, F., "Wind Turbine Blockset in Matlab/Simulink". Aalborg: Aalborg University, Inc., 2004.
- [6] Bekker, J.C.; Vermeulen, H.J., "Parameter estimation of a doubly-fed induction generator in a wind generation topology," Universities Power Engineering Conference (UPEC), 2012 47th International, vol., no., pp.1,6, 4-7 Sept. 2012.
- [7] V. Quaschnig, *Understanding Renewable Energy Systems*. London: Earthscan, 2006; 2005.
- [8] M. R. Patel, *Wind and Solar Power Systems*. Boca Raton, Fla.:CRC Press, 1999.
- [9] T. Wizelius, *Developing Wind Power Projects: Theory and Practice*. London: Earthscan, 2007.
- [10] T. Burton, D. Sharpe, N. Jenkins, E. Bossanyi, "Wind Energy Handbook," 1st Edition, Wiley, 2001.
- [11] J. H. J. Potgieter and M. J. Kamper, "Design of New Concept Direct Grid-Connected Slip-Synchronous Permanent-Magnet Wind Generator," in *IEEE Transactions on Industry Applications*, vol. 48, no. 3, pp. 913-922, May-June 2012.
- [12] L. Ljung, *System Identification: Theory for the User*. Upper Saddle River, NJ: Prentice Hall PTR, 1999.
- [13] T. Soderstrom and P. Stoica, *System Identification*. New York, N.Y.: Prentice-Hall, 1989.
- [14] J. C. Bekker and H. J. Vermeulen, "Implementation of a wind turbine system as a native C-code MATLAB model for parameter estimation application," in 46th International Universities' Power Engineering Conference, Soest, Germany, 2011, pp. 88.
- [15] J. Nocedal and S. J. Wright, *Numerical Optimization*. New York: Springer, 1999.
- [16] D. G. Luenberger and Y. Ye, *Linear and Nonlinear Programming*. Springer Verlag, 2008.
- [17] J. Zhang, *Iterative Methods for Optimization*. USA: Purdue University, 2008.



- [18] D. J. Higham, "Trust Region Algorithms and Timestep Selection," *SIAM Journal on Numerical Analysis*, vol. 37, pp. 194-210, 2000.
- [19] P. Vas, *Sensorless Vector and Direct Torque Control*. London, U.K.: Oxford Univ. Press, 1998.
- [20] E. Levi, "Impact of iron loss on behavior of vector controlled induction machines," *IEEE Trans. Ind. Applicat.*, vol. 31, pp. 1287-1296, Nov./Dec. 1995.
- [21] H. Schierling, "Self-commissioning—A novel feature of modern inverter-fed induction motor drives," in *Proc. Inst. Elect. Eng. Conf. Power Electron. Variables Speed Drives*, 1988, pp. 287-290.
- [22] M. Ruff, A. Bünte, and H. Grotstollen, "A new self-commissioning scheme for an asynchronous motor drive system," in *Proc. IEEE Ind. Applicat. Soc. Annu. Meeting*, 1994, pp. 612-623.
- [23] A. Bünte and H. Grotstollen, "Offline parameter identification of an inverter-fed induction motor at standstill," in *Proc. Europe. Conf. Power Electron. Applicat.*, 1995, pp. 3.492-3.496.
- [24] C. Wang, D. W. Novotny, and T. A. Lipo, "An automated rotor time constant measurement system for indirect field-oriented drives," *IEEE Trans. Ind. Applicat.*, vol. 24, pp. 151-159, Jan./Feb. 1988.
- [25] P. J. Chrzan and H. Klaassen, "Parameter identification of vector-controlled induction machines," *Electrical Engineering*, vol. 79, no. 1, pp.39-46, 1996.
- [26] S. I. Moon and A. Keyhani, "Estimation of induction machine parameters from standstill time-domain data," *IEEE Trans. Ind. Applicat.*, vol. 30, pp. 1606-1615, Nov./Dec. 1994.
- [27] M. Ruff and H. Grotstollen, "Identification of the saturated mutual inductance of an asynchronous motor at standstill by recursive least squares algorithm," in *Proc. Europe. Conf. Power Electron. Applicat.*, vol. 5, 1993, pp. 103-108.
- [28] M. Bertoluzzo, G. S. Buja, and R. Menis, "Self-commissioning of RFO IM drives: One-test identification of the magnetization characteristic of the motor," *IEEE Trans. Ind. Applicat.*, vol. 37, pp. 1801-1806, Nov./Dec. 2001.
- [29] M. Bertoluzzo, G. Buja, and R. Menis, "Identification techniques of induction motor parameters for self-commissioning field-oriented drives," *Automatika*, vol. 38, no. 3-4, pp. 103-115, 1997.
- [30] R. D. Lorenz, "Tuning of field oriented induction motor controllers for high performance applications," in *Proc. IEEE Ind. Applicat. Soc. Annu. Meeting*, 1985, pp. 607-612.
- [31] A. Boglietti, P. Ferraris, M. Lazzari, and F. Profumo, "Induction motor equivalent circuit parameters determination from standard tests made with inverter supply," in *Proc. Inst. Elect. Eng. Elect. Mach. Drives Conf.*, 1993, pp. 271-276.

- [32] Y. N. Lin and C. L. Chen, "Automatic induction motor parameter measurement under sensorless field-oriented control," in Proc. IEEE Int. Symp. Ind. Electron., 1996, pp. 894–899.
- [33] E. Levi, M. Sokola, and S. N. Vukosavic, "A method for magnetizing curve identification in rotor flux oriented induction machines," IEEE Trans. Energy Conversion, vol. 15, pp. 157–162, June 2000.
- [34] E. Levi and S. N. Vukosavic, "Identification of the magnetizing curve during commissioning of a rotor flux oriented induction machine," Proc. Inst. Elect. Eng.—Elect. Power Applicat., vol. 146, no. 6, pp. 685–693, 1999.
- [35] E. Levi, "Method of magnetizing curve identification in vector controlled induction machines," Europe. Trans. Elect. Power, vol. 2, no. 5, pp. 309–314, 1992.
- [36] A. Ganji, P. Guillaume, R. Pintelon, and P. Lataire, "Induction motor dynamic and static inductance identification using a broadband excitation technique," IEEE Trans. Energy Conversion, vol. 13, pp. 15–20, March 1998.
- [37] A. Stankovic, E. R. Benedict, V. John, and T. A. Lipo, "A novel method for measuring induction machine magnetizing inductance," in Proc. IEEE Ind. Applicat. Soc. Annu. Meeting, 1997, pp. 234–238.
- [38] V. Staudt, "Measuring differential inductances of asynchronous machines," Europe. Trans. Elect. Power, vol. 4, no. 1, pp. 27–33, 1994.
- [39] E. Levi, M. Sokola, A. Boglietti, and M. Pastorelli, "Iron loss in rotor flux oriented induction machine: Identification, assessment of detuning and compensation," IEEE Trans. Power Electron., vol. 11, pp. 698–709, Sept. 1996.
- [40] D. E. Borgard, G. Olsson, and R. D. Lorenz, "Accuracy issues for parameter estimation of field oriented induction machine drives," IEEE Trans. Ind. Applicat., vol. 31, pp. 795–801, July/Aug. 1995.
- [41] G. S. Buja, R. Menis, and M. I. Valla, "MRAS identification of the induction motor parameters in PWM inverter drives at standstill," in Proc. IEEE Ind. Electron. Soc. Annu. Meeting, 1995, pp. 1041–1041.
- [42] M. Bertoluzzo, G. S. Buja, and R. Menis, "Inverter voltage drop-free recursive least-squares parameter identification of a PWM inverter-fed induction motor at standstill," in Proc. IEEE Int. Symp. Ind. Electron., 1997, pp. 649–654.
- [43] A. Gastli, "Identification of induction motor equivalent circuit parameters using the single-phase test," IEEE Trans. Energy Conversion, vol. 14, pp. 51–56, Mar. 1999.
- [44] T. Matsuo and T. A. Lipo, "A rotor parameter identification scheme for vector controlled induction motor drives," IEEE Trans. Ind. Applicat., vol. IA-21, pp. 624–632, May/June 1985.

- [45] H. A. Toliyat and A. A. GH. Hosseiny, "Parameter estimation algorithm using spectral analysis for vector controlled induction motor drives," in Proc. IEEE Int. Symp. Ind. Electron., 1993, pp. 90–95.
- [46] H. Chai and P. P. Acarnley, "Induction motor parameter estimation algorithm using spectral analysis," Proc. Inst. Elect. Eng., pt. B, vol. 139, no. 3, pp. 165–174, 1992.
- [47] R. Gabriel and W. Leonhard, "Microprocessor control of induction motor," in Proc. Int. Semiconductor Power Conversion Conf., 1982, pp. 385–396.
- [48] H. Sugimoto and S. Tamai, "Secondary resistance identification of an induction motor—Applied model reference adaptive system and its characteristics," IEEE Trans. Ind. Applicat., vol. IA-23, pp. 296–303, Mar./Apr. 1987.
- [49] E. Cerruto, A. Consoli, A. Raciti, and A. Testa, "Slip gain tuning in indirect field oriented control drives," Electric Machines and Power Systems, vol. 23, pp. 63–79, 1995.
- [50] J. Cilia, G. M. Asher, J. Shuli, M. Sumner, K. J. Bradley, and A. Ferrah, "The recursive maximum likelihood algorithm for tuning the rotor time constant in high-performance sensorless induction motor drives," in Proc. Int. Conf. Elect. Mach., 1998, pp. 926–930.
- [51] R. Kalman, "On the general theory of control systems," in IRE Transactions on Automatic Control, vol. 4, no. 3, pp. 110–110, Dec 1959.
- [52] J. W. Moore and R. Oldenburger, "Rapid Methods for the Solution of Automatic Control Equations," in IEEE Transactions on Applications and Industry, vol. 82, no. 68, pp. 286–295, Sept. 1963.
- [53] E. A. Wan and R. Van Der Merwe, "The unscented Kalman filter for nonlinear estimation," Proceedings of the IEEE 2000 Adaptive Systems for Signal Processing, Communications, and Control Symposium (Cat. No.00EX373), Lake Louise, Alta., 2000, pp. 153–158.
- [54] L. Loron and G. Laliberté, "Application of the extended Kalman filter to parameters estimation of induction motors," in Proc. Europe. Conf. Power Electron. Applicat., vol. 5, 1993, pp. 85–90.
- [55] L. C. Zai, C. L. DeMarco, and T. A. Lipo, "An extended Kalman filter approach to rotor time constant measurement in PWM induction motor drives," IEEE Trans. Ind. Applicat., vol. 28, pp. 96–104, Jan./Feb. 1992.
- [56] T. Kataoka, S. Toda, and Y. Sato, "On-line estimation of induction motor parameters by extended Kalman filter," in Proc. Europe. Conf. Power Electron. Applicat., vol. 4, 1993, pp. 325–329.
- [57] J.W. Finch, D. J. Atkinson, and P. P. Acarnley, "Full-order estimator for induction motor states and parameters," Proc. Inst. Elect. Eng. Elect. Power Applicat., vol. 145, no. 3, pp. 169–179, 1998.

- [58] D. G. Luenberger, "Observing the State of a Linear System," in IEEE Transactions on Military Electronics, vol. 8, no. 2, pp. 74-80, April 1964.
- [59] T. Du, P. Vas, and F. Stronach, "Design and application of extended observers for joint state and parameter estimation in high-performance AC drives," Proc. Inst. Elect. Eng.—Elect. Power Applicat., vol. 142, no. 2, pp. 71–78, 1995.
- [60] T. Du and M. A. Brdys, "Implementation of extended Luenberger observers for joint state and parameter estimation of PWM induction motor drive," in Proc. Europe. Conf. Power Electron. Applicat., vol. 4, 1993, pp. 439–444.
- [61] S. Wade, M. W. Dunnigan, and B. W. Williams, "Improvements for induction machine vector control," in Proc. Europe. Conf. Power Electron. Applicat., 1995, pp. 1.542–1.546.
- [62] J. Bongiorno, "Stability and convergence properties of model-reference adaptive control systems," in IRE Transactions on Automatic Control, vol. 7, no. 3, pp. 30-41, Apr 1962.
- [63] G. Griva, M. C. Ficcaro, and F. Profumo, "Design of a speed regulator for induction motor drives based on model reference robust control," in Proc. IEEE Int. Symp. Ind. Electron., 1997, pp. 485–488.
- [64] S. N. Vukosavic and M. R. Stojic, "On-line tuning of the rotor time constant for vector-controlled induction motor in position control applications," IEEE Trans. Ind. Electron., vol. 40, pp. 130–138, Feb. 1993.
- [65] D. Y. Ohm, Y. Khersonsky, and J. R. Kimzey, "Rotor time constant adaptation method for induction motors using DC link power measurement," in Proc. IEEE Ind. Applicat. Soc. Annu. Meeting, 1989, pp. 588–593.
- [66] S. K. Sul, "A novel technique of rotor resistance estimation considering variation of mutual inductance," IEEE Trans. Ind. Applicat., vol. 25, pp. 578–587, July/Aug. 1989.
- [67] A. Ba-razzouk, A. Cheriti, and V. Rajagoplan, "Real time implementation of a rotor time-constant online estimation scheme," in Proc. IEEE Ind. Electron. Soc. Annu. Meeting, 1999, pp. 927–932.
- [68] S. Mayaleh and N. S. Bayindir, "On-line estimation of rotor-time constant of an induction motor using recurrent neural networks," in Proc. IEEE Workshop Comput. Power Electron., 1998, pp. 219–223.
- [69] M. Ta-Cao and H. Le-Huy, "Rotor resistance estimation using fuzzy logic for high performance induction motor drives," in Proc. IEEE Ind. Electron. Soc. Annu. Meeting, 1998, pp. 303–308.
- [70] V. Ambrozic, D. Nedeljkovic, and J. Nastran, "Sensorless control of induction machine with parameter adaptation," in Proc. IEEE Int. Symp. Ind. Electron., 1999, pp. 724–728.

- [71] M. Tsuji, S. Chen, K. Izumi, and E. Yamada, "A sensorless vector control system for induction motors using  $q$ -axis flux with stator resistance identification," IEEE Trans. Ind. Electron., vol. 48, pp. 185–194, Feb. 2001.
- [72] E. Levi, "A unified approach to main flux saturation modelling in  $d$ - $q$  axis models of induction machines," IEEE Trans. Energy Conversion, vol. 10, pp. 455–461, Sept. 1995.
- [73] R. C. Healey, S. Williamson, and A. C. Smith, "Improved cage rotor models for vector controlled induction motors," IEEE Trans. Ind. Applicat., vol. 31, pp. 812–822, July/Aug. 1995.
- [74] S. D. Wee, M. H. Shin, and D. S. Hyun, "Stator-flux-oriented control of induction motor considering iron loss," IEEE Trans. Ind. Electron., vol. 48, pp. 602–608, June 2001.
- [75] H. Rasmussen, P. Vadstrup, and H. Borsting, "Rotor field oriented control with adaptive iron loss identification," in Proc. IEEE Ind. Applicat. Soc. Annu. Meeting, 1999, pp. 1253–1258.
- [76] S. Santoso and H. T. Le, "Fundamental time-domain wind turbine models for wind power studies," Renewable Energy, vol. 32, pp. 2436–2452, 11, 2007.
- [77] M. R. Patel, *Wind and Solar Power Systems - Design, Analysis, and Operation*. Boca Raton, Florida: CRC, 2006.
- [78] P. Krause, O. Wasynczuk and S. Sudhoff, *Analysis of Electric Machinery and Drive Systems*, 2002.
- [79] N. N. Hancock, *Matrix Analysis of Electrical Machinery*. Oxford: Pergamon, 1964.
- [80] D. O'Kelly and S. Simmons, *Introduction to Generalized Electrical Machine Theory*. London: McGraw-Hill, 1968.
- [81] MathWorks, "Simulink 7 - Writing S-functions," 2008.
- [82] Fitzgerald, A.E., Kingsley, C., Jr., and Umans, S.D., *Electric Machinery*, 6th ed., McGraw-Hill, Burr Ridge, IL, 2003.
- [83] Dominique Placko, "Fundamentals of Instrumentation and Measurement", January 2010.
- [84] National Instruments official website, available at: [www.ni.com](http://www.ni.com).

## **APPENDIX A: LABVIEW IMPLEMENTATION OF MEASUREMENT SYSTEM**

### **A.1.1 Introduction**

In this appendix, the block diagrams for the implementation of the measurement system in Labview is shown for each measurement task. Then, the front panel regarding the whole measurement system including all the tasks is shown.

Due to the scale and size of these pictures, they are shown in the next pages.

### A.1.2 Current and voltage tasks

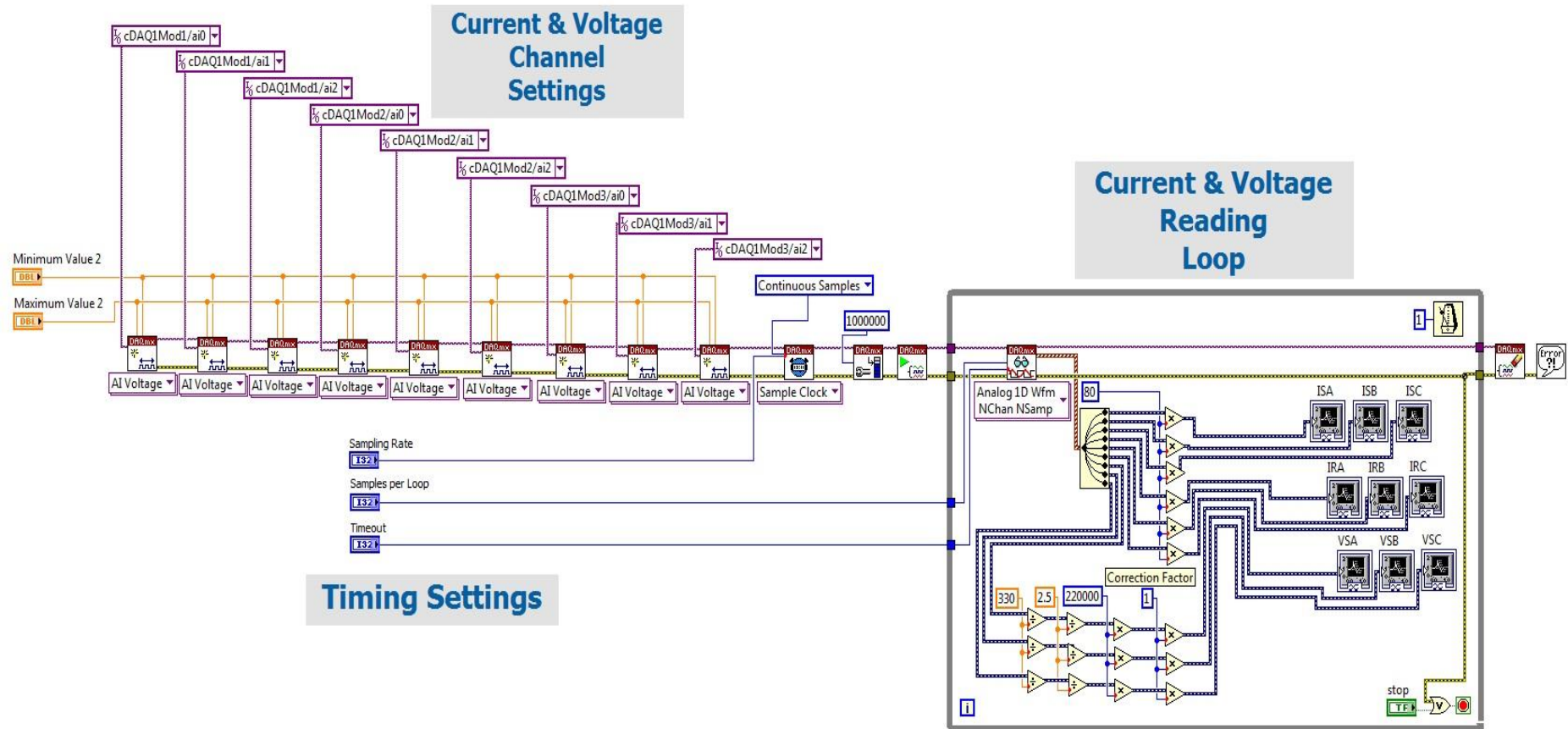


Figure 7-1 Current and voltage tasks

### A.1.3 Torque reading task

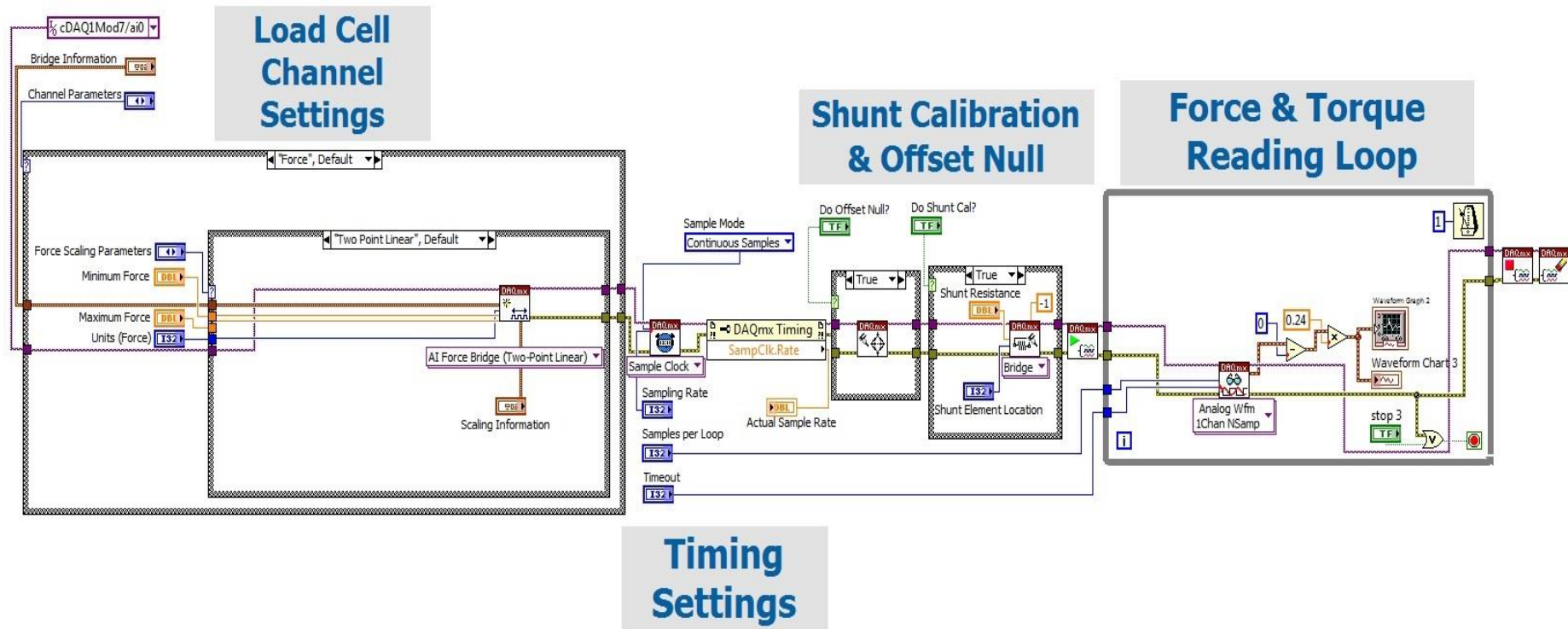


Figure 7-2 Torque reading task



### A.1.4 Angular velocity and position measurement task

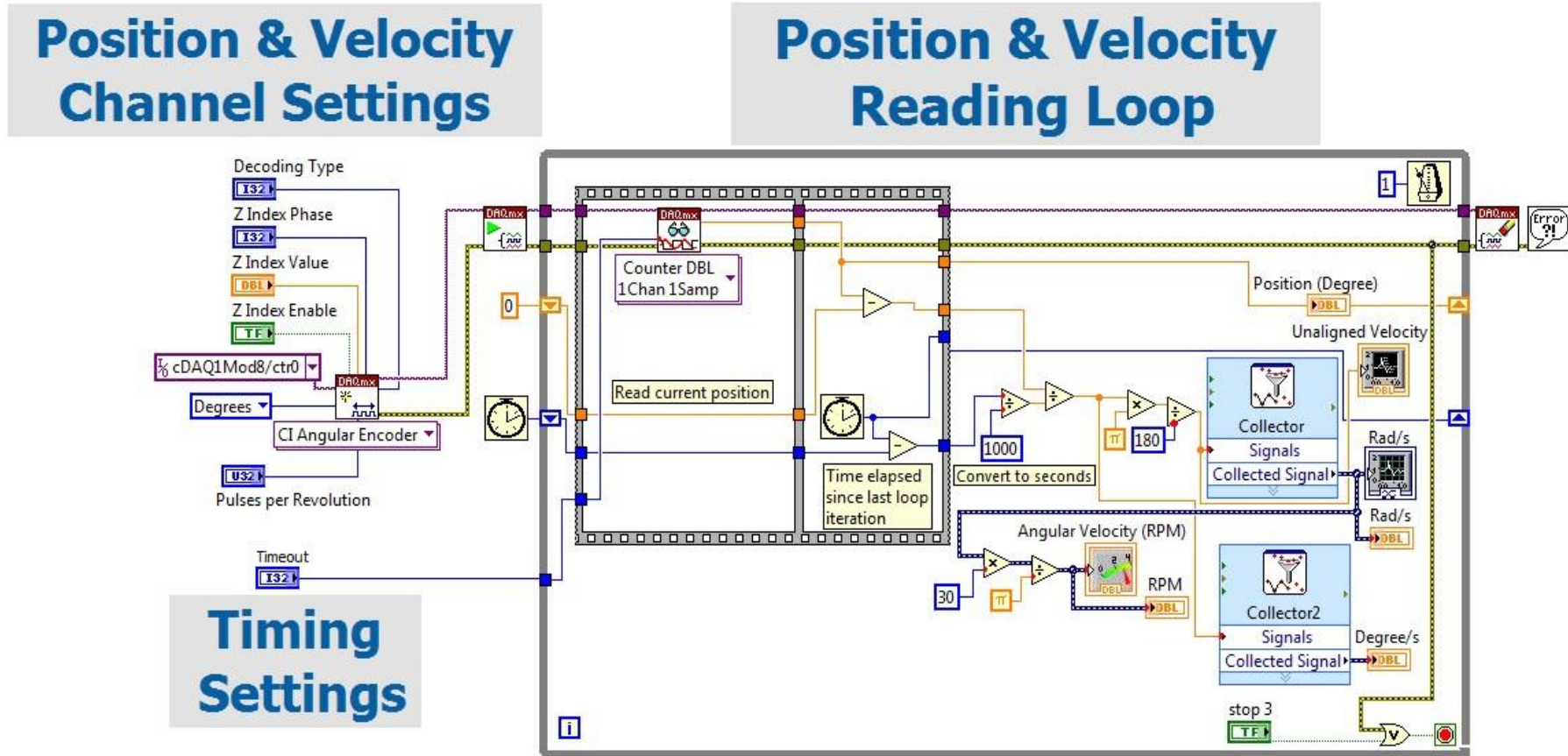
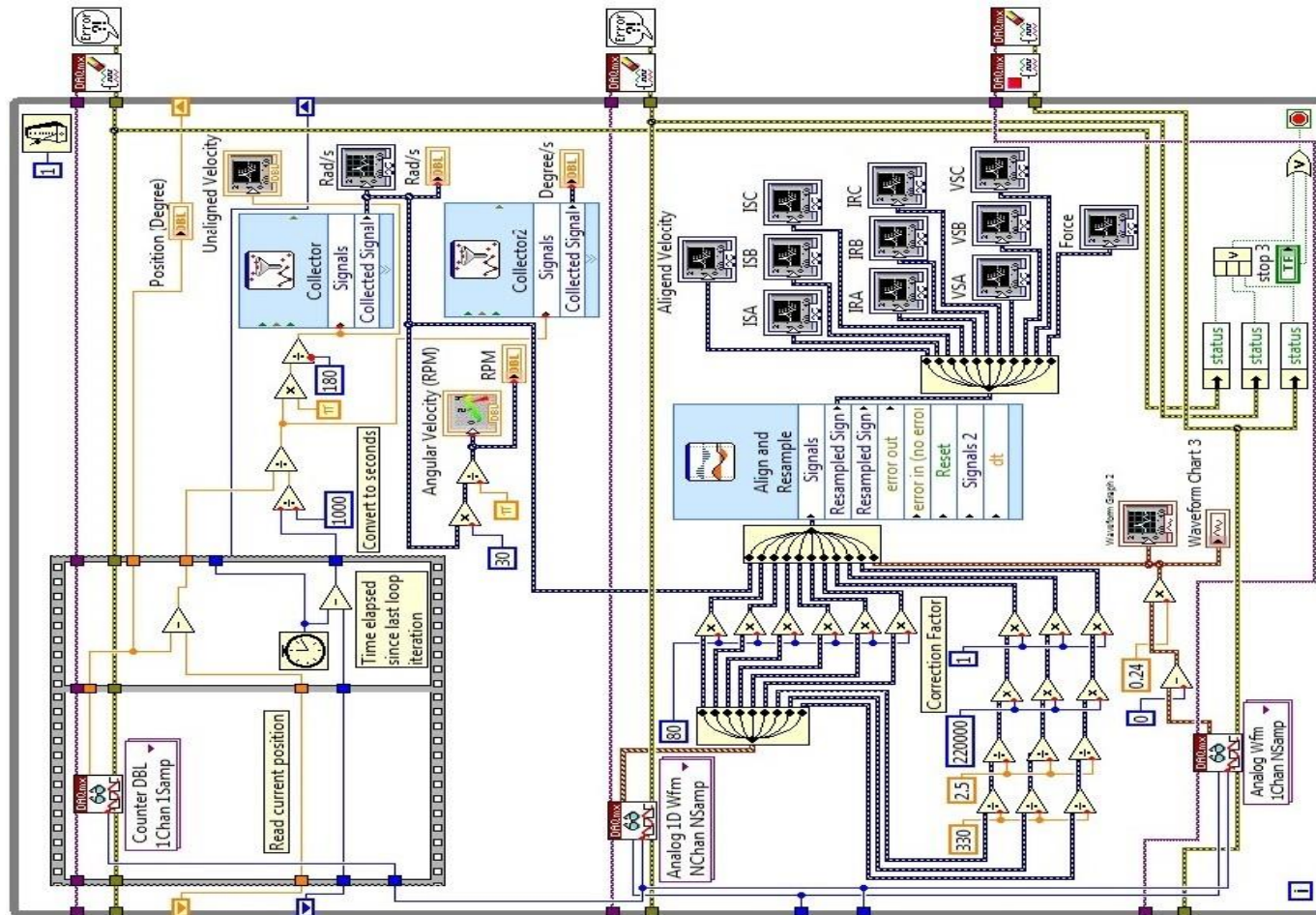


Figure 7-3 Angular velocity and position measurement task

### A.1.5 Measurements synchronization task



Reading Data and Synchronizing all the Signals

Figure 7-4 Measurements synchronization task

### A.1.6 Complete System including all tasks

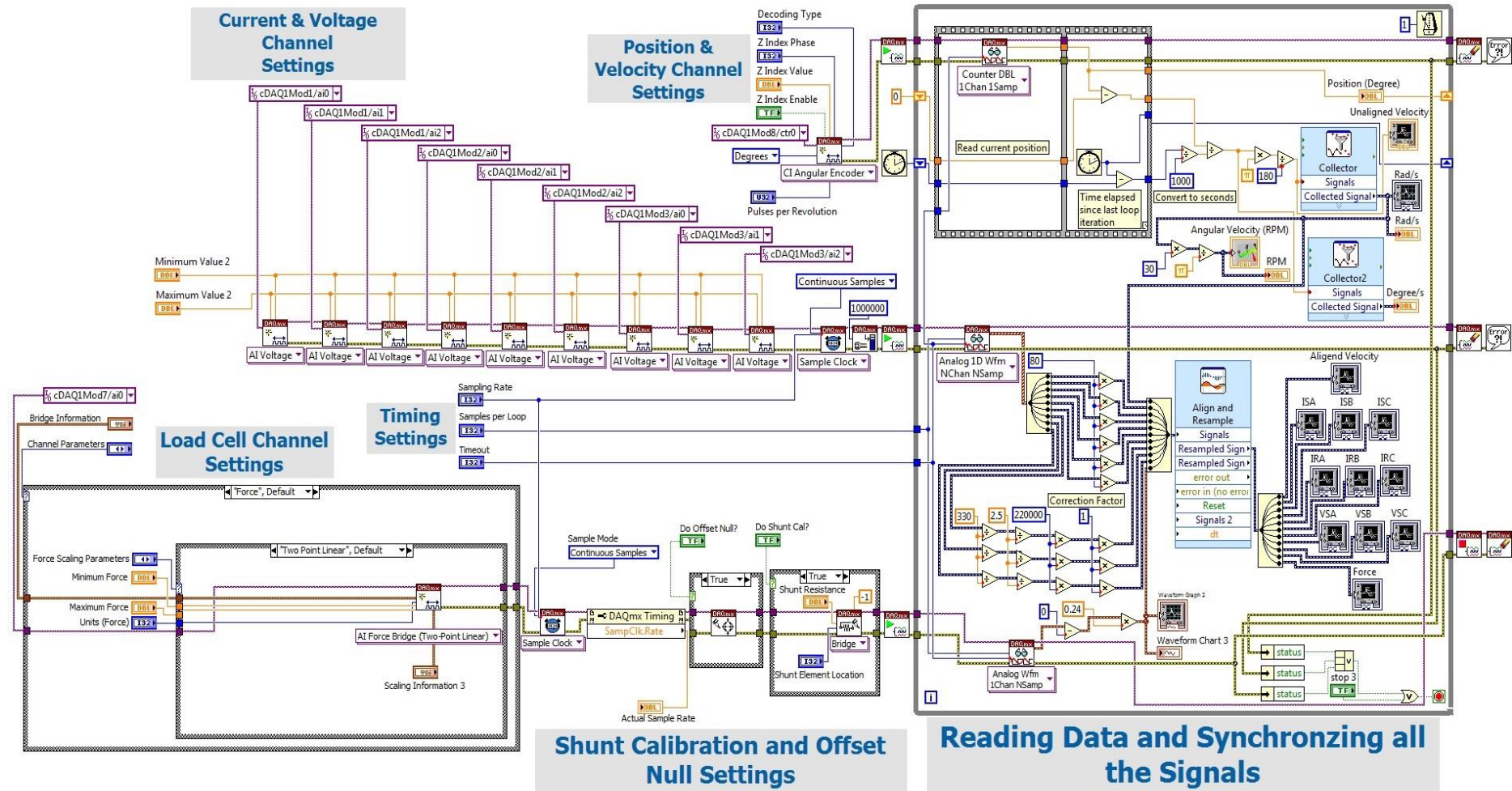


Figure 7-5 Complete System including all tasks

## APPENDIX B: DATA SHEETS

### B.1.1 Introduction

In this section, all the technical data regarding the sensors and also the data acquisition system is provided.

### B.1.2 CNCELL PA6110 200 kg load cell datasheet

PA6110/6210



**STANDARD CAPACITY :**

5,10,25,50,100,150,200,250,500,750 lb  
 1,1.5,2,2.5,3,5,10,15,20 klb  
 2.5,5,15,25,50,70,100,150,250,300 kg  
 0.5,0.7,1,1.5,2,2.5,5,7,10,20 t

**WIRING:**

RED +INPUT GREEN +OUTPUT  
 BLACK -INPUT WHITE -OUTPUT  
 4 COLOR SHIELD CABLE 20FT(6m)

**● Specifications**

Rated output	2.95~3.05mV/V
Accuracy class	0.03 0.05 C3
Non-linearity	0.03%F-S
Hysteresis	0.03%(PA6110) 0.05%(PA6210)
Non-repeatability	0.02%F-S
Creep in 30 minutes	0.03%F-S
Temperature effect span	15 PPM / °C of Applied Load
Temperature effect zero	26 PPM / °C of Applied Load
Compensated temperature range	-10 °C~40 °C
Operating temperature range	-40 °C~65 °C
Zero balance	± 1%F-S
Input resistance	385 ± 15 Ω
Output resistance	350 ± 3 Ω
Safe overload	150%F-S
Ultimate overload	300%F-S
Excitation voltage	10VAC/DC
Maximum excitation voltage	15VAC/DC
Insulation resistance	≥ 5000M Ω (50V DC)
Environmental protection	IP67
Material	Alloy tool steel(PA6110 ) Stainless steel(PA6210)

※All specifications are a maximum as a%( ± ) of full load, otherwise stated.

Capacity	A	B	H	D
50~50lb	2.00	0.50	2.50	1/4-28UNF-2B
100~200lb	2.00	0.50	3.00	1/4-28UNF-2B
250lb	2.00	0.75	3.00	3/8-24UNF-2B
500~1500lb	2.00	0.75	3.00	1/2-20UNF-2B
2~3klb	2.00	1.00	3.00	1/2-20UNF-2B
5~10klb	3.00	1.00	4.25	3/4-16UNF-2B
15klb	4.00	1.25	5.50	1-14UNF-2B
20klb	5.00	2.00	7.00	1 1/4-12UNF-2B
2.5~25kg	51	12	63	M6
50~70kg	51	12	75	M6
100~700kg	51	19	75	M12
1~1.5t	51	25	75	M12
2~5t	76	25	108	M20X1.5
7t	102	32	140	M20X1.5
10t	127	50	178	M30X2
20t	160	60	190	M36X3

(inch/mm)



-1-

YUYAO PACIFIC AUTO-CONTROL ENGINEERING CO., LTD.

Figure 7-6 CNCELL PA6110 200 kg load cell datasheet

### B.1.3 LEM Hass 50-S current sensor electrical data

Electrical data			
	Primary nominal rms current $I_{PN}$ (A)	Primary current measuring range $I_{PM}$ (A)	Type
	50	$\pm 150$	<b>HASS 50-S</b>
	100	$\pm 300$	<b>HASS 100-S</b>
	200	$\pm 600$	<b>HASS 200-S</b>
	300	$\pm 900$	<b>HASS 300-S</b>
	400	$\pm 1100$	<b>HASS 400-S</b>
	500	$\pm 1100$	<b>HASS 500-S</b>
	600	$\pm 1100$	<b>HASS 600-S</b>
$G_{Th}$	Theoretical sensitivity @ $I_{PN}$		0.625 V/ $I_{PN}$
$V_{out}$	Analog output voltage @ $I_P$		$V_{OE} \pm (0.625 \cdot I_P / I_{PN})V$
$V_{ref}$	Reference voltage <sup>1)</sup>	Output voltage	$2.5 \pm 0.025$ V
		Output impedance	typ. 200 $\Omega$
		Load impedance	$\geq 200$ $\Omega$
$R_L$	Load resistance		$\geq 2$ k $\Omega$
$R_{out}$	Output internal resistance		$< 5$ $\Omega$
$C_L$	Capacitive loading ( $\pm 20\%$ )		$= 4.7$ nF
$U_C$	Supply voltage ( $\pm 5\%$ ) <sup>2)</sup>		5 V
$I_C$	Current consumption @ $U_C = 5$ V		19 (typ) mA
			25 (max) mA

**Figure 7-7 LEM Hass 50-S current sensor electrical data**

### B.1.4 LEM LV 25-P voltage transducer technical data

Electrical data				
$I_{PN}$	Primary nominal rms current		10	mA
$I_{PM}$	Primary current, measuring range		0 .. $\pm 14$	mA
$R_M$	Measuring resistance		$R_{M \min}$ $R_{M \max}$	
		with $\pm 12$ V	@ $\pm 10$ mA <sub>max</sub>	30   190 $\Omega$
			@ $\pm 14$ mA <sub>max</sub>	30   100 $\Omega$
		with $\pm 15$ V	@ $\pm 10$ mA <sub>max</sub>	100   350 $\Omega$
		@ $\pm 14$ mA <sub>max</sub>	100   190 $\Omega$	
$I_{SN}$	Secondary nominal rms current		25	mA
$K_N$	Conversion ratio		2500 : 1000	
$U_C$	Supply voltage ( $\pm 5$ %)		$\pm 12$ .. 15	V
$I_C$	Current consumption		10 (@ $\pm 15$ V) + $I_S$	mA
Accuracy - Dynamic performance data				
$X_G$	Overall accuracy @ $I_{PN}, T_A = 25$ °C	@ $\pm 12$ .. 15 V	$\pm 0.9$	%
		@ $\pm 15$ V ( $\pm 5$ %)	$\pm 0.8$	%
$\epsilon_L$	Linearity error		< 0.2	%
$I_O$	Offset current @ $I_p = 0, T_A = 25$ °C		Typ	Max
$I_{OT}$	Temperature variation of $I_O$	0 °C .. + 25 °C	$\pm 0.06$	$\pm 0.15$ mA
		+ 25 °C .. + 70 °C	$\pm 0.10$	$\pm 0.25$ mA
$t_r$	Step response time <sup>1)</sup> to 90 % of $I_{PN}$		40	$\mu$ s


Figure 7-8 LEM LV 25-P voltage transducer technical data

### B.1.5 Baumer GI342 incremental encoder technical data

Technical data - electrical ratings	
Voltage supply	5 VDC $\pm 10$ % 4.75...30 VDC
Reverse polarity protection	Yes (4.75...30 VDC)
Consumption w/o load	$\leq 30$ mA (24 VDC) $\leq 60$ mA (5 VDC)
Resolution (steps/turn)	5...2048
Reference signal	Zero pulse, width 90°
Sensing method	Optical
Output frequency	$\leq 150$ kHz
Output signals	A 90° B, N + inverted
Output circuit	Linedriver RS422 TTL Push-pull short-circuit proof
Interference immunity	DIN EN 61000-6-2
Emitted interference	DIN EN 61000-6-4
Approval	UL approval / E63076

Figure 7-9 Baumer GI342 incremental encoder technical data

## B.1.6 NI CompactDAQ 9178 8-Slot USB Chassis

General	
Number of Slots	8
Operating System / Target	Windows
LabVIEW RT Support 	Yes
Built-In Trigger	Yes
Power Requirements	
Total Available Power	15 W
Input Voltage Range	9 V - 30 V
Counters / Timers	
Counters	4
Size	32 bits
Shock and Vibration	
Operational Shock	30 g
Random Vibration	5 Hz - 500 Hz
Random Operating Frequency Range	0.3 g
Physical Specifications	
Length	25.4 cm
Width	8.81 cm
Height	5.89 cm
Weight	878 gram
Operating Temperature	-20 °C - 55 °C
Maximum Altitude	5000 m

**Figure 7-10 NI CompactDAQ 9178 8-Slot USB Chassis**

## B.1.7 NI 9215 measurement card

General	
Product Family	Industrial I / O
Measurement Type	Voltage
Form Factor	CompactDAQ CompactRIO
Operating System / Target	Windows
RoHS Compliant	Yes
Isolation Type	Ch-Earth Ground Isolation
Analog Input	
Single-Ended Channels	0
Differential Channels	4
Analog Input Resolution	16 bits
Maximum Voltage Range	
Range	-10 V - 10 V
Accuracy	0.003456 V
Simultaneous Sampling ⓘ	Yes
Analog Output	
Number of Channels	0
Digital I / O	
Bidirectional Channels	0
Input-Only Channels	0
Output-Only Channels	0
Counters / Timers	
Counters	0
Physical Specifications	
Length	9 cm
Width	2.3 cm
I / O Connector	BNC connectors Screw terminals
Operating Temperature	-40 °C - 70 °C

Figure 7-11 NI 9215 measurement card



## B.1.8 NI 9401 measurement card

General	
Product Family	Digital I / O Industrial I / O
Measurement Type	Digital Specialty Digital
Form Factor	CompactDAQ CompactRIO
RoHS Compliant	Yes
Isolation Type	Ch-Earth Ground Isolation
Analog Input	
Single-Ended Channels	0
Differential Channels	0
Analog Output	
Number of Channels	0
Digital I / O	
Bidirectional Channels	8
Input-Only Channels	0
Output-Only Channels	0
Timing	Hardware
Maximum Clock Rate	10 MHz
Logic Levels	TTL
Digital Input	
Maximum Voltage Range	0 V - 5.25 V
Digital Output	
Maximum Voltage Range	0 V - 5.25 V
Counters / Timers	
Counters	0
Physical Specifications	
Length	9 cm
Width	2.3 cm
I / O Connector	25-pin D-Sub
Operating Temperature	-40 °C - 70 °C

Figure 7-12 NI 9401 measurement card

## B.1.9 NI 9237 measurement card


General	
Product Family	Industrial I / O
Measurement Type	Strain / Bridge-based sensor
Form Factor	CompactDAQ CompactRIO
Operating System / Target	Windows
RoHS Compliant	Yes
Isolation Type	Ch-Earth Ground Isolation
Analog Input	
Single-Ended Channels	0
Differential Channels	4
Analog Input Resolution	24 bits
Maximum Voltage Range	
Range	-25 mV / V - 25 mV / V
Accuracy	0.0375 mV / V
Bridge Configurations	Full Bridge Half Bridge Quarter Bridge
Simultaneous Sampling 	Yes
Excitation Voltage	2 V 2.5 V 3.3 V 5 V 10 V
Signal Conditioning	Anti-aliasing filter Bridge completion Voltage excitation
Analog Output	
Number of Channels	0
Digital I / O	
Bidirectional Channels	0
Input-Only Channels	0
Output-Only Channels	0
Counters / Timers	
Counters	0
Physical Specifications	
Length	9 cm
Width	2.3 cm
I / O Connector	RJ50
Operating Temperature	-40 °C - 70 °C

Figure 7-13 NI 9237 measurement card